AEROSERVOELASTIC MODELING OF A MISSILE CONTROL FIN


A THESIS SUBMITTED TO
THE GRADUATE SCHOOL OF NATURAL AND APPLIED SCIENCES
OF
MIDDLE EAST TECHNICAL UNIVERSITY


BY


MEHMET OZAN NALCI


IN PARTIAL FULLFILLMENT OF THE REQUIREMENTS
FOR
THE DEGREE OF MASTER OF SCIENCE
IN
AEROSPACE ENGINEERING


FEBRUARY 2013

Approval of the thesis:

**AEROSERVOELASTIC MODELING OF A MISSILE CONTROL FIN**

submitted by **MEHMET OZAN NALCI** in partial fulfillment of the requirements for the degree of **Master of Science in Aeronautical and Aerospace Engineering Department, Middle East Technical University** by,

Prof. Dr. Canan Özgen
Dean, Graduate School of **Natural and Applied Sciences**          _____

Prof. Dr. Ozan Tekinalp
Head of Department, **Aerospace Engineering**          _____

Prof. Dr. Altan Kayran
Supervisor, **Aerospace Engineering Dept., METU**          _____

**Examining Committee Members**

Assoc. Prof. Dr. Funda Kurtuluş
Aerospace Engineering Dept., METU          _____

Prof. Dr. Altan Kayran
Aerospace Engineering Dept., METU          _____

Assoc. Prof. Dr. Melin Şahin
Aerospace Engineering Dept., METU          _____

Asst. Prof. Dr. Ali Türker Kutay
Aerospace Engineering Dept., METU          _____

Msc. Bülent Acar
Roketsan Missiles Industries Inc.          _____

**Date**:          28.02.2013

**I hereby declare that all information in this document has been obtained and presented in accordance with academic rules and ethical conduct. I also declare that, as required by these rules and conduct, I have fully cited and referenced all material and results that are not original to this work.**

Name, Last name     : Mehmet Ozan NALCI

Signature           :

# ABSTRACT

## AEROSERVOELASTIC MODELING OF A MISSILE CONTROL FIN

Nalcı, Mehmet Ozan
M. Sc., Department of Aerospace Engineering
Supervisor: Prof. Dr. Altan Kayran

February 2013, 100 pages

In this thesis, aeroservoelastic modeling of a typical Missile Control Fin was performed. MSC®PATRAN, MSC®NASTRAN, MSC®FlightLoads and Dynamics, MATLAB® and MATLAB®Simulink were used for technical computing, modeling and simulation throughout the study. Linear models of the control fin structure, aerodynamics and servo-actuator system were developed, so as to be able to analyze the aeroservoelastic system in frequency and time domains. The flutter characteristics of the missile control fin for different flight conditions were obtained and presented. Time history of the control fin elastic deflection under unsteady aerodynamic loads, for various actuator commands is simulated. An aeroservoelastic model development strategy is presented, such that the interaction between servo-actuator system dynamics and aeroelastic properties of the control fin could be revealed.

Keywords: Aeroelasticity, Aeroservoelasticity, Flutter, Servoactuation Systems.

# ÖZ

## BİR FÜZE KONTROL YÜZEYİNİN AEROELASTİK MODELLEMESİ

Nalcı, Mehmet Ozan
Yüksek Lisans, Havacılık ve Uzay Mühendisliği Bölümü
Tez Yöneticisi : Prof. Dr. Altan Kayran

Şubat 2013, 100 sayfa

Bu tezde, tipik bir füze kontrol yüzeyinin aeroservoelastik modellemesi yapılmıştır. Teknik hesaplama, modelleme ve simülasyon araçları olarak; MSC$^{®}$ PATRAN, MSC$^{®}$ NASTRAN, MSC$^{®}$ FlightLoads and Dynamics, MATLAB$^{®}$ and MATLAB$^{®}$ Simulink yazılımları kullanılmıştır. Aeroservoelastik sistemin frekans ve zaman uzaylarında incelemelerini yapabilmek amacıyla; füze kontrol yüzeyi yapısının, aerodinamiğinin ve servo-eyleyici sisteminin doğrusal modelleri oluşturulmuştur. Füze kontrol yüzeyi çırpıntı karakteristikleri, çeşitli uçuş koşulları için elde edilmiş ve sunulmuştur. Füze kontrol yüzeyinin çeşitli eyleyici komutları için, durağan olmayan aerodinamik yükler altında verdiği sehim cevabı, zaman uzayında simüle edilmiştir. Servo-eyleyici sistem dinamiği ile füze kontrol yüzeyinin aeroleastik karakteristiklerinin etkileşiminin incelenmesine olanak sağlayan bir aeroservoelastik modelleme stratejisi sunulmuştur.

Anahtar kelimeler: Aeroelastisite, Aeroservoelastisite, Çırpıntı, Servo-eyleyici Sistemler.

*To my family*

# ACKNOWLEDGEMENTS

# TABLE OF CONTENTS

# LIST OF FIGURES

# LIST OF TABLES

TABLES

## NOMENCLATURE

**SYMBOLS**

| | |
|---|---|
| $\mathbf{M}$ | Structural Mass Matrix |
| $\mathrm{C}$ | Structural Damping Matrix |
| $\mathbf{K}$ | Structural Stiffness Matrix |
| $\bar{\mathbf{M}}$ | Aeroelastic Mass Matrix |
| $\bar{\mathrm{C}}$ | Aeroelastic Damping Matrix |
| $\bar{\mathbf{K}}$ | Aeroelastic Stiffness Matrix |
| $\mathbf{F}$ | Generalized Force Vector |
| $\mathrm{I}$ | Identity Matrix |
| $\mathrm{Q}$ | Generalized Aerodynamic Force Matrix |
| $\mathrm{G}$ | Spline Matrix |
| $\bar{\mathrm{Q}}$ | Estimated Generalized Aerodynamic Force Matrix |
| $\mathrm{A}$ | RFA Coefficient Matrix |
| $\mathrm{A}_{sys}$ | System Matrix of the Aeroelastic Fin System |
| $\mathrm{B}_{sys}$ | Input Matrix of the Aeroelastic Fin System |
| $\phi$ | Modeshape Matrix |
| $x$ | Global Displacement Coordinates |
| $t$ | Time |
| $\zeta$ | Generalized Displacement Coordinate |
| $\omega$ | Structural Natural Frequency |
| $s$ | Laplace Variable |
| $k$ | Reduced Frequency |
| $b$ | Semi-chord length |
| $U$ | Free Stream Speed |
| $q$ | Dynamic Pressure |
| $\beta$ | Aerodynamic Lag Root |
| $N$ | Number of Aerodynamic Lag Roots |
| $J$ | Moment of Inertia |
| $T$ | Torque |
| $\theta$ | Angular Position |
| $N_{tr}$ | Transmission Ratio |
| $\eta_{tr}$ | Transmission Efficiency |
| $V$ | Terminal Voltage |
| $K_t$ | Torque Constant |

| | |
|---|---|
| $K_b$ | Back EMF Constant |
| $R$ | Terminal Resistance |
| $L$ | Inductance |
| $c$ | Viscous Damping Coefficient of DC Motor |
| $K_P$ | Proportional Gain of the PD Controller |
| $K_D$ | Derivative Gain of the PD Controller |
| $x_l$ | Aerodynamic Lag States |
| $u$ | Aeroelastic System Input Vector |
| $z$ | Aeroelastic System State Vector |
| $a$ | Speed of Sound |
| $f$ | Frequency of Oscillation for Generalized Aerodynamic Force Matrix Generation |
| $\rho$ | Air Density |
| $h$ | Altitude |
| $g$ | Damping Ratio of Aeroelastic Mode |
| $n_m$ | Number of Degrees of Freedom of Modal Set |
| $n_k$ | Number of Reduced Frequencies |
| $n_s$ | Number of Degrees of Freedom of Elastic Modal Set |

## SUPERSCRIPTS

| | |
|---|---|
| . | $d/dt$ |
| .. | $d^2/dt^2$ |
| ' | Complex Conjugate |
| $T$ | Transpose of Matrix |
| $ij$ | Element of Matrix at i'th Row and j'th Column |

## SUBSCRIPTS

| | |
|---|---|
| $g$ | Global Degree of Freedom Set |
| $a$ | Analysis Degree of Freedom Set |
| $m$ | Modal Degree of Freedom set |
| $c$ | Rigid Modal Degree of Freedom Set |
| $s$ | Elastic Modal Degree of Freedom Set |

**CHAPTER 1**

**INTRODUCTION**

## 1.1 Theoretical Background

### 1.1.1 Aeroelasticity

Aeroelasticity studies the interaction between aerodynamic forces, elastic forces and inertial forces that act on a structure. The famous Collar triangle shown in Figure 1, depicts the interdisciplinary relations that aeroelasticity inherits. Analysis of the Collar's triangle's primary disciplines in double combinations forms the most frequently encountered modeling schemes in literature.



A:      Aerodynamic forces
E:      Elastic forces
I:      Inertia forces

Related Fields
V:      Mechanical vibrations
DS:     Dynamic stability

Static Aeroelastic Phenomena
SSA:    Aeroelastic effects on static stability
L:      Load distribution
C:      Control effectiveness
D:      Divergence
R:      Control system reversal

Dynamic Aeroelastic Phenomena
F:      Flutter
B:      Buffeting
Z:      Dynamic response
DSA:    Aeroelastic effects on dynamic stability

*Figure 1 Collar's Triangle [1]*

Structural dynamic nature of a structure, in the absence of aerodynamic and any other external forces, can be described by accounting for the inertial and elastic forces that act on it. This type of modeling is used for characterizing the nature of the dynamic properties of the structure and is referred as the free vibration problem in literature. Information such as structural natural frequencies, structural damping and flexible mode shapes can be extracted by a free vibration analysis and modal testing of a structure. If external forces that do not couple with the motion are involved, it is possible to study the forced vibration response, a problem in which the response is still a function of the structural dynamic properties, together with the frequency content of the forcing.

The traditional way of modeling the flight mechanics of an aircraft is followed by making the assumption that the structure is rigid throughout the motion. As a result of this assumption, dynamics of the aircraft is modeled only by accounting for aerodynamic and inertial forces. This type of modeling is most frequently used for control system design and flight performance evaluation purposes. The validity of rigid body modeling is questionable when the structure undergoes significant elastic motion, which in turn, alters the aerodynamic forcing on the aircraft. Up to this point, no relation between elastic forces and aerodynamics is established.

There are two main areas that aeroelasticity is divided into. These are namely, static aeroelasticity and dynamic aeroelasticity.

Static aeroelastic formulation neglects the dependence of the states of the structure to time. As a result of this assumption, any time dependent phenomena that act on the motion of the structure vanish. This implies that, in turn, all of the inertial and damping forces that are present in the aeroelastic system, whether it originates from the structure or the aerodynamics, is neglected. This formulation does not allow an exchange between kinetic and internal elastic potential energy of the structure. Therefore only the internal elastic forces and the steady aerodynamic forces that act on the structure is taken into account. In other words, the position of the structure is momentarily frozen in time regardless of its motion and flow history and studied for its strength and aerodynamic form. Static aeroelastic formulation gives the opportunity to analyze an aircraft for load distribution, control effectiveness, aeroelastic divergence, and static flight stability. For example, static trim condition at an airspeed/air density combination is analyzed with static aeroelasticity formulation, so as to reveal the effects of aeroelasticity on control surface deflections and static flight stability margins.

Dynamic aeroelasticity takes into account all of the primary force components in Collar's triangle. As time dependent phenomena is now presented, inertial and damping forces due to the structure is modeled. As a result, aerodynamics is dependent not only on the momentary position of the aircraft, but also on the velocity and acceleration of the aircraft. Time dependence of aerodynamics also brings the transient aerodynamic phenomena involved in the flow field into the picture. Dynamic aeroelastic formulation gives the opportunity to analyze dynamic time response, flutter margins, limit cycle oscillations, buffeting phenomena and aeroelasticity effects on dynamic flight stability.

Table 1 lists the topics that are addressed by static and dynamic aeroelastic formulations, after which brief explanations of these topics follow [1].

*Table 1 List of Aeroelastic Problems*

| Static Aeroelastic Phenomena | Dynamic Aeroelastic Phenomena |
|---|---|
| Load Distribution | Dynamic time response |
| Aeroelastic Divergence | Flutter |
| Control Effectiveness | Limit Cycle Oscillations |
| Control Reversal | Buffeting |
| Static Flight Stability | Dynamic Flight Stability |

- **Load distribution:** "Influence of elastic deformations of the structure on the distribution of aerodynamic pressures over the structure."
- **Aeroelastic Divergence:** "A static instability of a lifting surface of an aircraft in flight, at a speed called the divergence speed, where the elasticity of the lifting surface plays an essential role in the instability."
- **Control Effectiveness:** "Influence of elastic deformations of the structure on the controllability of an airplane."

- **Control Reversal:** "A condition occurring in flight, at a speed called the control reversal speed, at which the intended effects of displacing a given component of the control system are completely nullified by elastic deformations of the structure." Control reversal makes the aircraft completely uncontrollable.
- **Static Flight Stability:** "Influence of elastic deformations of the structure on static airplane stability." Static flight stability is important for all aircraft, whether it is actively controlled or not, since a change in the margins of stability due to aeroelastic effects may cause the loss of the aircraft.
- **Dynamic time response:** "Transient response of aircraft structural components produced by rapidly applied loads due to gusts, landing, gun reactions, abrupt control motions, moving shock waves, or other dynamic loads."
- **Flutter:** "A dynamic instability occurring in an aircraft in flight, at a speed called the flutter speed, where the elasticity of the structure plays an essential part in the stability." Flutter is a catastrophic instability, in which oscillations of a structure due to aeroelastic effects grow unboundedly until structural failure.
- **Limit Cycle Oscillations:** Limited amplitude, oscillatory response of a structure, usually due to the resultant effect of an aeroelastic or aeroservoelastic instability and nonlinearity inherent in the structure. The limit cycle can be a single or multiple frequency oscillation below or over instability airspeed.
- **Buffeting:** "Transient vibrations of aircraft structural components due to aerodynamic impulses produced by the wake behind wings, nacelles, fuselage pods, or other components of the airplane."
- **Dynamic Flight Stability:** "Influence of elastic deformations of the structure on dynamic airplane stability."

### 1.1.2    Aeroservoelasticity

Aeroservoelasticity studies the interaction between aerodynamic, inertial, elastic and control forces that act on an aircraft. The interaction between control dynamics and aeroelastic properties of an aircraft naturally inherits transient dynamics, therefore aeroservoelasticity is a topic of dynamic aerelasticity. Steady and unsteady effects on the structure are studied, since both interact with control system dynamics. The structure being analyzed may be a single control surface or a full aircraft with control surfaces. Studies on aeroservoelasticity mainly focuses on modeling, analysis and control of aeroelastic responses. Since this thesis focuses on modeling linear aeroservoelasticity, a brief survey on aeroservoelastic modeling is presented.

#### 1.1.2.1    Survey on Aeroservoelasticity

Theodore Theodorsen, the most famous pioneer in the field of aeroelasticity, established a set of equations which involve the famous Theodorsen function and the paved the ways to flutter analysis and control[2]. Theodorsen function was a complex frequency response function together with the set of equations, which took vertical translational, torsional degree of freedoms of a 2D wing section and the rotation angle of its aileron. The outputs were the unsteady lift force, the pitching moment and the aileron hinge moment.

Parallel to the work of Theodorsen, Wagner defined his own function in time domain, which exploits the formation of circulatory lift due to a step change in angle of attack[3]. He used the model to demonstrate how the lift acting at the quarter chord of the aerofoil forms.

Kussner, on the other hand, demonstrated the lift formation of the airfoil subject to a sharp edged gust[4]. Similar to Wagner, Kussner showed how the lift changes as an arifoil enters a gust, as a function of time. Garrick's work[5] revealed the Fourier Transform relationship of Theodorsen's function with Wagner's function and with Kussner's function.

Later, von Karman and Sears[6] dealt with the unsteady aerodynamics of an airfoil in non-uniform motion. They formulation was applicable to general non-uniform motion, leaving Theodorsen's, Wagner's and Kussner's solutions as specific cases of flow.

In 1946, Collar explained the interaction between aerodynamic, elastic and inertial forces that act on a structure[7]. He formed the famous Collar's Triangle diagram, which is shown in Figure 1.

Ashley ,in 1962, formulated complete aeroelastic equations of flexible flight vehicle for the first time, which permitted large rigid-body motion in addition to small and linear elastic displacements[8]. Garrick, in his work on development of supersonic research vehicle X-15, added another dimension to the Collar's diagram, which was aerodynamic heating[9].

Garrick, in 1976, gave a detailed description of research on active control of aeroelastic response[10]. He described load alleviation, modal suppression, flutter control based on aerodynamic energy methods, flutter control of aircraft with external stores, and the mathematical treatment of active control research. Analytical and numerical methods used to model the unsteady aerodynamics of arbitrary aerodynamic configurations was explained. He also commented on future work of state-space and optimal control theory applications in aeroservoelastic modeling.

Albano and Rodden developed the subsonic Doublet Lattice Method and implemented the method to the aeroelastic analysis module in NASTRAN[11]. The Doublet Lattice Method and its later improvements[13] was capable of modeling linear unsteady aerodynamics of deformable thin bodies by panel disceratization, also for subsonic compressible flow.

Vepa, in 1977, used Pade approximants to build rational models of aerodynamics for arbitrary motion, from knowledge of oscillatory aerodynamic forces on thin airfoils[13]. He explained the behavior of unsteady airloads in the frequency domain and extended the oscillatory aerodynamic forces into the entire frequency domain.

In 1979, Edwards studied active control of elastic vehicles[14]. In his work, the transfer functions relating the arbitrary airfoil motion to the airloads were derived from the Laplace transforms of the linearized airload expressions for incompressible, two dimensional, potential flow. He inverted the Laplace transforms to obtain exact expressions for transient airloads and motions.

Roger proposed a method to represent unsteady aerodynamic forces in the Laplace domain, by utilizing rational function approximation[15]. He used a second-order polynomial of the Laplace variable 's' plus the summation of a user-defined number of first-order filters which accounted for the wake effects in unsteady flow. Roger's procedure was improved by Tiffany and Adams[16] and by Karpel[17] for better curve fitting of oscillatory aerodynamic forces. Karpel's work was also minimizing the number of lag filters that has to be added to obtain good fits. Formulating the 3D panel aerodynamics of wing-control surface combinations in state space was made possible through the use of Doublet Lattice Method for the whole subsonic region, at least for linearized potential flow, and using rational function approximations.

Once the state-space equations of aeroservoelastic systems were available, it was possible to apply modern control theory to design optimal or robust controllers for flutter-suppression. Nissim and Abel[18] proposal of a method on aerdynamic energy and Newsom's[19] optimal control methods were used to design robust feedback control laws for flutter suppression.

Practical and linear formulations of the structure with finite element modeling and the aerodynamics with the Doublet Lattice Method, together with the Rational Function Approximation methods, paved the way to aeroelastic and aeroservoelastic optimization studies. Karpel used methods of optimization for linear problems and problems involving concentrated structural nonlinearities[20][21]. Karpel used the fictitious mass method[22] to model concentrated nonlinearities in structures. He also published several papers on aeroelastic and aeroservoelastic modeling incorporating control action as a rigid body mode in aeroservoelastic modal equations[23][24][25].

## 1.2    Objective of the thesis

The motivation behind the study in this thesis is to present a generic aeroservoelastic mathematical model of an all-movable aerodynamic control surface.

The study is focused on a missile control fin, which is a part of the control actuation system of a subsonic missile. Control actuation systems of missiles are of various types. Electro-hydraulic, pneumatic and electro-mechanical control actuation systems exist, where each type has its advantages and disadvantages. Electromechanical actuation systems are widely preferred because of their conservative power consumption, linearity, denser packaging, and good performance at disturbance load rejection. The control actuation system modeled in this thesis is of electro-mechanical type.

The requirements of a missile control fin are specified from a top to down perspective, taking start from various top system level requirements. From the operational requirements of a missile, the missile system designer determines how agile the missile should be and how much maneuvering capability it should have, for a range of flight conditions formed by speed and altitude profiles. The answer to these questions, together with robustness considerations, specifies the overall aerodynamic design, the controller design and the flight stability margins of the missile. The control fins included in a control actuation system are usually designed to provide the predefined static flight stability margins and controllability of the missile. The consideration given to aeroelastic phenomena in early design stages is crucial in obtaining the desired static and dynamic stability and performance of the missile.

In this thesis, the missile control fin structure is assumed to be already designed, neglecting the aeroelastic effects on both the missile and the fin. Therefore the structural properties of the fin are fixed. The servo-actuation system selection and controller design studies are carried out accordingly. The performance requirements and constraints of the missile control fin are specified in Table 2. All requirements given in Table 2 are assumed to be given before the servo-actuation system selection and the controller design, except the maximum load torque. The derivation of the maximum load torque is related with the aerodynamics and the dynamic performance of the fin, and it is presented in Section 4.1.1.

*Table 2 Requirements and Constraints of the Missile Control Fin*

| | |
|---|---|
| Angular Position Limit | 15° |
| Maximum Input Voltage | 24 V |
| Maximum Input Current | 10 A |
| Settling Time up to 15° Angular Position Command | 50 ms |
| Steady State Angular Position Error | 2% |
| Maximum Load Torque | 6 N.m |
| Minimum Angular Speed at Maximum Load Torque | 300°/s |
| Maximum Diameter of Actuator | 28 mm |
| Processor Frequency | 1 kHz |

The flight conditions that the fin is subjected to are given in Table 3.

*Table 3 Flight Conditions of the Missile Control Fin*

|  | Minimum | Maximum |
|---|---|---|
| Range of Altitudes | 0 m | 5000 m |
| Range of Mach Numbers | 0.4 | 0.6 |

## 1.3 Scope of the Thesis

Aeroservoelastic modeling steps are divided into five chapters. The methodology of modeling followed is demonstrated in Figure 2.
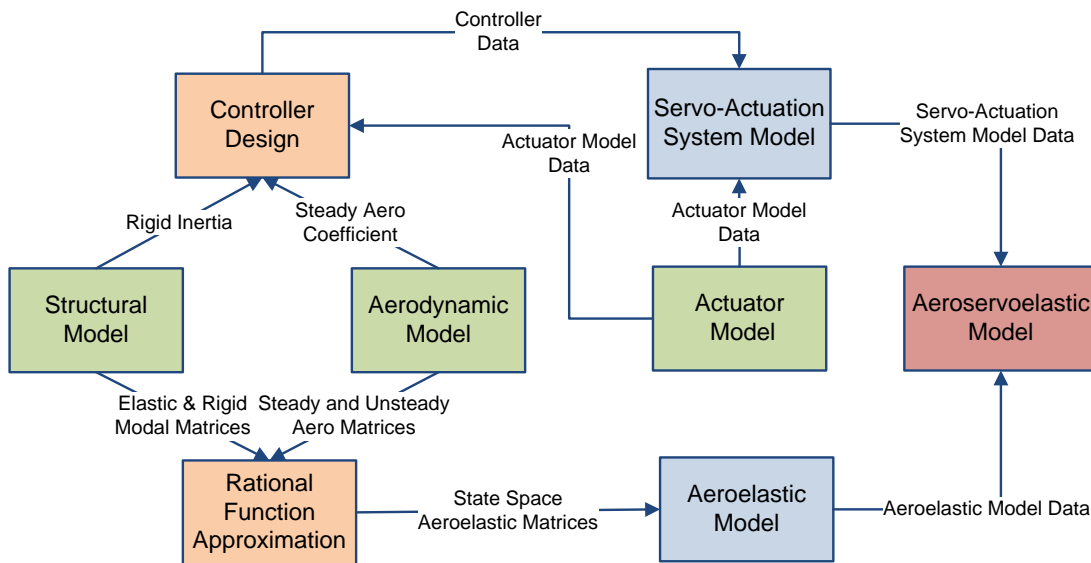


*Figure 2 Methodology of Aeroservoelastic Modeling*

In Chapter 2, the engineering approach to aeroservoelastic modeling of the missile control fin is discussed. The equations and tools used for the structural, the aerodynamic and the servo-actuation system modeling are explained. Physical reasoning behind the decisions, together with the assumptions that lead to the given models is given. Structural and aerodynamic model integration is also formulated. This chapter provides the physical and mathematical basis for the following modeling chapters.

In Chapter 3, the modeling steps followed in MSC PATRAN and MSC Flightloads and Dynamics are described. Since the models are exported from MSC Nastran solver and implemented in MATLAB, a validation procedure is carried out to make sure the implemented models are identical to the ones modeled by MSC PATRAN and MSC Flightloads and Dynamics. Additional modeling steps to obtain time domain aerodynamic forces are followed in MATLAB. The validation procedure includes the normal modes analysis and the flutter analysis of the missile control fin. A generic flutter analysis procedure is described and the flutter speed is obtained by both frequency domain and time domain analysis.

In Chapter 4, the MATLAB Simulink model of the servo-actuation system is presented. The parameters of a permanent magnet DC-Motor and a Transmission Unit is selected for smooth operation of the missile control fin under given requirements in Table 2. A PD controller is designed using the Root Locus Method, in compliance with the requirements, assuming that the missile control fin is rigid, and the aerodynamics is steady. The performance of the servo-actuation system under these assumptions is demonstrated.

In Chapter 5, the integration of the models implemented in MATLAB and MATLAB Simulink in Chapter 3 and Chapter 4 is explained, and the resulting performance of the aeroservoelastic system is presented. The behavior of the aeroservoelastic system in both frequency domain and time domain is investigated. The effect of the assumptions made in Chapter 4, such as the fin being rigid and the aerodynamics being steady is discussed.

In Chapter 6, the final comments on thesis are made. Also, the alternatives for future work are discussed.

# CHAPTER 2

# AEROSERVOELASTIC MODELING APPROACH

The physical phenomena involved in aeroservoelastic modeling of a missile control fin are multidisciplinary. The three disciplines involved; aerodynamics, structural dynamics and servo-actuator dynamics may exhibit linear/nonlinear and steady/unsteady behavior. It is often not only practical but also obligatory to make simplifying assumptions for the aeroservoelastic problem at hand, in order to reach a solution. Therefore a clear understanding of the underlying physical phenomena is crucial to be able to make assumptions that simplify the problem, while keeping key aspects of the physics involved. This chapter builds the aeroservoelastic model of a missile control fin, together with introducing the most frequently encountered assumptions and simplifications, so that the analysis objectives presented at Section 1.2 are met with an acceptable accuracy.

## 2.1    Structural Modeling Approach

Modeling of aircraft structures such as wings and control surfaces is performed by analytical or finite element methods. The decision among the two methods is governed by applicability of the methods to the specific problem under consideration. Although the exact analytical formulations give exact solutions, they are limited to very simple cases of structural problems. Closed form solutions of the differential equations that govern the structural dynamics of complex problems are not readily available. On the other hand, finite element formulations are widely used because of their ability to obtain accurate solutions for complex geometries with various boundary conditions.

In this thesis, structural dynamics modeling of the missile control fin is performed by the finite element method. This decision is motivated by the fact that the formulation developed in this thesis is intended to be a generic one with acceptable accuracy. Formulating the structural dynamics of the missile control fin with finite element modeling renders the aeroservoelastic model to be applicable to complex geometries of various shapes and boundary conditions.

The control fin structure modeled is shown in Figure 3.
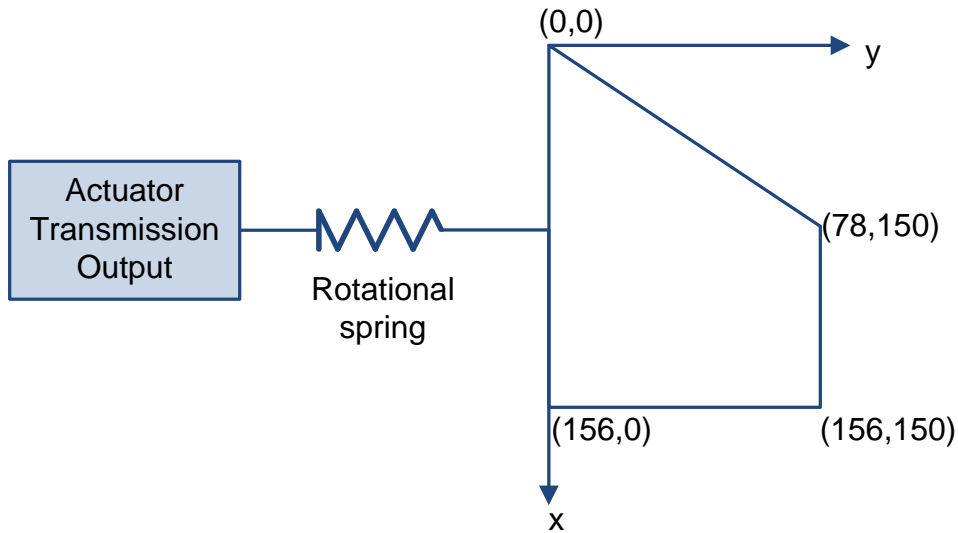
*Figure 3 Missile Control Fin*

The thickness profile of the fin along the span is given in Figure 4.
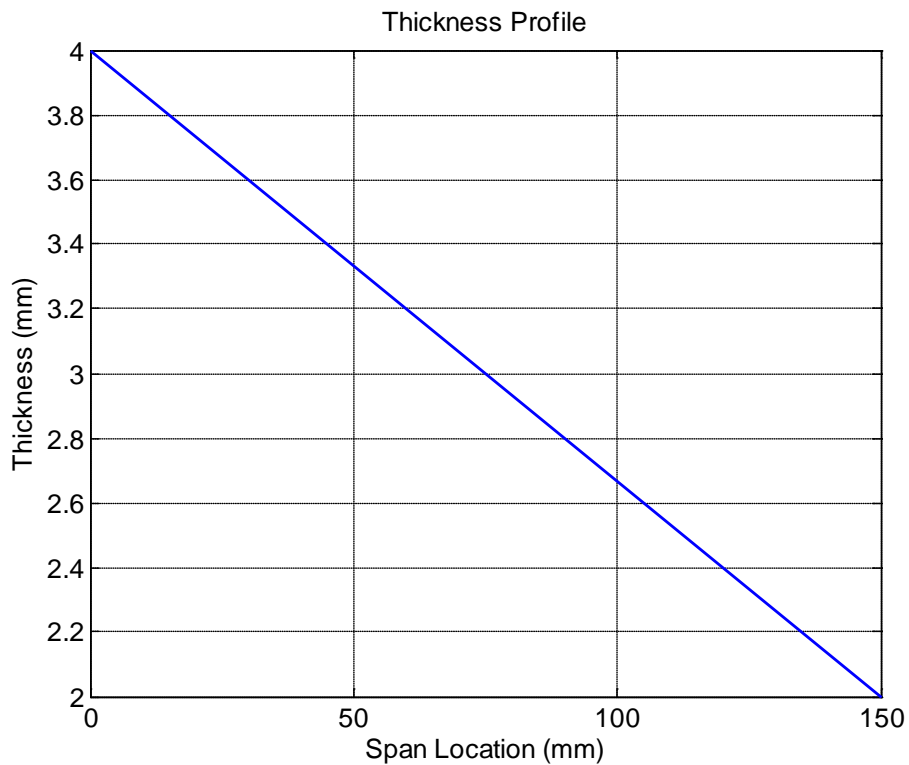


*Figure 4 Missile Control Fin Thickness Profile*

The fin is assumed to have linear structural properties. It is tightly connected to the servo-actuation system by a shaft that has rotational stiffness. The material selected for the fin is isotropic and its structural properties; mass, inertia, damping and stiffness are independent constants of the problem.

Thermal stiffening effect, nonlinearities due to large deflections and any other nonlinear phenomena is neglected. The elastic structural deflections are assumed to be small and linearly independent from rigid body motion. Also, there is no coupling between the elastic modes of the structure, hence they are orthogonal. Therefore it is possible to obtain solutions to the structural dynamics problem by means of modal reduction and superposition methods.

In reality, a structure has an infinite number of structural natural frequencies and modeshapes. Through a normal modes analysis on a finite element model, structural modes equal to the number of degrees of freedom of the model can be obtained. Typically, less than half of these modes are accurate, depending on the complexity of the problem.

Aircraft structures can be of significant spatial size, and it is practical to treat the problem with a number of equations much smaller than the number degrees of freedom of the finite element model. In aircraft structural dynamics analysis, modal reduction is usually employed to reduce the problem size. The physical motivation behind the reduction process is that, a relatively narrow frequency range of interest dominates the dynamics of the structure. Through a proper selection of a number of low frequency structural modes, it is possible to capture the dominant dynamics of a structure and reduce the problem size. For the cases where an independent external forcing is also involved, the frequency content of the external forcing agents should be taken into account. Following steps clarify the finite element modeling and modal reduction process.

Structural dynamics of the missile control fin is formulated by Finite Element Method (FEM) as follows:

$$[\mathbf{M}]\ddot{x} + [\mathbf{C}]\dot{x} + [\mathbf{K}]x = \{\mathbf{F}(x,\dot{x},\ddot{x},t)\} \tag{2.1}$$

The parameters and variables are defined as:

$\mathbf{M}$: global mass matrix                          $x$: global displacement vector

$\mathbf{C}$: global damping matrix                   $\dot{x}$: global velocity vector

$\mathbf{K}$: global stiffness matrix                   $\ddot{x}$: global acceleration vector

$\mathbf{F}$: global forcing matrix                        $t$: time

The term 'global' that qualifies the parameters and variables, points out that they are expressed in the global spatial coordinates that the problem is defined. The size of the matrices involved in Eqn. (2.1) is set by the complexity of the problem and is equal to the number of equations of motion to be solved, before the boundary conditions are applied. Whereas the size of the full finite element model of an aircraft structure can be on the order of millions, size of the modal problem is typically smaller than thirty[26].

First, the free vibration problem must be formulated and solved for the natural frequencies and modeshapes of the control fin. The free vibration problem is the homogenous differential equation formulation of Eqn. (2.1), where also the boundary conditions have been applied :

$$[\mathbf{M}_{aa}]\ddot{x} + [\mathbf{C}_{aa}]\dot{x} + [\mathbf{K}_{aa}]x = 0 \tag{2.2}$$

Displacement history of Eqn. (2.2), when released from an initial condition, can be described by modal superposition as[27] :

$$\mathbf{x}(t) = [\phi_{aa}]\{\zeta_a(t)\} \tag{2.3}$$

$\phi_{aa}$ is the modal matrix that possesses all modeshapes of the finite element model as column vectors and $\zeta_a(t)$ is the generalized coordinate vector in a-set.

A modeshape is defined only on the spatial domain and is independent of any external forcing. It is only a function of structural properties and the boundary conditions of the structure. The generalized

coordinate on the other hand is a function of time, and can be solved by a forced response analysis that accounts also for transient dynamics. It can be said that an element of the generalized coordinate vector specifies the amount of contribution of its corresponding modeshape to the total displacement solution at a given time.

In this thesis, to obtain the structural natural frequencies $\omega_a$ and the corresponding modeshapes $\phi_{aa}$, normal modes analysis is carried out in MSC®NASTRAN and MATLAB®. Mass and stiffness matrices obtained from the finite model of the control fin, which was built in MSC®PATRAN are used in the analysis. The reduced modal matrix is obtained by selecting a number of low frequency modes from $\phi_{aa}$ to form $\phi_{am}$, which is also mass normalized to uncouple the equations of motion. The typical normal modes analysis seeks a solution to the famous eigenvalue problem Eqn. (2.4), which is derived from Eqn. (2.2) [27]:

$$[K_{aa}] = [M_{aa}][I]\omega_a^2 \tag{2.4}$$

$I$ is the identity matrix of a-set size.

MSC®NASTRAN Solver 103 is utilized to obtain $\omega_a$ and $\phi_{aa}$ from Eqn. (2.4). MSC®NASTRAN utilizes the Lanczos eigenvalue problem solver as default [28].

As the modal matrix $\phi_{aa}$ is obtained and reduced to $\phi_{am}$, by substituting Eqn. (2.3) in Eqn. (2.1) and multiplying by $\phi_{am}{}^T$, the final structural dynamics equation is obtained :

$$\left[\phi_{am}{}^T\right][\mathbf{M}_{aa}][\phi_{am}]\{\ddot{\zeta}_m(t)\} + \left[\phi_{am}{}^T\right][C_{aa}][\phi_{am}]\{\dot{\zeta}_m(t)\} + \left[\phi_{am}{}^T\right][\mathbf{K}_{aa}][\phi_{am}]\{\zeta_m(t)\}$$
$$= \left[\phi_{am}{}^T\right]\{\mathbf{F}_a(x,\dot{x},\ddot{x},t)\}$$

$$[\mathbf{M}_{mm}]\{\ddot{\zeta}_m(t)\} + [C_{mm}]\{\dot{\zeta}_m(t)\} + [\mathbf{K}_{mm}]\{\zeta_m(t)\} = \{\mathbf{F}_m(x,\dot{x},\ddot{x},t)\} \tag{2.5}$$

Eqn. (2.5) is the reduced form of the structural dynamics problem. The subscript 'm' is used for the reduced modal set. This modal set also includes a rigid body mode, which accounts for rigid control surface motion due to actuator input. $\mathbf{F}_m(x,\dot{x},\ddot{x},t)$ is the vector of external forces at modal coordinates.

In Laplace domain, Eqn. (2.5) is expressed as :

$$\left(s^2[\mathbf{M}_{mm}] + s[C_{mm}] + [\mathbf{K}_{mm}]\right)\{\zeta_m(s)\} = \{\mathbf{F}_m(s)\} \tag{2.6}$$

Eqn. (2.6) will be used for constructing the aeroservoelastic equation of motion in Section 2.4.

## 2.2    Aerodynamic Modeling Approach

Aerodynamic modeling of aircraft structures necessitates a careful treatment of the underlying physical phenomena. From the very complex Navier-Stokes Equation solutions to the very simple 2D Strip Theory solutions, there exists a variety of options that enables the engineer to model key aspects of physical phenomena. This section focuses on how an aerodynamic model is selected for the missile control fin.

Nature has no difficulty in implementing physical laws. This fact is observed and taken into granted in our everyday life. This is not the case when man tries to model and solve the corresponding phenomenon. Aerodynamics of real flows is very complicated and currently it is impossible to obtain analytical solutions to the equations that govern the physics of all kinds of flow. Although Navier-Stokes equations govern all known physical phenomena for external flows, when the fluid is assumed to be a continuous medium, the equation is almost always solved by methods that require certain assumptions about the nature of the flow. The assumptions and simplifications that suit the nature of the flow and the objectives of the corresponding engineering analysis must be selected cautiously. The simplest aerodynamic model should be selected, which allows the engineer to model key aspects of the problem while insignificant phenomena are neglected.

Real flows are simplified to types of simpler flow, depending on the behavior of the velocity field. To model a flow, the simplification process mainly focuses on compressibility, viscosity, steadiness and the number of significant dimensions of the flow. The simplest model would be incompressible, inviscid, steady and one dimensional; whereas in nature, all flows are compressible, viscous, unsteady and three dimensional to some extent. The operating conditions of the missile control fin are considered in order to make suitable simplifications about the flow. From the discussion below, nature of the flow and aerodynamic model is decided.

*Compressibility:* As the fin is expected to operate at free stream speed comparable to the speed of sound, the flow is compressible. In fact all flow above Mach 0.3 is considered to be compressible [29]. Also as the free stream speed is well below the speed of sound, no shock formation is expected, the flow field is entirely subsonic.

*Viscosity:* Regarding the operating conditions as specified at Table 2, the fin is expected to operate at an incidence angle region below 15°. For slender bodies such as the missile control fin, in this region of small incidence, it is reasonable to assume that no flow separation occurs. Therefore viscosity only plays a role in a thin boundary layer around the fin. Other regions of the flow are inviscid.

The existence of the viscous boundary layer brings important effects: formation of shear stress and establishment of Kutta condition. For the operating conditions specified, net effect of shear stress on magnitude of lift is insignificant, thus neglected. For aeroelastic analysis, unsteady lift is the parameter that we are interested in and it is mainly formed by normal pressure distribution. Therefore, viscous effects on equation of motion of the aerodynamics of the fin are neglected. Although this is equivalent to saying that the flow field is entirely inviscid, one should be aware that viscosity creates the mechanism that forms the lift and this mechanism should be accounted for while constructing the equation of motion. Although the shear stress effect is insignificant by means of lift magnitude, it is the reason how a finite and continuous lift distribution around an airfoil is formed. It has the effect of smoothing large pressure fluctuations at the trailing edge and thereby establishing the Kutta condition, through shaping the time history of normal pressure distribution around an airfoil. Therefore, the effect of viscosity on the flow cannot be entirely neglected. Although the entire flow field is assumed to be inviscid, the effect of viscosity on formation of lift is somewhat included in the aerodynamic modeling, as will be discussed later.

*Time Dependence:* As dynamic aeroelastic effects are sought in this thesis, obtaining the time history of aerodynamic forcing is crucial. Modeling unsteadiness will introduce key unsteady aerodynamic effects such as:
- The phase lag between the motion of the structure and aerodynamic forcing. Including this behavior is the key to be able to detect dynamic aeroelastic effects such as classical flutter.
- Attenuation of the magnitude of aerodynamic forcing when compared to quasisteady aerodynamics. Quasisteady aerodynamics is discussed in Section 2.2.1.1.

***Flow Dimensionality:*** Aspect ratio of the control fin shown in Figure 3 necessitates that it is modeled by three dimensional aerodynamics. Its chord and span lengths are comparable. Anyway, one of the challenges in this thesis is to present a generic aeroservoelastic modeling technique for lifting surfaces, therefore the finite span effects on the flow is accounted for.

### 2.2.1 Unsteady Lift Model

A common and practical model for a compressible, inviscid, unsteady and three dimensional flow for a slender lifting surface is the linearized potential flow model. If the free stream is irrotational and the flow field is inviscid, then the flow will remain irrotational. This enables the velocity field to be expressed by the gradient of a scalar potential. Therefore the flow can be modeled as a potential flow. Because the missile fin is thin and the incidence angle region is below 15°, the equation of motion can be linearized [29].

#### 2.2.1.1 Generation of Unsteady Lift

Unsteadiness in a flow is stimulated by a change of state in the boundary conditions.
Two types of boundary conditions exist for subsonic flow: the free stream boundary condition and the wall boundary condition. The free stream boundary condition states that all disturbances should die out in the free stream, and this condition holds for both steady and unsteady analysis. On the other hand, the wall boundary condition behaves different for steady and unsteady flow. Whereas an airfoil is just an impenetrable rigid surface for a steady state analysis, it becomes a source of perturbation when the motion of the airfoil is considered. Therefore the wall boundary condition becomes a dynamic boundary condition, whose position and velocity states are derived from the motion of the airfoil. This motion of the airfoil can be elastic, rigid or resultant of both.

The measure of unsteadiness of a flow is the reduced frequency :

$$k = \frac{\omega b}{U}$$

(2.7)

In Eqn. (2.7), $\omega$ is the oscillation frequency of the aerodynamic surface, $b$ is the semi chord length and $U$ is the free stream speed. As this number grows in magnitude, the significance of unsteady effects grows in the flow. In order to clarify how unsteadiness acts on an airfoil, consider Figure 5.
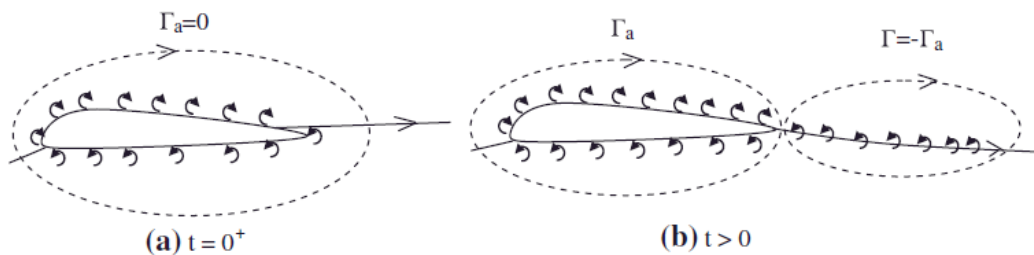


*Figure 5 Generation of Circulatory Lift[30]*

Suppose that the airfoil is suddenly exposed to the free stream conditions. At the beginning of the motion, the circulation around the airfoil is zero, so the lift is zero. As time passes, the vortices formed by the boundary layer are shed into free stream from the trailing edge. As the steady state is reached, the vortices leave the trailing edge smoothly, as stated by the Kutta condition. This is the time history

of the motion up to steady state; and this mechanism holds for changes in angle of attack, changes in free stream speed and changes in boundary conditions.

Now suppose that this airfoil makes harmonic heave motion with a certain amplitude and frequency, and it has no lift at zero incidence. The steady lift value will be zero but the unsteady lift value will not. The unsteady lift value also depends on the amplitude and frequency of motion. This dependence of unsteady lift on frequency has been studied Theodorsen[2] on two dimensional airfoils, called the typical section, such as shown in Figure 6.
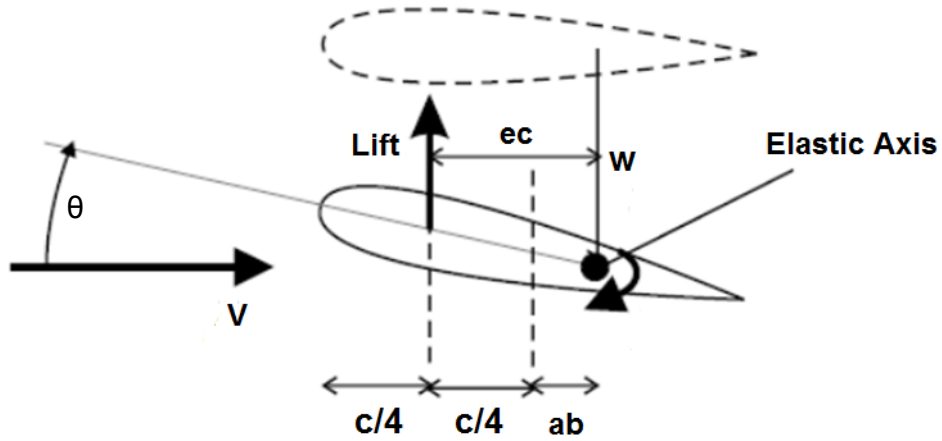


*Figure 6 The Typical Section*

In Figure 6, the parameters are defined as:

V : freestream speed
c : chord length
ec : distance between center of pressure and elastic axis
ab : distance between midchord and elastic axis
θ : Pitching angle
w : Heave displacement

Suppose that this typical section makes a harmonic heave and pitch motion simultaneously with the dynamics given in Eqn (2.8), where $\overline{w}$ and $\overline{\theta}$ are amplitudes of heaving and pitching harmonic motion respectively.

$$w = \overline{w}e^{i\omega t}$$
$$\theta = \overline{\theta}\,e^{i\omega t}$$

(2.8)

Theodorsen's formulation modifies the quasisteady lift amplitude with a function that is frequency dependent, and also adds a phase shift. It assumes incompressible, inviscid but unsteady flow. Theodorsen's formulation of lift is given here to clarify the unsteady lift force agents [31]:

$$Lift = 2\pi\rho UbC(k)\left[U\theta - \dot{w} + b(\frac{1}{2} - a)\dot{\theta}\right] + \pi\rho b^2\left[U\dot{\theta} - \ddot{w} - ba\ddot{\theta}\right]$$

(2.9)

Where,

$\rho$ : Free Stream Density

$C(k)$ : Theodorsen's Function

The first part of the lift in Eqn. (2.9) is due to circulation and is modified by Theodorsen's function. This part is responsible for the lag between structural motion and aerodynamic motion. It is also the key part of the equation that enables the analyst to detect the most famous dynamic instability, flutter. Second part of the equation is related to non-circulatory lift. It is the so called apparent mass effect [29] and is significant at much higher reduced frequencies [30]. When $C(k)$ is taken to be unity and the non-circulatory part is neglected, the remaining lift is called the quasisteady lift. The quasisteady lift accounts for the momentary position and velocity of the airfoil, but does not account for the time history of aerodynamic forcing. In Figure 7, the comparison between quasisteady and unsteady lift for sinusoidal change in angle of attack, according to Theodorsen's function, is given.
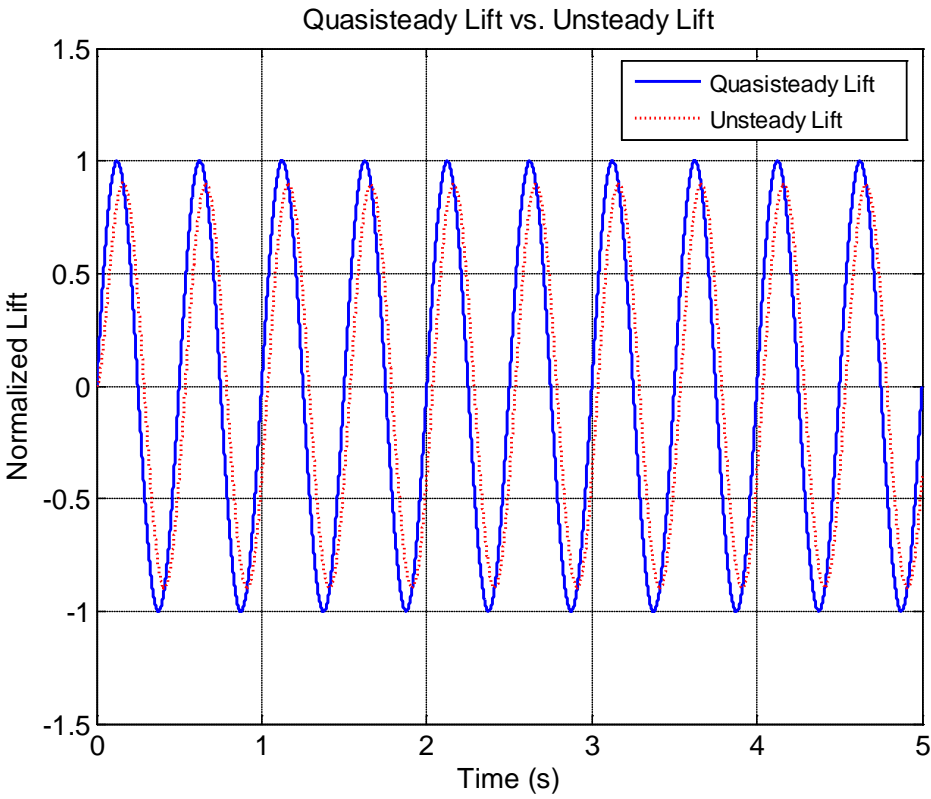


*Figure 7 Comparison of Quasisteady and Unsteady Lift for Sinusoidal Incidence Change*

This discrimination of types of forces that act on the airfoil is crucial in understanding the unsteady behavior of aerodynamic forcing. Although a more complex computational method is used in this thesis, the physical phenomena involved is not different than what is discussed above.

### 2.2.1.2 The Doublet Lattice Method

When 2D Strip Theory or relevant modeling techniques are not preferred, the modeling techniques that the aeroelastician is left with are the CFD methods. A very widely used computational modeling tool for thin airfoils in 3D is panel discretization. It is a fast and medium-to-high fidelity tool that is used for modeling linear aerodynamics. These tools can account for finite span effects on aeroelastic surfaces. Panel discretization tools of varying fidelity exists, some of which can account also for thickness effects and frequently observed types of aerodynamic nonlinearity such as shock formation or vortical effects[32][33].

MSC®FlightLoads and Dynamics module [35] includes a subsonic aerodynamic solver, which solves the linearized potential flow equation for arbitrary geometries by panel discretization. This tool is

widely accepted and utilized in aeroelastic analysis and design of aircraft in the industry. The Doublet Lattice Method (DLM), which is an acceleration potential method developed by Albano and Rodden [11] is implemented in the solver to model unsteady lift generation on the panels due to harmonic structural motion. DLM can also be used for modeling steady aerodynamics when the reduced frequency is very close to zero. It is actually equivalent to the Vortex Lattice Method[36] when the reduced frequency is zero.

Like Theodorsen's aerodynamic formulation, DLM generates aerodynamic forcing that depends on harmonic motion of an aerodynamic surface. In this case, the aerodynamic surface is discretized into trapezoidal panels. DLM is similar to the Kernel Function Method [30]. It introduces constant strength doublet lines into quarter chord of each panel and solves the linearized potential equation for harmonic pressure perturbations of each panel. The unknown lifting pressures are assumed to be concentrated uniformly across the one-quarter chord line of each panel [34]. The transverse structural displacement $w$ at a three quarter chord of a panel is taken as the downwash value of the panel. This point is called as the control point. The chord lines must all lie parallel to the flow.
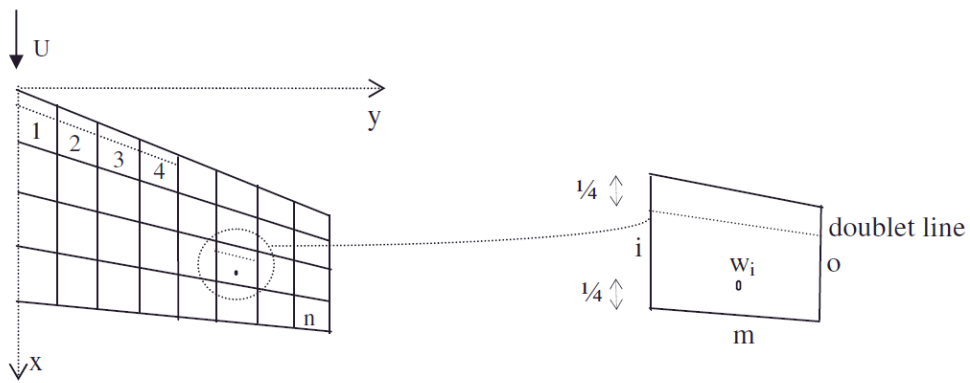


*Figure 8 Panel Discretization of DLM [34]*

DLM creates the so called Generalized Aerodynamic Forcing (GAF) Matrices at specified Mach numbers and reduced frequencies for simple harmonic motion of the structure. Therefore the GAF matrices obtained from DLM cannot be directly used to model transient aerodynamic phenomena. It is only directly applicable to steady state sinusoidal motion. In order to model transient and dynamic aerodynamic phenomena together with the steady state aeroelastic condition, these frequency dependent GAF matrices must be represented as a continuous function of reduced frequency. For a specified Mach number and several reduced frequencies it is possible to obtain a continuous frequency response by Rational Function Approximation (RFA) methods. The RFA method used in this thesis is presented at Section 2.2.1.4.

### 2.2.1.3    Generalized Aerodynamic Forcing Matrices

The GAF matrices relate aerodynamic forcing to structural displacements. They are formulated in matrix format so that they comply with the finite element formulation of structural dynamics. A GAF matrix, which is a function of a Mach number and a reduced frequency, can be expressed in different sets of analysis in MSC®FlightLoads and Dynamics. The k-set is the aerodynamic set [35]. The nomenclature for a GAF matrix is as follows:

$Q^{ij}_{kk}(M,k)$ :   Aerodynamic Force Coefficient on i'th aerodynamic grid point due to unit downwash at j'th aerodynamic grid point.

$Q^{ij}_{aa}(M,k)$ : Aerodynamic Force Coefficient on i'th structural d.o.f. due to unit displacement at j'th structural d.o.f. where the structural d.o.f. are expressed in a-set.

$Q^{ij}{}_{mm}(M,k)$ : Aerodynamic Force Coefficient on i'th structural mode due to unit modal displacement at j'th structural mode.

The transformation between different sets is carried out as follows :

$$[Q^{ij}{}_{aa}] = [G^T{}_{ka}][Q^{ij}{}_{kk}][G_{ka}] \qquad (2.10)$$

$$[Q^{ij}{}_{mm}] = [\phi^T{}_{am}][Q^{ij}{}_{aa}][\phi_{am}] \qquad (2.11)$$

Where $G_{ka}$ is the spline matrix that transfers forcing from the aerodynamic grid to the structural grid.

Relating the GAF matrix to the structural displacements and the dynamic pressure, aerodynamic forcing vector is obtained:

$$\{F_m(x,\dot{x},\ddot{x},t)\} = q[Q_{mm}(x,\dot{x},\ddot{x},t)]\{\zeta_m(t)\} \qquad (2.12)$$

Note that (2.12) is defined for a single Mach number and a single reduced frequency. Therefore it can be used for classical flutter analysis but cannot be used for transient response analysis.

### 2.2.1.4    Rational Function Approximations

Aeroservoelastic formulation of the missile control fin requires transient aerodynamic effects to be modeled. GAF matrices obtained by DLM are defined for a Mach number and a reduced frequency pair. This is because; DLM calculates the lifting pressure due to a single frequency harmonic oscillation of the aerodynamic surface. Elements of a GAF matrix are complex functions of a single reduced frequency. On the other hand, to calculate the transient aerodynamic effects on an aerodynamic surface in a flow, one needs the continuous frequency domain representation of unsteady aerodynamics [37].

Suppose that we are interested in a structural natural frequency region of fixed bandwidth $f_{max}$, set by the dominant dynamics of the problem, again for a fixed Mach number. If it were possible to generate GAF matrices at each and every frequency from zero to $f_{max}$, then a linear and full frequency response model of the aerodynamics up to $f_{max}$ would be obtained. Then by Fourier Transform methods, it would be possible to obtain the exact time response corresponding to the specified bandwidth, including the transient effects [38].

Unfortunately, it is impossible to generate GAF matrices at every frequency, as there is an infinite number of frequencies between zero and $f_{max}$. Rational Function Approximations to unsteady aerodynamics was proposed by Vepa [13] to utilize the oscillatory aerodynamic coefficients in GAF matrices at specific frequencies, to obtain a continuous frequency domain representation of unsteady aerodynamics. Later, a variety of RFA methods emerged. Today the most frequently used RFA methods are Roger's Method [15] and Karpel's Minimum State Approximation Method[23]. In this thesis, Roger's Method is used. All RFA methods depend on least square techniques, which fit a frequency response function to GAF matrices at multiple reduced frequencies. Comparisons of accuracy and computational efficiency between these methods are available in literature [24] and are out of the scope of this thesis.

Roger's Method approximates the unsteady aerodynamics with following frequency response function that depends on reduced frequency and Mach number:

$$[\bar{Q}(M,k)] = [A_0] + (ik)[A_1] + (ik)^2[A_2] + \sum_{n=1}^{N} \frac{(ik)[A_{n+2}]}{ik + \beta_n} \qquad (2.13)$$

$\beta$ : Roots of Aerodynamic Lag Functions

$N$ : Number of Aerodynamic Lag States

In Eqn. (2.13), $A_{0...N+2}$ are the constant matrices to be determined from least square approximation for the best fit of $Q(M,k)$. $\beta_n$ are the aerodynamic lag roots. $\beta_n$ are preset to specific values in the frequency range of interest, so that the aerodynamic lag functions are stable, the least square problem becomes linear, and the fit is satisfactory. Note that for each element of $Q(M,k)$ at different frequencies $Q^{ij}(M,k_1), Q^{ij}(M,k_2)$. $Q^{ij}(M,k_{n_k})$, a least square fit is generated. Given a $Q(M,k)$ matrix of size $n_m$ at a Mach number, the number of linear least square fits required is $n_m{}^2 x n_k$, where $n_k$ is the number of GAF matrices at $n_k$ different reduced frequencies. $\beta_n$ are the same for each fit, so that the size of the resulting aeroelastic equation is kept small. By modeling the unsteady aerodynamics with Roger's Method, number of states of the resulting aeroelastic equation will be $n_s(N+2)$, where $n_s$ is the number of elastic modal degrees of freedom.

To calculate $A^{ij}{}_{0...N+2}$ for a Mach number, $\overline{Q}^{ij}(M,k)$ is divided into real and imaginary parts such that:

$$[\overline{Q}^{ij}(M,k)] = [\overline{Q}_R^{ij}(M,k)] + i[\overline{Q}_I^{ij}(M,k)] \tag{2.14}$$

$$[\overline{Q}_R^{ij}(M,k)] = [A^{ij}{}_0] - k^2[A^{ij}{}_2] + \sum_{n=1}^{N} \frac{k^2[A^{ij}{}_{n+2}]}{k^2 + \beta_n{}^2} \tag{2.15}$$

$$[\overline{Q}_I^{ij}(M,k)] = k[A^{ij}{}_1] + \sum_{n=1}^{N} \frac{\beta_n k[A^{ij}{}_{n+2}]}{k^2 + \beta_n{}^2} \tag{2.16}$$

Then these parts are written in matrix form, for each Mach - reduced frequency pair:

$$[\overline{Q}_R^{ij}(M,k_f)] = \{K_{Rf}\}[A^{ij}] \tag{2.17}$$

$$[\overline{Q}_I^{ij}(M,k_f)] = \{K_{If}\}[A^{ij}] \tag{2.18}$$

where $K_{Rf}$, $K_{If}$ and $A^{ij}$ are defined as:

$$K_{Rf} = \begin{bmatrix} 1 & 0 & -k_f{}^2 & \dfrac{k_f{}^2}{k_f{}^2 + \beta_1{}^2} & \dfrac{k_f{}^2}{k_f{}^2 + \beta_2{}^2} & \cdots & \dfrac{k_f{}^2}{k_f{}^2 + \beta_N{}^2} \end{bmatrix} \tag{2.19}$$

$$K_{If} = \begin{bmatrix} 0 & k_f & 0 & \dfrac{\beta_1 k_f}{k_f{}^2 + \beta_1{}^2} & \dfrac{\beta_2 k_f}{k_f{}^2 + \beta_2{}^2} & \cdots & \dfrac{\beta_N k_f}{k_f{}^2 + \beta_N{}^2} \end{bmatrix} \tag{2.20}$$

$$A^{ij} = \begin{bmatrix} A^{ij}{}_0 & A^{ij}{}_1 & A^{ij}{}_2 & A^{ij}{}_3 \cdots & A^{ij}{}_{(N+2)} \end{bmatrix}^T \tag{2.21}$$

Then the following complex error function is defined for linear least square minimization problem:

$$[E^{ij}(M,k_f)] = [Q^{ij}(M,k_f)] - [\overline{Q}^{ij}(M,k_f)] \tag{2.22}$$

The aim is to make a linear least square fit, so that the left hand side of Eqn. (2.22) is minimized. Then,

$$\frac{\partial}{\partial A^{ij}_f} \sum_{n=1}^{n_k} (E^{ij}(M,k_f)E^{ij}(M,k_f)') = 0 \tag{2.23}$$

Eqn. (2.23) is solved to obtain[39] :

$$A^{ij} = \left[ \sum_{f=1}^{n_k} \{K_{Rf}\}^T \{K_{Rf}\} + \{K_{If}\}^T \{K_{If}\} \right]^{-1} \sum_{f=1}^{n_k} [Q_{Rf}]\{K_{Rf}\}^T + [Q_{If}]\{K_{If}\}^T \tag{2.24}$$

When all $A^{ij}$ is calculated for each element of $\overline{Q}(M,k)$, one obtains a fit with respect to reduced frequency $k$. In order to use $\overline{Q}(M,k)$ in time domain simulations and frequency domain analysis, it is expressed in Laplace domain with the help of the following equations:

$$k = \frac{\omega b}{U} \tag{2.25}$$

$$s = \sigma + i\omega \tag{2.26}$$

As the GAF matrix is purely oscillatory in $\omega$:

$$\sigma = 0 \tag{2.27}$$

Then by using Eqn. (2.25), Eqn. (2.26) and Eqn. (2.27), the GAF matrix is expressed in Laplace domain as :

$$[\overline{Q}(M,s)] = [A_0] + \frac{sb}{U}[A_1] + \left(\frac{sb}{U}\right)^2 [A_2] + \sum_{n=1}^{N} \frac{s[A_{n+2}]}{s + \frac{U}{b}\beta_n} \tag{2.28}$$

GAF matrices are obtained from MSC NASTRAN in the aerodynamic set, namely the k-set. The matrices are transformed to the m-set as shown in Eqn. (2.10) and Eqn. (2.11). Then Roger's method is applied on the m-set GAF matrices to obtain $\overline{Q}_{mm}(M,s)$. As m-set includes a rigid body mode which accounts for actuator input, $\overline{Q}_{mm}(M,s)$ includes the aerodynamic coefficients that account for rigid body motion of the fin.

In Eqn. (2.28), the number of aerodynamic lag roots is determined so that a satisfactory fit for GAF matrices is performed. Typically 2 to 4 lag roots are used in aeroelastic studies [24]. Taking Laplace transform of Eqn. (2.12) and inserting the estimate from Eqn. (2.28), aerodynamic force in Laplace domain is expressed as:

$$\{F_m(s)\} = q[\overline{Q}_{mm}(M,s)]\{\zeta_m(s)\} \tag{2.29}$$

Eqn. (2.29) will be used for constructing the aeroelastic equation of motion in Section 2.4.

## 2.3    Servo-Actuator Modeling Approach

The missile control fin is controlled by a servo-actuation system. The servo-actuation system is made up of a Permanent Magnet Brushless DC Motor, a transmission unit and a PD Controller. In Figure 9, a generic block diagram of a servo-actuator is shown.
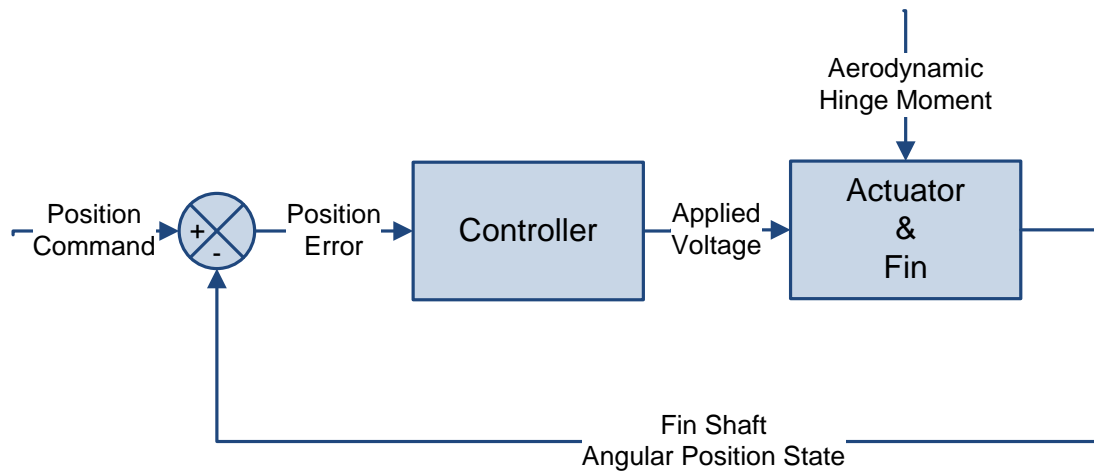
*Figure 9 Block Diagram of Servo-Actuation System*

Linear transfer functions for the servo-actuation system are derived and presented in this section. These transfer functions are used for selecting a suitable DC Motor and transmission unit for actuation, and Root Locus [40] design of the PD controller. No nonlinearity in the actuator is modeled in this chapter. Nonlinear parameters such as dry friction and free play in mechanical linkages are neglected. On the other hand effect of the power limit will be demonstrated by the model developed in MATLAB Simulink in Section 4.3 and Section 5.3.

### 2.3.1   Derivation of Actuator Transfer Function

The DC Motor, together with the transmission unit is called the actuator. The transfer function of the actuator is derived in the following sections.

### 2.3.1.1   The Transmission Unit

In aerospace applications, especially in missile system design, the size of both the servo-actuation system and the power unit is constrained by packaging requirements of the missile. These constraints are commonly reflected on the servo-actuation unit by limiting its diameter and length, and placement in the missile. In turn, these constraints limit the control power that can be obtained from the servo-actuation system and also constrain the axis of the motion created. On the other hand, significant aerodynamic hinge moments on the control surfaces have to be tolerated and the performance of the servo-actuation system should be sustained in a vast range of flight conditions. Therefore a gearbox with a specific speed reduction ratio is commonly used to provide the necessary torque to actuate the fin without performance degradation. In addition, because of the cylindrical shape of the DC Motors used, they are commonly placed in the missile so that the rotational motion of the motor output shaft is parallel to the missile's longitudinal axis, as shown in Figure 10. Therefore there is a need for transmitting the rotational motion of the motor output shaft onto the axis of rotation of the control surface. A transmission unit with speed reduction is commonly used for this purpose.
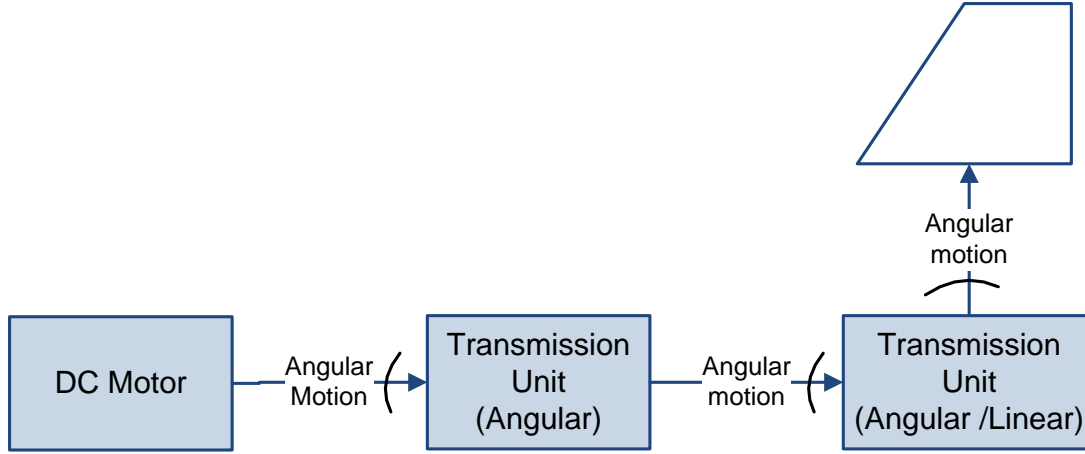
*Figure 10 Common Actuator Placement in Missiles*

The use of a gearbox and/or a transmission unit does not come without cost to the servo-actuation system. Although they increase the torque that can be generated, they also reduce the efficiency of the servo-actuator in terms of mechanical power generation. They also limit the rotational speed that can be obtained at the control surface shaft.

In this thesis, a gearbox and a transmission unit is modeled as a combined transmission unit with a specific speed reduction ratio and efficiency as follows:

$$\theta_m = \theta_{fin} N_{tr} \tag{2.30}$$

$$\dot{\theta}_m = \dot{\theta}_{fin} N_{tr} \tag{2.31}$$

$$\ddot{\theta}_m = \ddot{\theta}_{fin} N_{tr} \tag{2.32}$$

$$J_{total\,@\,motor} = J_{rotor} + J_{gear\,@\,motor} + \frac{J_{fin}}{N_{tr}^2 \eta_{tr}} \tag{2.33}$$

$$T_{hinge\,@\,motor} = \frac{T_{hinge\,@\,fin}}{N_{tr} \eta_{tr}} \tag{2.34}$$

Where the parameters in Eqn. (2.30) to Eqn. (2.34) are defined as:

$J_{rotor}$     : Rotor Inertia (kg.m$^2$)

$J_{gear\,@\,motor}$   : Rotor Inertia (kg.m$^2$)

$T_{hinge\,@\,motor}$   : Hinge Moment on the Motor (N.m)

$T_{hinge\,@\,fin}$   : Hinge Moment on the Fin (N.m)

$\theta_m$     : Angular Position of Motor Shaft

$\theta_{fin}$     : Angular Position of Fin Shaft

$N_{tr}$     : Combined Speed Reduction Ratio

$\eta_{tr}$     : Combined Efficiency

$J_{rotor}$ and $J_{gear\,@\,motor}$ are obtained from the motor catalog and $J_{fin}$ is obtained from the MSC PATRAN finite element model.

### 2.3.1.2    The DC Motor

Dynamic characteristics of a DC Motor are often given in motor catalogs in terms of constant parameters. As long as the DC Motor is used according to the operating conditions that are specified in the catalog such as nominal voltage and max load torque, these parameters are valid for the motor's entire lifecycle. The parameters are listed below:

$V$ : Nominal Voltage (Volts)

$K_t$ : Torque Constant (N.m / Amperes)

$K_b$ : Back EMF constant (Volts.s / radians)

$R$ : Armature Resistance (Ohms)

$L$ : Aramature Inductance (Henries)

$c$ : Viscous Damping Coefficient (N.m.s / radians)

In Figure 11, free body diagram of the DC Motor is shown.
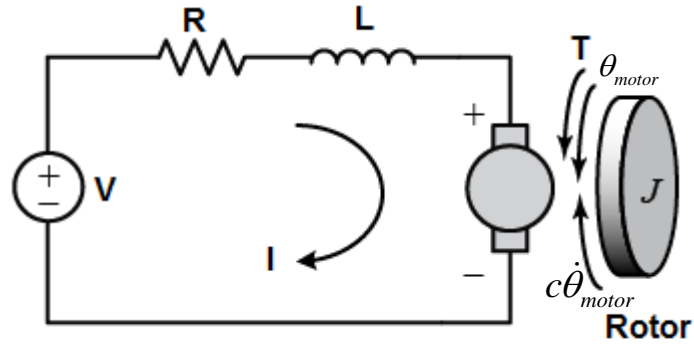


*Figure 11 Free Body Diagram of DC Motor*

According to Figure 9 and Figure 11, equation of motion can be expressed at motor output shaft as follows:

$$T_i(t) + T_{hinge\,@\,motor}(t) - c\dot{\theta}_{motor}(t) = J_{total\,@\,motor}\ddot{\theta}(t) \tag{2.35}$$

$$V_i(t) - I(t)R - \dot{\theta}_{motor}(t)K_b = L\dot{I}(t) \tag{2.36}$$

Where $T_i$ is the torque applied by armature current such that;

$$T_i(t) = K_t I(t) \tag{2.37}$$

Eqn. (2.37) is inserted in Eqn. (2.35), and the resulting equation is transformed to Laplace domain such that;

$$I(s) = \frac{s\theta_{motor}(s)\left(J_{total\,@\,motor}s + c\right) - T_{hinge\,@\,motor}(s)}{K_t} \tag{2.38}$$

Aerodynamic load torque $T_{hinge\,@\,motor}(s)$ is assumed to be a disturbance torque; therefore it is commonly discarded from Eqn. (2.38) for controller design purposes. The PD controller designed will treat the aerodynamic load torque as an unknown disturbance. This is often done to enhance the

robustness to uncertainty in the aerodynamic hinge moment. Note that, $T_{hinge\ @\ motor}(s)$ will be included in aeroservoelastic system simulations. Then Eqn. (2.36) becomes:

$$I(s) = \frac{V_i(s) - s\theta_m(s)K_b}{(Ls + R)}$$

(2.39)

Then Eqn. (2.38) and Eqn. (2.39) are equated so that an input – output relationship between input voltage $V_i$ and motor shaft position $\theta_{motor}$ is obtained:

$$\frac{\theta_m(s)}{V_i(s)} = \frac{K_t}{s\left(\left(J_{total\ @\ motor}s + c\right)(Ls + R) + K_bK_t\right)}$$

(2.40)

### 2.3.1.3    The Actuator Transfer Function

Eqn. (2.40) is the transfer function of the actuator that is composed of the DC motor and the transmission unit. The transmission unit may include a gear box and/or other mechanisms. The total transmission ratio and efficiency of a transmission unit defined in Section 4.1 are inserted in Eqn. (2.40), such that the output position is now at the output of the transmission unit. When the fin is assumed to be both rigid and rigidly connected to the transmission, the output of the transmission unit is equivalent to the output of the fin.

$$\frac{\theta_{fin}(s)}{V_i(s)} = \frac{K_t}{Ns\left(\left(J_{total\ @\ motor}s + c\right)(Ls + R) + K_bK_t\right)}$$

(2.41)

### 2.3.2    Derivation of Closed Loop Servo-Actuation System Transfer Function

A PD controller is cascaded to the actuator transfer function given in Eqn. (2.41) and a unity feedback closed loop system is formed as shown in Figure 9. Sensor dynamics and error characteristics are neglected, as if the angular position of the fin shaft is perfectly known. In this thesis, the effects of the dynamics of the sensors on the aeroservoelastic loop are not sought after. Transfer function of a PD controller is:

$$G_{PD}(s) = K_P + K_D s$$

(2.42)

The resulting closed loop transfer function is:

$$\frac{\theta_{fin}}{\theta_{com}} = \frac{K_DK_ts + K_PK_t}{NJLs^3 + N\left(J_{total\ @\ motor}R + cL\right)s^2 + \left(N\left(K_bK_t + cR\right) + K_tK_D\right)s + K_PK_t}$$

(2.43)

$\theta_{com}$ is the commanded fin deflection.

## 2.4    Integration of Structural and Aerodynamic Models

As the Laplace domain expressions of the structural and the aerodynamic models are obtained from Eqn. (2.6) and Eqn. (2.29), they can now be used to form the aeroelastic model. Aeroelastic dynamics of the missile control fin can be expressed in the Laplace domain as follows:

$$\left( s^2 \left[ \mathbf{M}_{mm} \right] + s \left[ \mathbf{C}_{mm} \right] + \left[ \mathbf{K}_{mm} \right] - q[\overline{\mathbf{Q}}(M,s)] \right) \left\{ \zeta_m(s) \right\} = \left\{ T_{act}(s) \right\} \tag{2.44}$$

In Eqn. (2.44), $T_{act}(s)$ is the moment applied by the actuator to the fin. The m-set matrices are obtained by the modal transformation using the truncated modeshape matrix $\phi_{am}$, which is composed of a rigid body mode, and several elastic modes. The rigid body mode accounts for the actuator input control deflection. $\phi_{am}$ is expressed as:

$$\phi_{am} = \left[ \phi_{ac} \quad \phi_{as} \right] \tag{2.45}$$

In Eqn. (2.45), $\phi_{ac}$ is the rigid body mode column vector, and $\phi_{as}$ is the modeshape matrix that includes elastic modeshapes as column vectors. Then, the m-set equation of motion is partitioned into rigid and elastic modal coordinates, c-set and s-set respectively:

$$\left( s^2 \begin{bmatrix} \mathbf{M}_{cc} & \mathbf{M}_{cs} \\ \mathbf{M}_{sc} & \mathbf{M}_{ss} \end{bmatrix} + s \begin{bmatrix} 0 & 0 \\ 0 & \mathbf{C}_{ss} \end{bmatrix} + \begin{bmatrix} 0 & 0 \\ 0 & \mathbf{K}_{ss} \end{bmatrix} - q \begin{bmatrix} \overline{\mathbf{Q}}_{cc} & \overline{\mathbf{Q}}_{cs} \\ \overline{\mathbf{Q}}_{sc} & \overline{\mathbf{Q}}_{ss} \end{bmatrix} \right) \begin{Bmatrix} \zeta_c(s) \\ \zeta_s(s) \end{Bmatrix} = \begin{Bmatrix} T_{fin}(s) \\ 0 \end{Bmatrix} \tag{2.46}$$

In Eqn. (2.46), inertial coupling between rigid and elastic modes is modeled. There is no coupling in damping and stiffness terms in the equation of motion. Damping and stiffness are not defined for rigid body motion. Aerodynamic force is also coupled between rigid body and elastic modes.

Eqn. (2.46) can be rewritten in two equation sets as follows :

$$\left( s^2 \mathbf{M}_{cs} - q\overline{\mathbf{Q}}_{cs} \right) \zeta_s(s) + \left( s^2 \mathbf{M}_{cc} - q\overline{\mathbf{Q}}_{cc} \right) \zeta_c(s) = T_{fin}(s) \tag{2.47}$$

$$\left( s^2 \mathbf{M}_{ss} + s\mathbf{C}_{ss} + \mathbf{K}_{ss} - q\overline{\mathbf{Q}}_{ss} \right) \zeta_s(s) + \left( s^2 \mathbf{M}_{sc} - q\overline{\mathbf{Q}}_{sc} \right) \zeta_c(s) = 0 \tag{2.48}$$

In Eqn. (2.47), the coupling between rigid body dynamics with aeroelastic dynamics is introduced by inertial and aerodynamic coupling on $\zeta_s(s)$, the elastic modal coordinate vector.

In Eqn. (2.48), the coupling between rigid body dynamics with aeroelastic dynamics is introduced by inertial and aerodynamic coupling on $\zeta_c(s)$, the rigid body modal coordinate, which is the actuator output $\theta_{fin}(s)$.

The total hinge moment acting on the transmission unit output shaft, including the aerodynamic and the inertial components is:

$$T_{hinge @ fin}(s) = -T_{fin}(s) \tag{2.49}$$

The aerodynamic forces in Eqn. (2.47) and Eqn. (2.48) are expressed as:

$$\mathbf{F}_m(s) = q \begin{bmatrix} \overline{\mathbf{Q}}_{cc} & \overline{\mathbf{Q}}_{cs} \\ \overline{\mathbf{Q}}_{sc} & \overline{\mathbf{Q}}_{ss} \end{bmatrix} \begin{Bmatrix} \zeta_c(s) \\ \zeta_s(s) \end{Bmatrix} \tag{2.50}$$

Then let,

$$\mathbf{F}_m(s) = \begin{bmatrix} \mathbf{F}_{cc} & \mathbf{F}_{cs} \\ \mathbf{F}_{sc} & \mathbf{F}_{ss} \end{bmatrix} \begin{Bmatrix} \zeta_c(s) \\ \zeta_s(s) \end{Bmatrix} \tag{2.51}$$

Partitioning least square coefficient matrices $\mathbf{A}_0$ to $\mathbf{A}_{N+2}$ in Eqn. (2.28) into rigid body and elastic modal coordinates and inserting into Eqn. (2.51):

25

$$F_{cc}(s) = 0.5\rho U^2 A_{cc_0} + 0.5\rho bU A_{cc_1} s + 0.5\rho b^2 A_{cc_2} s^2 + 0.5\rho U^2 x^l_{cc}(s) \tag{2.52}$$

$$F_{cs}(s) = 0.5\rho U^2 A_{cs_0} + 0.5\rho bU A_{cs_1} s + 0.5\rho b^2 A_{cs_2} s^2 + 0.5\rho U^2 x^l_{cs}(s) \tag{2.53}$$

$$F_{sc}(s) = 0.5\rho U^2 A_{sc_0} + 0.5\rho bU A_{sc_1} s + 0.5\rho b^2 A_{sc_2} s^2 + 0.5\rho U^2 x^l_{sc}(s) \tag{2.54}$$

$$F_{ss}(s) = 0.5\rho U^2 A_{ss_0} + 0.5\rho bU A_{ss_1} s + 0.5\rho b^2 A_{ss_2} s^2 + 0.5\rho U^2 x^l_{ss}(s) \tag{2.55}$$

For any of the above cc, cs, sc and ss sets of $x^l(s)$:

$$x^l(s) = \sum_{n=1}^{N} \frac{s A_{n+2}}{s + \dfrac{U}{b}\beta_n} \tag{2.56}$$

Note that all sets of $A_0$ to $A_{N+2}$ are obtained from the Roger's Method as applied in Section 2.2.1.4. Then Eqn. (2.47) and Eqn. (2.48) become:

$$\left(s^2 \mathbf{M}_{cs} - F_{cs}(s)\right)\zeta_s(s) + \left(s^2 \mathbf{M}_{cc} - F_{cc}(s)\right)\zeta_c(s) = T_{fin}(s) \tag{2.57}$$

$$\left(s^2 \mathbf{M}_{ss} + s\mathbf{C}_{ss} + \mathbf{K}_{ss} - F_{ss}(s)\right)\zeta_s(s) + \left(s^2 \mathbf{M}_{sc} - F_{sc}(s)\right)\zeta_c(s) = 0 \tag{2.58}$$

When Eqn. (2.52), Eqn. (2.53), Eqn. (2.54) and Eqn. (2.55) are inserted into Eqn. (2.57) and Eqn. (2.58):

$$\begin{aligned}
&\left(s^2 \bar{\mathbf{M}}_{cs} + s\bar{\mathbf{C}}_{cs} + \bar{\mathbf{K}}_{cs} - q x^l_{cs}(s)\right)\zeta_s(s) + \\
&\left(s^2 \bar{\mathbf{M}}_{cc} + s\bar{\mathbf{C}}_{cc} + \bar{\mathbf{K}}_{cc} - q x^l_{cc}(s)\right)\zeta_c(s) = T_{fin}(s)
\end{aligned} \tag{2.59}$$

$$\begin{aligned}
&\left(s^2 \bar{\mathbf{M}}_{ss} + s\bar{\mathbf{C}}_{ss} + \bar{\mathbf{K}}_{ss} - q x^l_{ss}(s)\right)\zeta_s(s) + \\
&\left(s^2 \bar{\mathbf{M}}_{sc} + s\bar{\mathbf{C}}_{sc} + \bar{\mathbf{K}}_{sc} - q x^l_{sc}(s)\right)\zeta_c(s) = 0
\end{aligned} \tag{2.60}$$

Where the aeroelastic matrices in Eqn. (2.59) and Eqn. (2.60) are expressed as:

$$\bar{\mathbf{M}}_{cs} = \mathbf{M}_{cs} - \frac{\rho b^2}{2} A_{cs_2} \qquad\qquad \bar{\mathbf{M}}_{cc} = \mathbf{M}_{cc} - \frac{\rho b^2}{2} A_{cc_2}$$

$$\bar{\mathbf{C}}_{cs} = -\frac{\rho bU}{2} A_{cs_1} \qquad\qquad \bar{\mathbf{C}}_{cc} = -\frac{\rho bU}{2} A_{cc_1}$$

$$\bar{\mathbf{K}}_{cs} = -\frac{\rho U^2}{2} A_{cs_0} \qquad\qquad \bar{\mathbf{K}}_{cc} = -\frac{\rho U^2}{2} A_{cc_0}$$

$$\bar{\mathbf{M}}_{ss} = \mathbf{M}_{ss} - \frac{\rho b^2}{2} A_{ss_2} \qquad\qquad \bar{\mathbf{M}}_{sc} = \mathbf{M}_{sc} - \frac{\rho b^2}{2} A_{sc_2}$$

$$\bar{\mathbf{C}}_{ss} = \mathbf{C}_{ss} - \frac{\rho bU}{2} A_{ss_1} \qquad\qquad \bar{\mathbf{C}}_{sc} = -\frac{\rho bU}{2} A_{sc_1}$$

$$\bar{\mathbf{K}}_{ss} = \mathbf{K}_{ss} - \frac{\rho U^2}{2} A_{ss_0} \qquad\qquad \bar{\mathbf{K}}_{sc} = -\frac{\rho U^2}{2} A_{sc_0}$$

Two types of aerodynamic lag states are defined so that a state space formulation for the solution of $\zeta_s(s)$ is constructed. The aeroelastic hinge moment lag state is:

$$\zeta_{c_{an}}(s) = \frac{sA_{cs_{n+2}}}{s + \dfrac{U}{b}\beta_n}\zeta_s(s) + \frac{sA_{cc_{n+2}}}{s + \dfrac{U}{b}\beta_n}\zeta_c(s) \tag{2.61}$$

The lag state for aeroelastic equation of motion is:

$$\zeta_{s_{an}}(s) = \frac{sA_{ss_{n+2}}}{s + \dfrac{U}{b}\beta_n}\zeta_s(s) + \frac{sA_{sc_{n+2}}}{s + \dfrac{U}{b}\beta_n}\zeta_c(s) \tag{2.62}$$

$\zeta_{c_{an}}(s)$ is used for constructing the hinge moment as an output of the state space aeroelastic system model. Otherwise, if the hinge moment was not necessary as an output, definition of $\zeta_{s_{an}}(s)$ would be enough for solving Eqn. (2.60) for $\zeta_s(s)$.

Then the state space formulation of Eqn. (2.60) augmented with hinge moment lag states is:

$$\{\dot{z}(t)\} = \left[A_{sys}\right]\{z(t)\} + \left[B_{sys}\right]\{u(t)\} \tag{2.63}$$

Where the system and input matrices are expressed as:

$$\left[A_{sys}\right] = \begin{bmatrix} 0 & I & 0 & 0 \\ -\bar{\mathbf{M}}_{ss}^{-1}\bar{\mathbf{K}}_{ss} & -\bar{\mathbf{M}}_{ss}^{-1}\bar{\mathbf{C}}_{ss} & q\bar{\mathbf{M}}_{ss}^{-1}D_s & 0 \\ 0 & E_{ss} & \dfrac{U}{b}R_{ss} & 0 \\ 0 & E_{cs} & 0 & \dfrac{U}{b}R_{cs} \end{bmatrix} \qquad \{z(t)\} = \begin{Bmatrix} \zeta_s(t) \\ \dot{\zeta}_s(t) \\ \zeta_{s_{a1}}(t) \\ \dots \\ \zeta_{s_{aN}}(t) \\ \zeta_{c_{a1}}(t) \\ \dots \\ \zeta_{c_{aN}}(t) \end{Bmatrix}$$

$$\left[B_{sys}\right] = \begin{bmatrix} 0 & I & 0 \\ \bar{\mathbf{M}}_{ss}^{-1}\bar{\mathbf{K}}_{sc} & \bar{\mathbf{M}}_{ss}^{-1}\bar{\mathbf{C}}_{sc} & -\bar{\mathbf{M}}_{ss}^{-1}\bar{\mathbf{M}}_{sc} \\ 0 & E_{sc} & 0 \\ 0 & E_{cc} & 0 \end{bmatrix} \qquad \{u(t)\} = \begin{Bmatrix} \zeta_c(t) \\ \dot{\zeta}_c(t) \\ \ddot{\zeta}_c(t) \end{Bmatrix}$$

Where zeros and $I$'s represent zero and identity matrices respectively, and also;

$$E_{ss} = \left\{ \begin{array}{c} A_{ss_3} \\ A_{ss_4} \\ ... \\ A_{ss_{N+2}} \end{array} \right\} \qquad E_{sc} = \left\{ \begin{array}{c} A_{sc_3} \\ A_{sc_4} \\ ... \\ A_{sc_{N+2}} \end{array} \right\} \qquad R_{ss} = \begin{bmatrix} -\beta_1 & 0 & 0 & 0 \\ 0 & -\beta_2 & 0 & 0 \\ 0 & 0 & ... & 0 \\ 0 & 0 & 0 & -\beta_N \end{bmatrix}$$

$$E_{cs} = \left\{ \begin{array}{c} A_{cs_3} \\ A_{cs_4} \\ ... \\ A_{cs_{N+2}} \end{array} \right\} \qquad E_{cc} = \left\{ \begin{array}{c} A_{cc_3} \\ A_{cc_4} \\ ... \\ A_{cc_{N+2}} \end{array} \right\} \qquad R_{cs} = R_{ss} = \begin{bmatrix} -\beta_1 & 0 & 0 & 0 \\ 0 & -\beta_2 & 0 & 0 \\ 0 & 0 & ... & 0 \\ 0 & 0 & 0 & -\beta_N \end{bmatrix}$$

$$D_s = \begin{bmatrix} I_1 & I_2 & ... & I_N \end{bmatrix}$$

Above, $D_s$ is composed of N identity matrices of size equal to number of elastic modal coordinates.

Eqn. (2.63) is the aeroelastic state space system model that is used in Section 5.1, where it is cascaded to the electromechanical actuation system model in MATLAB Simulink environment. The solution of the resulting model is carried out in MATLAB Simulink by a numerical integration method.

The output of the aeroelastic state space system model is formulated, so that the actual displacements at global coordinates, and the hinge moment acting on the fin is calculated. In order to obtain global displacements, modal superposition is used as follows:

$$x(t) = \begin{bmatrix} \phi_{as} \end{bmatrix} \{ \zeta_s(t) \} + \begin{bmatrix} \phi_{ac} \end{bmatrix} \{ \zeta_c(t) \} \tag{2.64}$$

In order to express hinge moment in terms of states $z$ and inputs $u$, using Eqn. (2.49) and Eqn. (2.59):

$$T_{hinge @ fin}(s) = T_{hinge @ fin}^{state}(s) + T_{hinge @ fin}^{input}(s) \tag{2.65}$$

$$T_{hinge @ fin}^{state}(s) = \left( -s^2 \bar{M}_{cs} - s\bar{C}_{cs} - \bar{K}_{cs} + q x_{cs}^l(s) \right) \zeta_s(s) \tag{2.66}$$

$$T_{hinge @ fin}^{input}(s) = \left( -s^2 \bar{M}_{cc} - s\bar{C}_{cc} - \bar{K}_{cc} + q x_{cc}^l(s) \right) \zeta_c(s) \tag{2.67}$$

Formulating Eqn. (2.66) and Eqn. (2.67) in state space, the hinge moment is formulated as an output:

$$T_{hinge @ fin}(t) = \begin{bmatrix} C_{hinge @ fin} \end{bmatrix} \{ z(t) \} + \begin{bmatrix} D_{hinge @ fin} \end{bmatrix} \{ u(t) \} \tag{2.68}$$

Where the output matrix and the direct transition matrix are defined as:

$$C_{hinge @ fin} = \begin{bmatrix} -\bar{K}_{cs} & -\bar{C}_{cs} & 0 & q D_c \end{bmatrix} - \bar{M}_{cs} \bar{M}_{ss}^{-1} \begin{bmatrix} -\bar{K}_{ss} & -\bar{C}_{ss} & q D_s & 0 \end{bmatrix} \tag{2.69}$$

$$D_{hinge @ fin} = \begin{bmatrix} -\bar{K}_{cc} & -\bar{C}_{cc} & -\bar{M}_{cc} \end{bmatrix} - \bar{M}_{cs} \bar{M}_{ss}^{-1} \begin{bmatrix} \bar{K}_{sc} & \bar{C}_{sc} & -\bar{M}_{sc} \end{bmatrix} \tag{2.70}$$

Where $D_c$ is an N size row vector composed of 1's.

Eqn. (2.63), Eqn. (2.64) and Eqn. (2.68) form the state space aeroelastic system model together with its outputs, displacements in global coordinates and total hinge moment around the fin.

Note that the total hinge moment acting on the motor output shaft is:

$$T_{hinge\,@\,motor}(t) = \frac{T_{hinge\,@\,fin}(t)}{N_{tr}\eta_{tr}} \qquad (2.71)$$

# CHAPTER 3

# AEROELASTIC MODELING

This chapter of the thesis is devoted to clarifying the aeroelastic modeling steps followed in MSC NASTRAN. In this thesis, there has been put a considerable amount of effort to extract information from MSC® NASTRAN solvers and reformulate the problem in MATLAB as a state space model. In order to be able to verify that this interfacing step did not bring any mistakes; normal modes analysis and flutter analysis are performed on both software platforms, and the results are verified.

## 3.1    Structural Modeling

Finite element modeling of the fin, whose geometric properties are given in Figure 3 and Figure 4 is performed, so that the normal modes analysis and flutter analysis is performed in MSC NASTRAN. Two separate finite element models are constructed for different purposes. Outputs of the second model are used in subsequent aeroelastic analysis in MATLAB. The material of the fin is aluminum, whose modulus of elasticity is 70 GPa. Poisson's ratio is taken as 0.3.

## 3.1.1    Finite Element Modeling in MSC® PATRAN

The first model is prepared for flutter analysis, and normal modes analysis for elastic modes. The fin is connected to the actuator through a shaft. This shaft is assumed to be rigid in all five degrees of freedom except the rotational one in y-axis. It is assumed that the shaft reflects the resultant static stiffness of the actuator and the connecting shaft. In y-axis, it has a stiffness of 120 N.m/rad. The rotational stiffness value and the planform shape of the fin is taken from [50], but the thickness of the fin is different from the specified reference. To model this shaft connection, a point on the ground is generated such that it is fixed in all degrees of freedom. The mid-node on the root chord of the fin is rigidly connected to this point through a multi point constraint (MPC), such that all five degrees of freedom except the rotational one in y-axis is fixed for this node. The rotational stiffness of the shaft in y-axis is modeled by a one dimensional bar element, which has no mass or inertia, and has 120 N.m/rad rotational stiffness. The model is shown in Figure 12. Element 43 is the bar element. The fin structure is modeled with 42 QUAD4 elements.
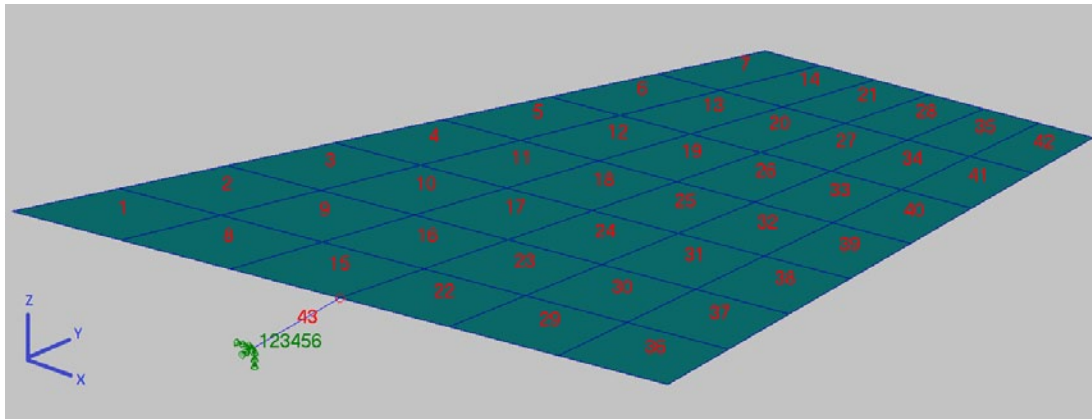
*Figure 12 Finite Element Model FN1*

A second model is prepared, so that the rigid body mode is obtained together with the elastic modes, without affecting the shapes and natural frequencies of the elastic modes. The rigid body mode is generated so that it is used in modeling the rigid control motion of the actuator. For this purpose, the boundary condition on the point on the ground is modified such that it is disconnected from the ground in y-axis rotational degree of freedom. Therefore, the fin is now free to rotate as a rigid body around y-axis. The problem is that, because the fin is disconnected from the ground, the shapes and frequencies of the elastic modes are now changed. It is needed to obtain the elastic modes, as if the fin is connected to the actuator with 120 N.m/rad rotational stiffness, but at the same time it has to be able to rigidly rotate around y-axis. To generate the needed modes in a single normal modes analysis run in MSC NASTRAN, a very high fictitious inertia [22] is used in y-axis, to mimic the fixed boundary condition at the point on the ground. The fictitious inertia is about $10^6$ times greater than that of the rotational inertia of the fin. This high inertia adds a huge inertial resistance to the motion at the point where it is added, so that in a dynamic analysis, the fin feels a fixed boundary condition for elastic modes, at that point. Therefore the modeshapes and natural frequencies contain a rigid body mode, in addition to the original elastic modeshapes and frequencies obtained for the model FN1. The mass matrix $\mathbf{M}_{mm}$ is now changed, but the additional inertia is discarded from $\mathbf{M}_{mm}$ when it is used in subsequent aeroelastic analysis in MATLAB. The model is shown in Figure 13, together with the changed boundary condition and the place the fictitious inertia added. CMASS1 element is used for the added inertia. A SUPORT[28] statement is inserted into the Bulk Data Section of MSC PATRAN flutter analysis menu[41], so that the rigid body mode obtained has exactly zero natural frequency.
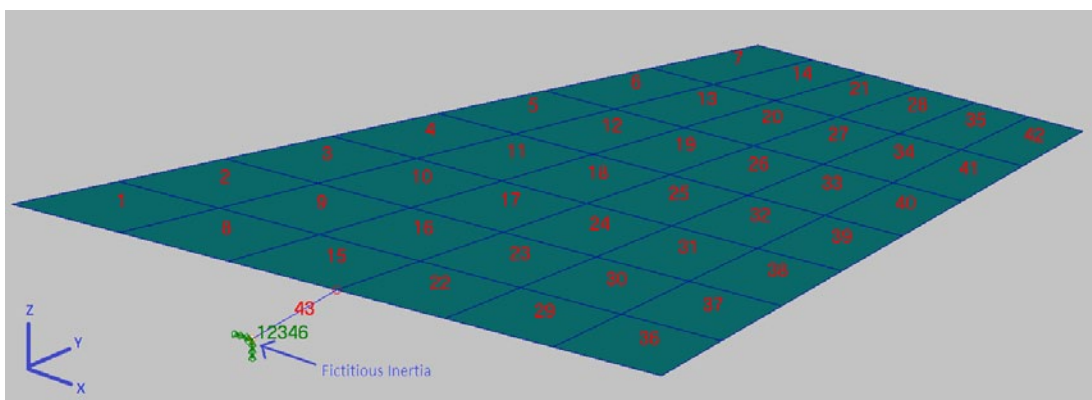


*Figure 13 Finite Element Model FN2*

The obtain structural matrices $\mathbf{M}_{mm}$, $\mathbf{K}_{mm}$, the truncated modeshape matrix $\phi_{am}$, several DMAP codes[42] are inserted into the Executive Control Deck and Case Control Deck, in MSC PATRAN flutter analysis menu[41].

```
$ Direct Text Input for Executive Control
COMPILE SEFLUTTR $
ALTER 114 $
OUTPUT4 MHH,KHH,PHDH,,//0/21 ///30 $
```

*Figure 14 DMAP Code in Executive Control Deck for Structural Matrix Extraction*

The DMAP code in Figure 14 is used to write the structural matrices $\mathbf{M}_{mm}$ and $\mathbf{K}_{mm}$ together with the modal matrix $\phi_{am}$ to a file, so that they are read by MATLAB for further aeroelastic analysis.

```
$ Direct Text Input for Global Case Control Data
RESVEC = NO
SET 100 = 1,3,4,5,6,7
MODESELECT = 100
```

*Figure 15 DMAP Code in Case Control Deck for Mode Selection*

The DMAP code in Figure 15 is used for neglecting structural modes higher than 1000 Hz in subsequent flutter and time response analysis. Modes up to 1000 Hz are included so that an unquestionable accuracy for global displacements is obtained in time simulation. Note that the second structural mode is also neglected although it is in the range below 1000 Hz. This is due to the nature of that mode, being a bending mode around the z-axis, as shown in Figure 16. This type of mode will not affect the aeroelastic analysis because it has no interference with aerodynamics of the fin.
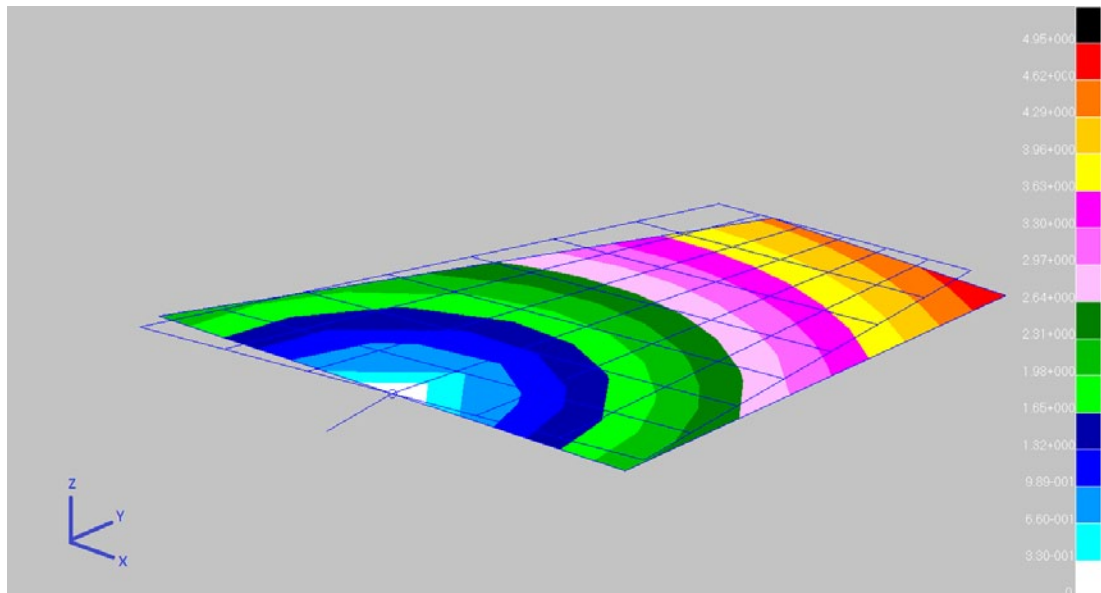


*Figure 16 Discarded Bending Mode of the Fin*

### 3.1.2 Normal Modes Analysis in MSC<sup>®</sup> NASTRAN and MATLAB

The results of the normal modes analysis carried out prior to the flutter analysis are given in Table 4, for both finite element models. Although the modes taken into account for the studies in the following chapters are limited by an upper limit of 1000 Hz, the normal modes analysis for validation of MATLAB implementation is carried with a total number of 10 modes.

*Table 4 Natural Frequency Comparison for FN1 & FN2*

|  | Model FN1 (Hz) | Model FN2 (Hz) |
|---|---|---|
| Rigid Body Mode | - | 0.0000 |
| Elastic Mode 1 | 16.5724 | 16.5724 |
| Elastic Mode 2 | 86.8891 | 86.8891 |
| Elastic Mode 3 | 159.6022 | 159.6022 |
| Elastic Mode 4 | 566.0895 | 566.0895 |
| Elastic Mode 5 | 627.1564 | 627.1564 |
| Elastic Mode 6 | 972.5351 | 972.5351 |
| Elastic Mode 7 | 1308.9220 | 1308.9220 |
| Elastic Mode 8 | 1817.4420 | 1817.4420 |
| Elastic Mode 9 | 1980.2690 | 1980.2690 |

As observed from Table 4, the fictitious inertia worked perfectly and the results obtained for the elastic natural frequencies are identical. Note that the elastic mode 1 is the discarded mode shown in Figure 16. The first four elastic modeshapes other than the discarded one of FN2 are shown in Figure 17.
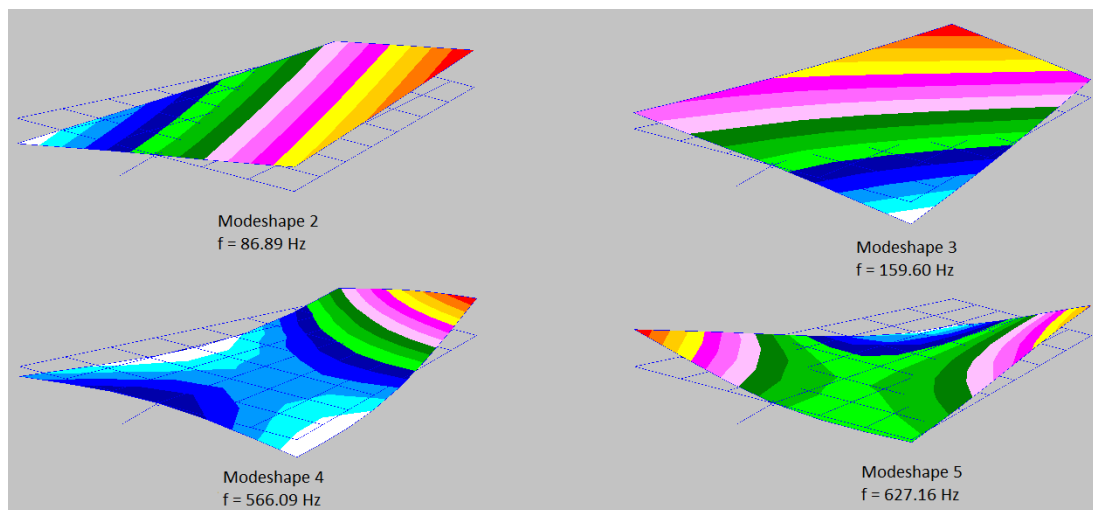


*Figure 17 Elastic Modeshapes 2-to-5*

An additional normal modes analysis is carried out in MATLAB, so that the matrices output from MSC NASTRAN are verified. In MATLAB, the eigenvalue problem solver function 'eig'[43] is used to obtain natural frequencies and modeshapes. The natural frequencies obtained from MATLAB are presented together with the results of MSC NASTRAN for FN2 is given in Table 5.

*Table 5 Natural Frequency Comparison*

|  | Model FN2 (Hz) Nastran Output | Model FN2 (Hz) MATLAB Output |
|---|---|---|
| Rigid Body Mode | 0.0000 | 1.52691E-07 |
| Elastic Mode 1 | 16.5724 | 16.5724 |
| Elastic Mode 2 | 86.8891 | 86.8891 |
| Elastic Mode 3 | 159.6022 | 159.6022 |
| Elastic Mode 4 | 566.0895 | 566.0895 |
| Elastic Mode 5 | 627.1564 | 627.1564 |
| Elastic Mode 6 | 972.5351 | 972.5351 |
| Elastic Mode 7 | 1308.9220 | 1308.9222 |
| Elastic Mode 8 | 1817.4420 | 1817.4419 |
| Elastic Mode 9 | 1980.2690 | 1980.2687 |

The mass normalized rigid body mode and the elastic mode 2 obtained from MSC NASTRAN and MATLAB for FN2 are plotted in Figure 18 and Figure 19, as examples. The x-axis of Figure 18 and Figure 19 shows the elements of a-set degrees of freedom for a modeshape vector. It is observed that the modeshapes are identical. Therefore the stiffness and mass matrices obtained from MSC NASTRAN can be used in further aeroservoelastic analysis with confidence.
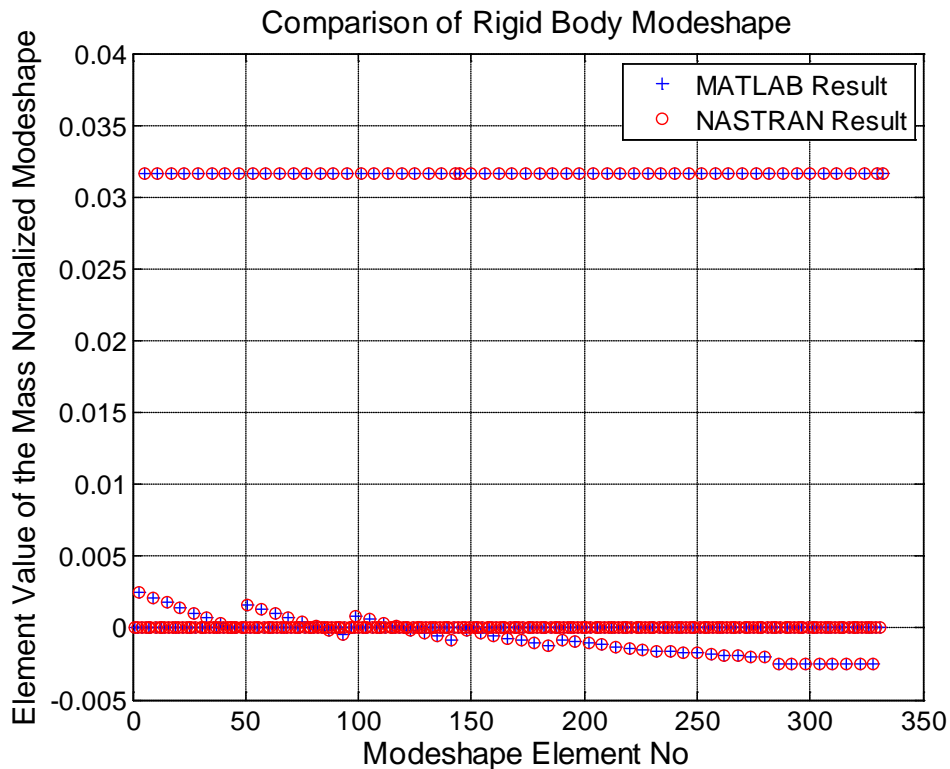


*Figure 18 Rigid Body Modeshape Comparison*
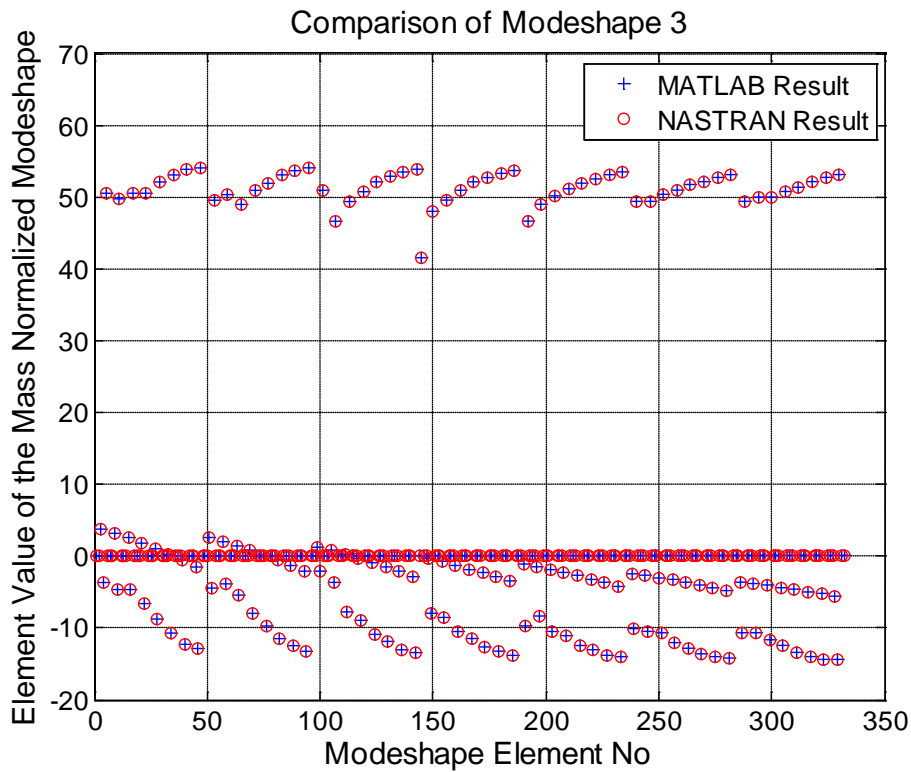
*Figure 19 Elastic Modeshape 3 Comparison*

The number of elastic modes below 1000 Hz is 5. Together with the rigid body mode, 6 structural modes are used in the subsequent analysis in MSC NASTRAN and MATLAB. Natural frequencies of these modes are summarized in Table 6.

*Table 6 Structural Modes used in Aeroservoelastic Analyses*

|  | Model FN2 (Hz) Nastran Output |
| --- | --- |
| Rigid Body Mode | 0.0000 |
| Elastic Mode 2 | 86.8891 |
| Elastic Mode 3 | 159.6022 |
| Elastic Mode 4 | 566.0895 |
| Elastic Mode 5 | 627.1564 |
| Elastic Mode 6 | 972.5351 |

The number of aeroelastic modes used in aeroservoelastic modeling and analysis directly equals the number of elastic modes included in structural modeling. From this point forward in the thesis, the modes that involve elasticity will be called the aeroelastic modes, and the mode that defines the control action will be called the rigid body mode.

### 3.2    Aerodynamic Modeling

Aerodynamic modeling of the missile control fin is carried out in MSC Flightloads and Dynamics, with the Doublet Lattice Method. Unsteady GAF matrices at 4 different Mach numbers are obtained

for a predefined region of reduced frequency. The GAF matrices are used for flutter analysis in both MSC NASTRAN and MATLAB.

### 3.2.1 Unsteady Aerodynamics Modeling in MSC® Flightloads and Dynamics

Unsteady aerodynamic modeling in MSC Flightloads and Dynamics is carried out using following important parameters obtained from the knowledge about the flight envelope.

$$U_{\min} < Mach_{\min@\ max\ altitude} a_{\max\ altitude} \tag{3.1}$$

$$U_{\max} > Mach_{\max@\ min\ altitude} a_{\min\ altitude} \tag{3.2}$$

$$f_{\min} < f_{\min\_structure} \tag{3.3}$$

$$f_{\max} > f_{\max\_structure} \tag{3.4}$$

The parameters on the right hand sides of inequalities (3.1) to (3.4) are defined as:

$Mach_{\min@\ max\ altitude}$ : Min. Mach at max. altitude

$Mach_{\max@\ min\ altitude}$ : Max. Mach at min. altitude

$f_{\min\_structure}$ : Min. structural natural freq. of interest

$f_{\max\_structure}$ : Max. structural natural freq. of interest

$a_{\min\ altitude}$ : Speed of sound at min. altitude

$a_{\max\ altitude}$ : Speed of sound at max. altitude

The parameters $U_{\min}$, $U_{\max}$, $f_{\min}$ and $f_{\max}$ are selected according to inequalities (3.1) to (3.4), and used in subsequent discussions.

Doublet Lattice Modeling of the missile control fin aerodynamics requires certain rules to be followed in MSC Flightloads and Dynamics [43]. Two of them significantly affect the accuracy of aerodynamic forcing and subsequent aeroelastic analysis:

- There should be a minimum of 15 boxes (panels) per wavelength for each chord strip. Not less than four boxes per chord should be used.
- The boxes (panels) should maintain an aspect ratio of less than 3 in the default Doublet-Lattice formulation.

There is couple of other guidelines that could make difference in the results, such as increasing the mesh density at the leading edge, the trailing edge and the control surface tip. Since the resulting mesh when the above rules are taken into account is dense enough, increasing the mesh density further in specific regions do not improve the solution for this case. Therefore only the above two rules are taken into account.

The parameter 'boxes per wavelength' is obtained as follows [43] :

$$BPW = \frac{U_{\min}}{f_{\max} \Delta x} \tag{3.5}$$

where, $\Delta x$ is the chord length of a single panel of the aerodynamic surface at a strip.

Panel discretization of the fin surface is shown in Figure 20 together with the 'boxes per wavelength' criterion. For the model obtained, the criterion is satisfied. The number is above 15 for all chord strips.
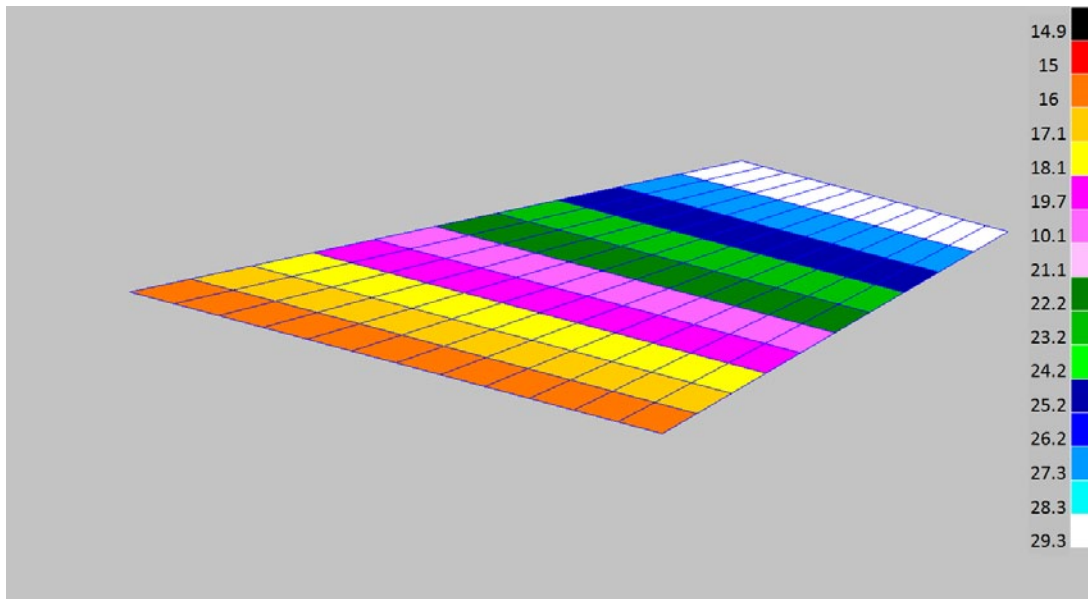
*Figure 20 Aerodynamic Mesh – Boxes per Wavelength*

Panel discretization of the fin surface is shown in Figure 21 together with the 'aspect ratio' criterion. For the model obtained, the criterion is satisfied. The number is below 3 for all panels.
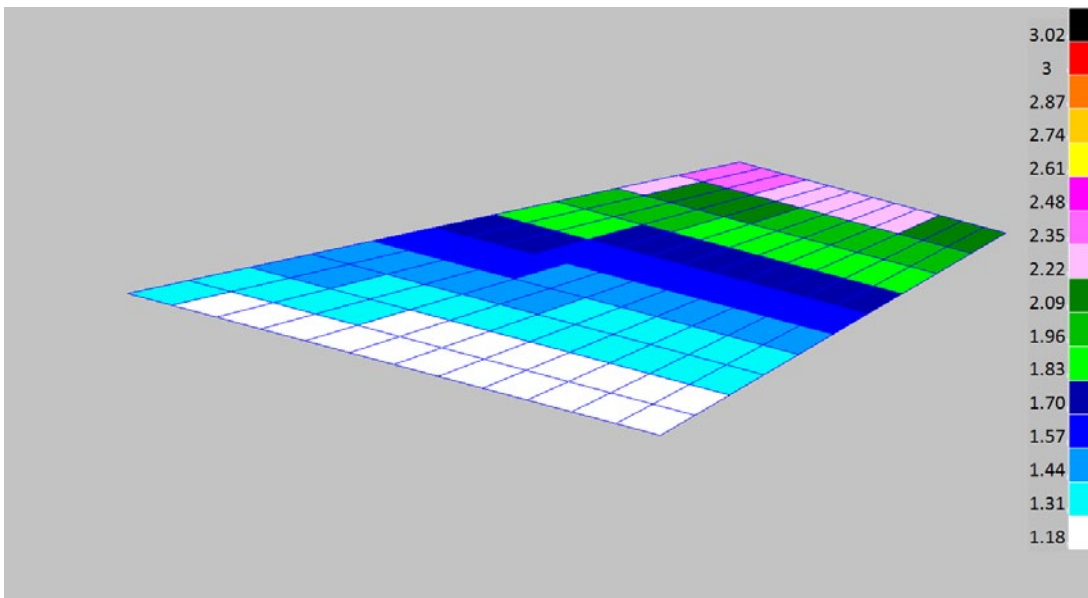


*Figure 21 Aerodynamic Mesh – Aspect Ratio*

The flight envelope of the missile control fin is given in Table 3. According to the given flight envelope, in order to make sure that no flutter condition occurs in operation, flutter analyses should be performed in different Mach numbers and altitudes. Therefore it is needed to obtain the unsteady aerodynamic forces at different Mach numbers. In this section, an analysis envelope that covers the flight envelope is derived. The analysis envelope is bounded by the flight velocity, the altitude, and the reduced frequency limits. This envelope is used for GAF Database generation. This database is also used for frequency domain and time domain analyses carried out in MATLAB.

Derivation of the analysis envelope is summarized as follows:

- The minimum and maximum air speeds that are expected in the flight envelope are calculated. These are the values $U_{min}$ and $U_{max}$.
- The minimum and maximum structural natural frequencies that are used in the analysis are specified. These are the values $f_{min}$ and $f_{max}$.
- The reduced frequency interval at which the oscillatory aerodynamic forces are obtained is calculated from knowledge of $U_{min}$, $U_{max}$, $f_{min}$ and $f_{max}$:

$$k_{min} = \frac{f_{min}b}{U_{max}} \tag{3.6}$$

$$k_{max} = \frac{f_{max}b}{U_{min}} \tag{3.7}$$

- A generalized aerodynamic force database for the calculated reduced frequency range, at a satisfactory number of Mach numbers in the flight envelope, is generated.

Table 7 summarizes the values obtained in GAF Database generation for the missile control fin flight envelope.

*Table 7 Summary of GAF Database Generation*

| | |
|---|---|
| $U_{min}$ | 150 m/s |
| $U_{max}$ | 240 m/s |
| $f_{min}$ | 0 Hz |
| $f_{max}$ | 1000 Hz |
| $k_{min}$ | 0.001 |
| $k_{max}$ | 3.3 |
| Mach | 0.5 , 0.6 , 0.7 , 0.8 |
| # of Reduced Frequencies | 15 |

Figure 22 shows the DMAP code inserted to the Executive Control Deck to output the GAF Matrices at different reduced frequencies and at a single Mach number to a text file. This text file is read by MATLAB with an interfacing code developed. The GAF matrices are output in the k-set.

```
$ Direct Text Input for Executive Control
COMPILE FLUTTER $
ALTER 31 $
OUTPUT4 GPIK,GDKI,GDAK,,//0/21 ///30 $ OUTPUT4 QKK,,,,//0/21 ///30 $
FILE QKKL=APPEND
ALTER 'delete /qhh,qhj,qkh'
MATGEN ,/I240/1/240 $
amp      ajj0,wskjf,d1jk,d2jk,I240,I240,I240,d1je,d2je,
            mklist,lajjt,uajjt/
            QKK,obsi,obsii/240/noue/gustaero/machno/kbar $
APPEND QKK,/QKKL/2
ALTER 'ENDIF $ NOQHHL>0'
OUTPUT4 QKKL,,,,//0/21 ///30 $
```

*Figure 22 DMAP Code in Executive Control Deck for GAF Extraction*

### 3.2.2 Rational Function Approximation to Unsteady Aerodynamics

In this section, results obtained by applying the RFA formulation given in Section 2.2.1.4 to the GAF Database at Mach 0.6 are presented. As the number of fits is $n_m{}^2 x n_k$, only a sample of fits is presented. In Figure 23 and Figure 24, an element of $\overline{Q}_{mm}$ and $Q_{mm}$ are compared for each reduced frequency at which $Q_{mm}$ is obtained.
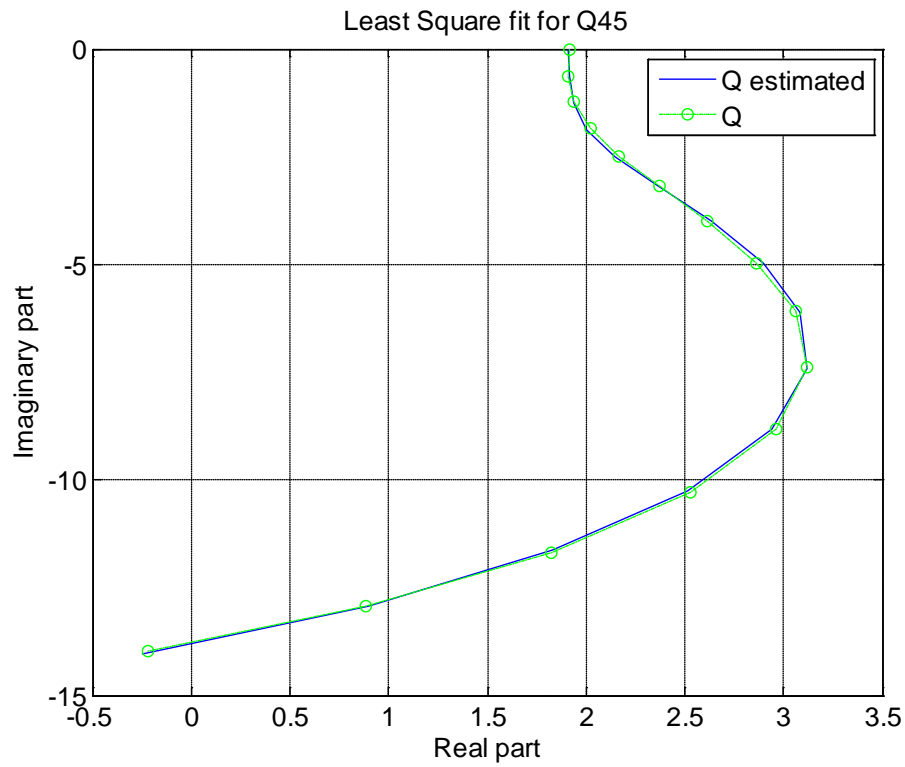


*Figure 23 RFA Fit for* $Q_{45}$
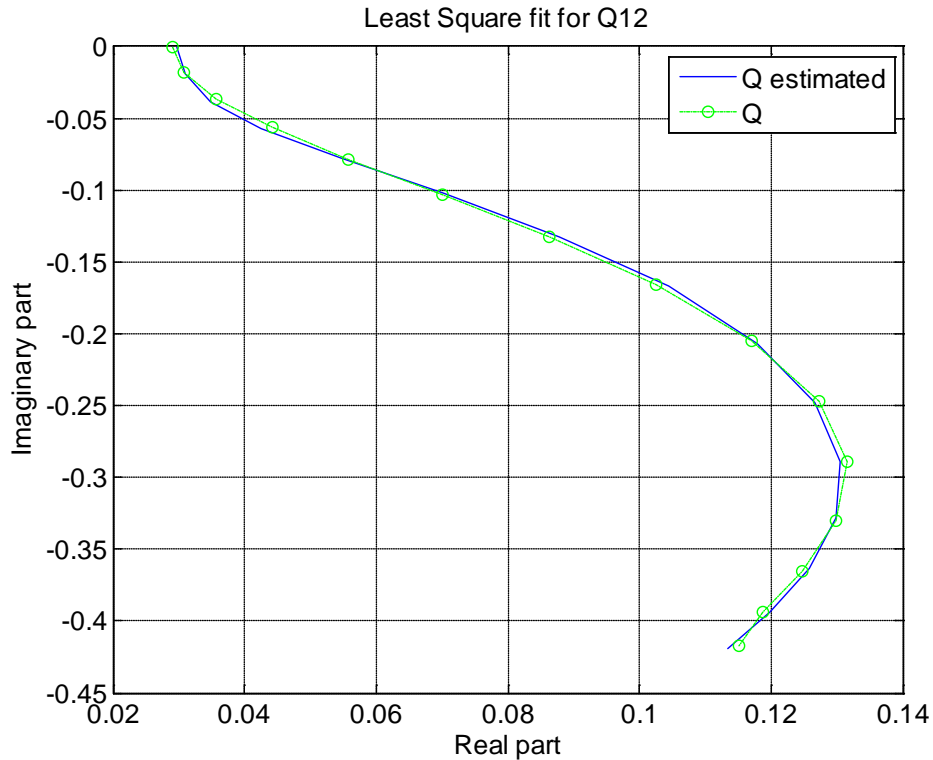
*Figure 24 RFA Fit for* $Q_{12}$

### 3.3 Flutter Solution Methods and Flutter Margins

There are various flutter solution techniques for aeroelastic systems in literature. The most frequently used methods for linear systems that can be represented in frequency domain are the k-method and the p-k method. Commercial programs like ZAERO® and MSC® NASTRAN also include the g method and the k-e method respectively. In this thesis, flutter calculations are carried out in both MSC® NASTRAN and MATLAB®.

P-K method is selected as a frequency domain solution method because of its ease of use, and accuracy. Analysis carried out in MSC® NASTRAN involves only the p-k method solution. On the other hand, in MATLAB®, by utilizing state space system matrix obtained in Eqn. (2.63), root locus solutions are obtained. To calculate the flutter margin, a time domain simulation which has a non-zero initial condition, is also performed in MATLAB®. The results obtained in both software platforms are listed, compared and verified in following sections.

#### 3.3.1 P-k Method Solution

##### 3.3.1.1 Approach to P-k Method

Main steps followed during a p-k method flutter analysis are summarized below:

- The altitudes at which the flutter analysis should be carried out are specified.
- The speed range at which the flutter speed will be searched for is specified. The speed range should lie within ($U_{min}^{analysis}$, $U_{max}^{analysis}$) where:

41

$$U_{min}^{analysis} = \frac{f_{min}b}{k_{max}} \tag{3.8}$$

$$U_{max}^{analysis} = \frac{f_{max}b}{k_{min}} \tag{3.9}$$

- A Mach number ($M_i^{analysis}$) and altitude($h_i^{analysis}$) pair is selected from the flight envelope, and *each aeroelastic mode* is analyzed for flutter.
- If a speed at which the system goes unstable is found for an aeroelastic mode, the equivalent airspeed ($U_{eq}$) at that altitude is calculated.

$$U_{eq} = U_{unstable}\sqrt{\rho/\rho_{sealevel}} \tag{3.10}$$

where, $\rho$ is the air density at $h_i^{analysis}$.

- From the Mach – Air speed – Altitude curves shown in Figure 25, the Mach number ($M^{eq}$) corresponding to the equivalent airspeed ($U_{eq}$) and analysis altitude $h_i^{analysis}$ is found. Note that Mach – Airspeed - Altitude curves are valid for a specific region of latitude and longitude.
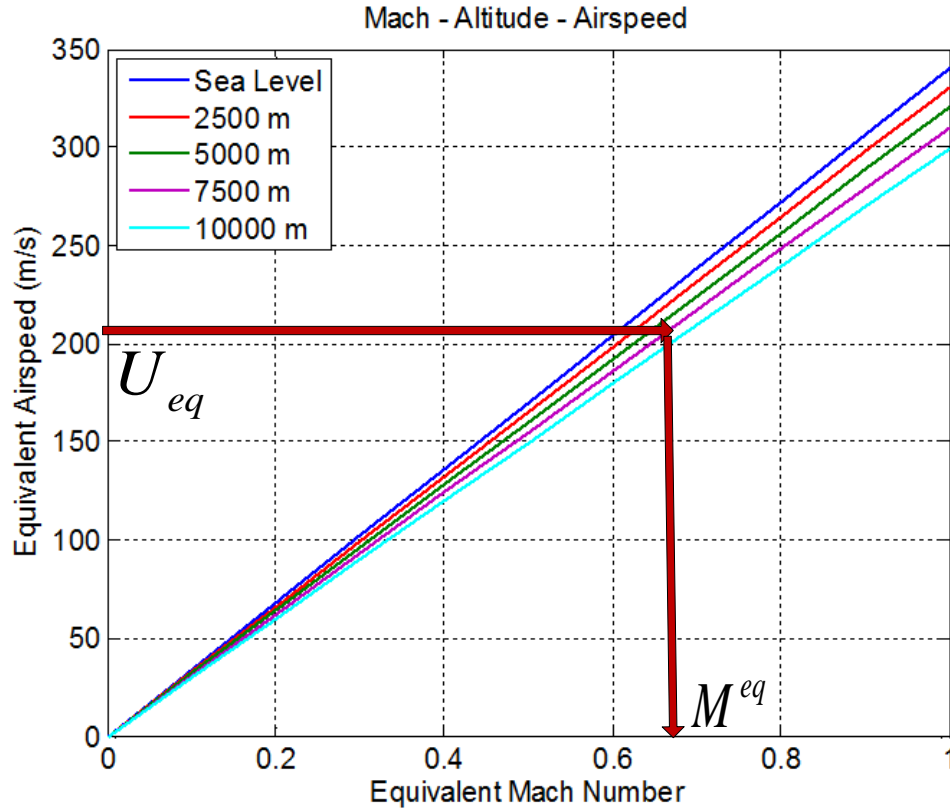


*Figure 25 Mach – Airspeed – Altitude Curves*

The Mach number obtained should lead to the following conclusions:

- If the Mach number ($M^{eq}$) obtained is equal to $M_i^{analysis}$, a match point is obtained at the specified $M_i^{analysis}$ and $h_i^{analysis}$. No match point should exist in the flight envelope for safe operation of any aircraft.

42

- If the Mach number obtained ($M^{eq}$) is greater than $M_i^{analysis}$, then $M_i^{analysis}$ is a safe flight condition at the specified altitude. Then another search at a different Mach number – Altitude pair could be started.

- If the Mach number obtained ($M^{eq}$) is smaller than $M_i^{analysis}$, then there exists a match point below $M_i^{analysis}$ at $h_i^{analysis}$. An analysis with a smaller Mach number at $h_i^{analysis}$ should be carried out so that the promising match point could be found.

### 3.3.1.2 Equation for P-k Method

A flutter analysis seeks a solution to the following aeroelastic equation in modal coordinates:

$$\left( \omega^2 \mathbf{M}_{ss} + i\omega \mathbf{C}_{ss} + (1 + ig) \mathbf{K}_{ss} - q\mathbf{Q}_{ss}(M,k) \right) \zeta_s = 0 \tag{3.11}$$

where $g$ is an artificial coefficient and $\omega$ is the oscillation frequency of the structure. In Eqn. (3.11), aerodynamic forces and $\zeta_s$ is harmonic in nature. Eqn. (3.11) is solved for $g$ by an engineering approach, to find the flutter margin. The idea is to apply a range of harmonic forcing to the structure through $q\mathbf{Q}_{ss}(M,k)$, and analyze the stability of oscillations. The equation is solved for the parameter $g$. If $g$ is equal to zero, then the oscillations are sustained without attenuation, and the aeroelastic system becomes marginally stable. This is called the onset of flutter.

The p-k method directly assumes $g = 0$ and reformulates Eqn. (3.11), utilizing the oscillatory GAF matrices as:

$$\left( p^2 \mathbf{M}_{ss} + p\left( \mathbf{C}_{ss} - \frac{\rho b U}{2k} \mathbf{Q}_{ss}^{imag}(M,k) \right) + \left( \mathbf{K}_{ss} - q\mathbf{Q}_{ss}^{real}(M,k) \right) \right) \zeta_s(s) = 0 \tag{3.12}$$

Where, $p = \omega(\gamma + i)$. Note that for complex roots $\gamma = \dfrac{2pb}{U \ln(2)}$ .

In Eqn. (3.12), the imaginary part of the aerodynamic forcing is considered as a damping agent, and the real part of the aerodynamic forcing is considered as a stiffness agent. Eqn. (3.12) is a nonlinear, complex eigenvalue problem. Eqn. (3.12) is solved for $p$ for a range of Mach number – altitude pairs and reduced frequency. If a Mach - altitude pair that gives $\gamma = 0$ is found, then a candidate flutter speed is obtained. A detailed solution procedure for Eqn. (3.12) is given in [45].

### 3.3.1.3    Results of P-k Method

The flight conditions at which the flutter analysis are carried out for the fin are given in Table 8. First, flutter speed is searched at 3 altitudes at Mach 0.6. The GAF database with properties given in Table 7 is used.

*Table 8 Flutter Analysis Conditions*

| | |
|---|---|
| $U_{\text{min}}^{analysis}$ | 180 m/s |
| $U_{\text{max}}^{analysis}$ | 340 m/s |
| $h_i^{analysis}$ | 0 m<br>2500 m<br>5000 m |
| $M^{\,analysis}$ | 0.6 |

The results of the analysis are summarized in Table 9.

*Table 9 Flutter Analysis Results*

| $h_i^{analysis}$ (m) | 0 | 2500 | 5000 |
|---|---|---|---|
| $M^{\,analysis}$ | 0.6 | 0.6 | 0.6 |
| $\rho_i^{analysis}$ (kg/m$^3$) | 1.226 | 1.173 | 0.902 |
| Speed of Sound | 340.3 | 330.6 | 320.5 |
| Flutter Point | Aeroelastic Mode 3 | Aeroelastic Mode 3 | Aeroelastic Mode 3 |
| Flutter Speed (m/s) | 250.81 | 256.28 | 292.57 |
| Flutter Frequency (Hz) | 143.86 | 143.87 | 143.85 |
| $U^{\,eq}$ (m/s) | 250.81 | 250.71 | 250.99 |
| $M^{\,eq}$ | 0.74 | 0.76 | 0.78 |

The flutter speeds found are checked for altitude, and Mach correspondence, according to the steps explained in Section 3.3.1.1 as shown in Figure 26, Figure 27 and Figure 28.
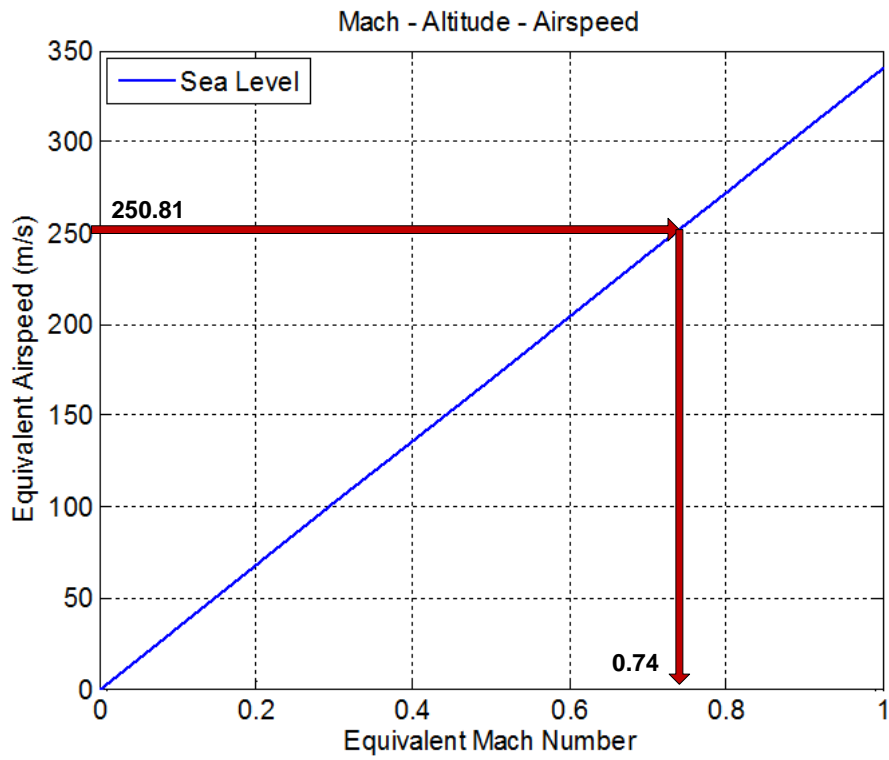
*Figure 26 Mach – Airspeed - Altitude Curve for A1*
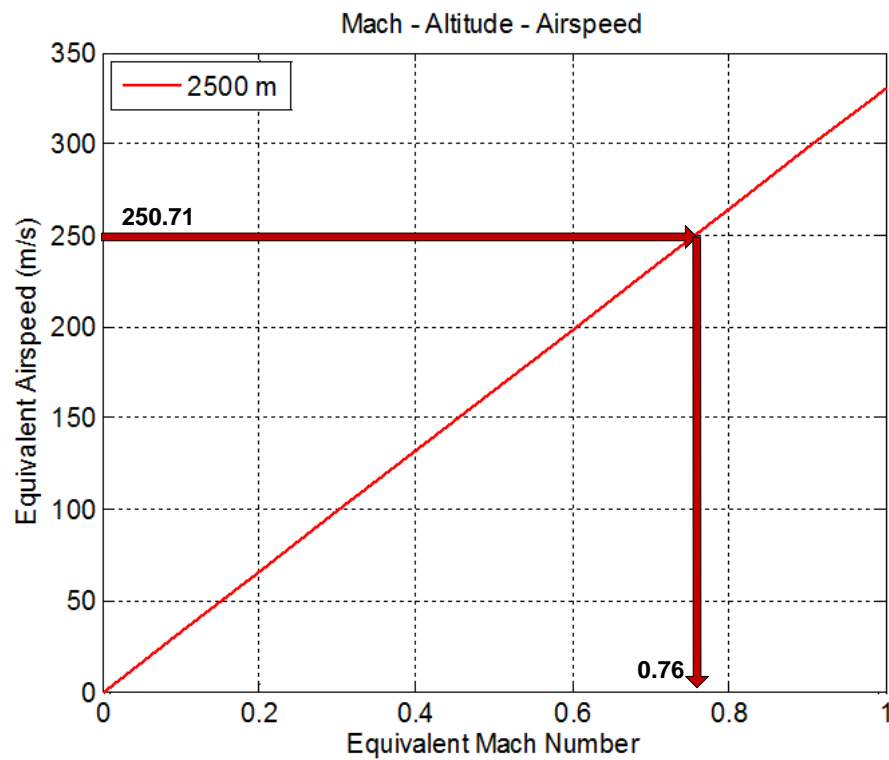


*Figure 27 Mach – Airspeed - Altitude Curve for A2*
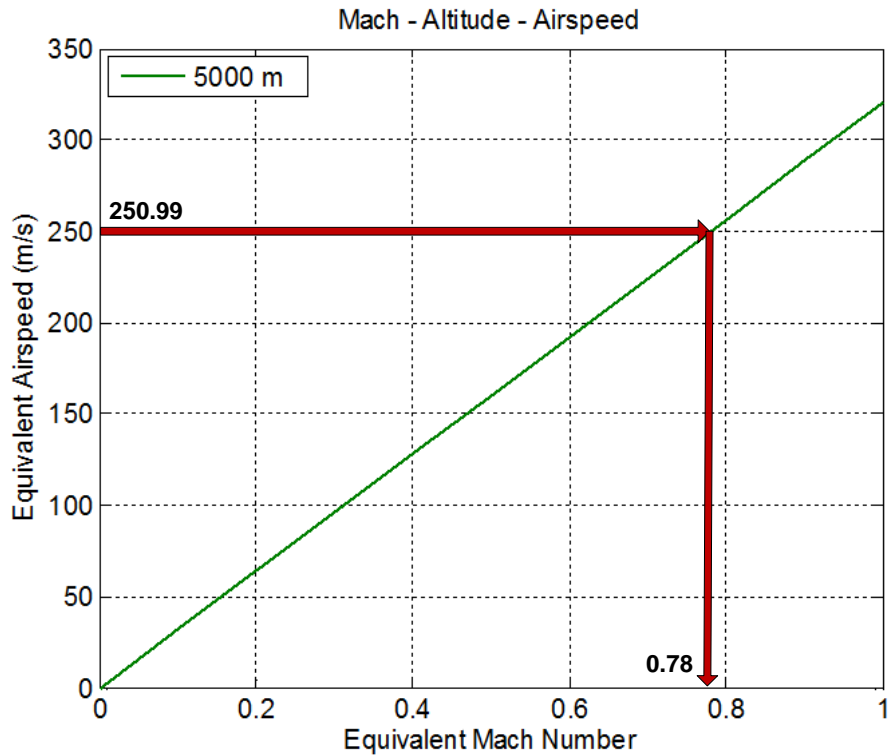
*Figure 28 Mach – Airspeed - Altitude Curve for A3*

As the resulting flutter speeds did not give a matched flutter condition, iterations on Mach number is necessary to find the true flutter margin. This is done by repeating the analysis at Mach 0.75 for the same 3 altitudes. The results are summarized in Table 10.

*Table 10 Flutter Analysis Results (Second Iteration)*

| $h_i^{analysis}$ (m) | 0 | 2500 | 5000 |
|---|---|---|---|
| $M^{analysis}$ | 0.75 | 0.75 | 0.75 |
| $\rho_i^{analysis}$ (kg/m$^3$) | 1.226 | 1.173 | 0.902 |
| Speed of Sound | 340.3 | 330.6 | 320.5 |
| Flutter Point | Aeroelastic Mode 3 | Aeroelastic Mode 3 | Aeroelastic Mode 3 |
| Flutter Speed (m/s) | 251.12 | 256.62 | 292.81 |
| Flutter Frequency (Hz) | 143.55 | 143.57 | 143.57 |
| $U^{eq}$ (m/s) | 251.12 | 251.04 | 251.21 |
| $M^{eq}$ | 0.74 | 0.76 | 0.78 |

When Table 9 and Table 10 are compared, it is observed that the equivalent Mach numbers did not change up to second decimal point. Therefore it is concluded that the flutter speeds given in Table 10 are almost matched. The mode at which flutter occurs is presented in Figure 29.

46
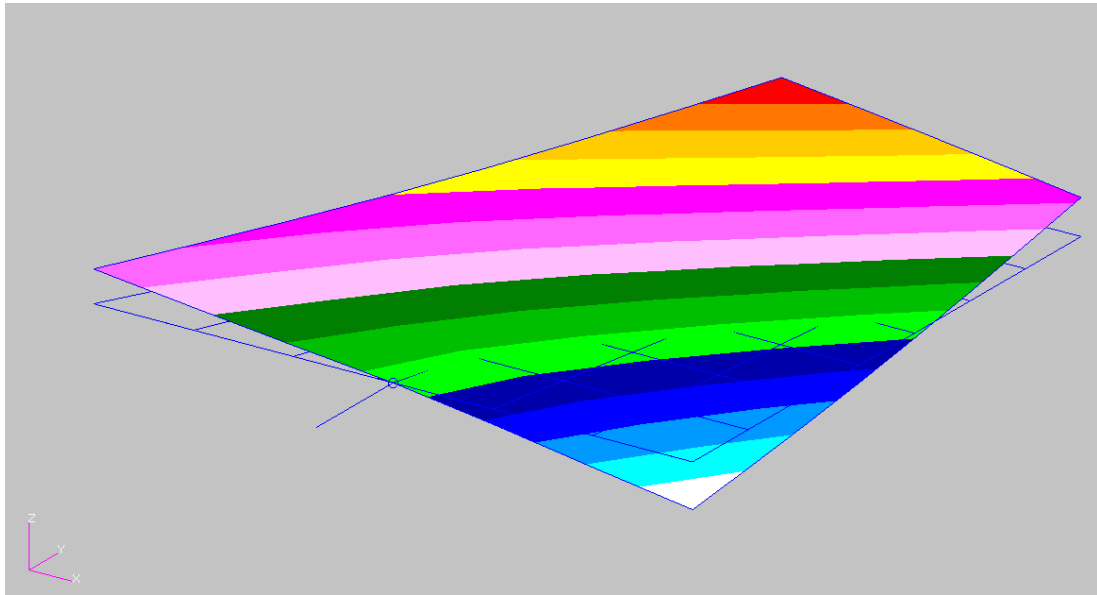
*Figure 29 Flutter Modeshape*

Airspeed vs. damping coefficient and airspeed vs. frequency plots are provided below for sea level flutter analysis.
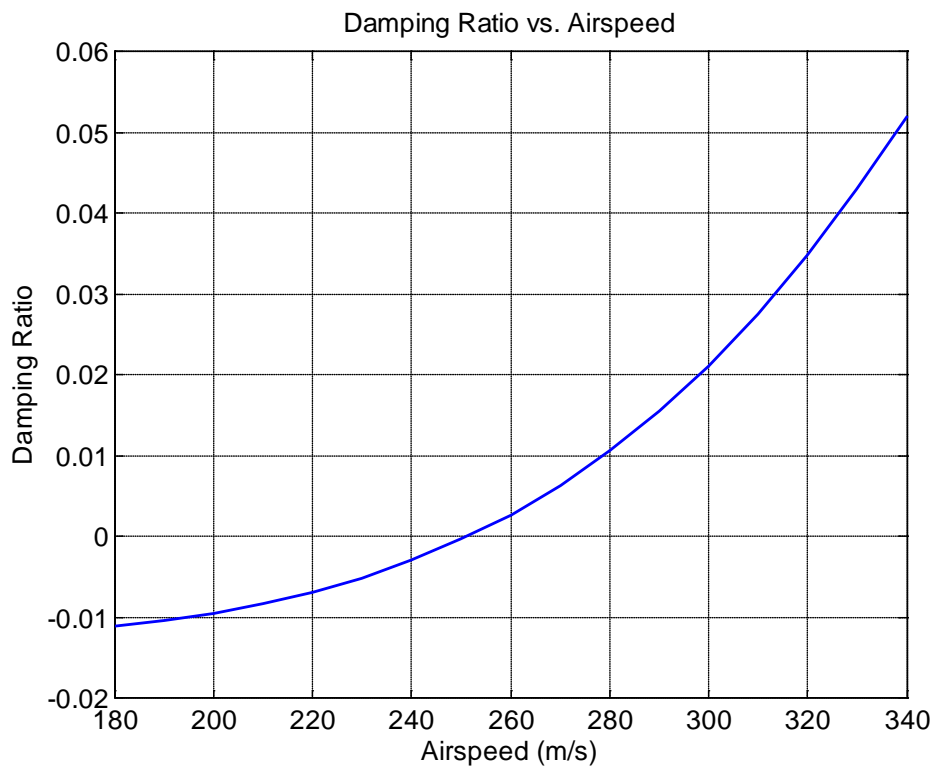


*Figure 30 Damping Ratio of Aeroelastic Mode 2 Calculated with the p-k Method*

The damping ratios and aeroelastic frequencies obtained from MSC NASTRAN analysis output file are shown in Figure 30 and Figure 31 respectively.
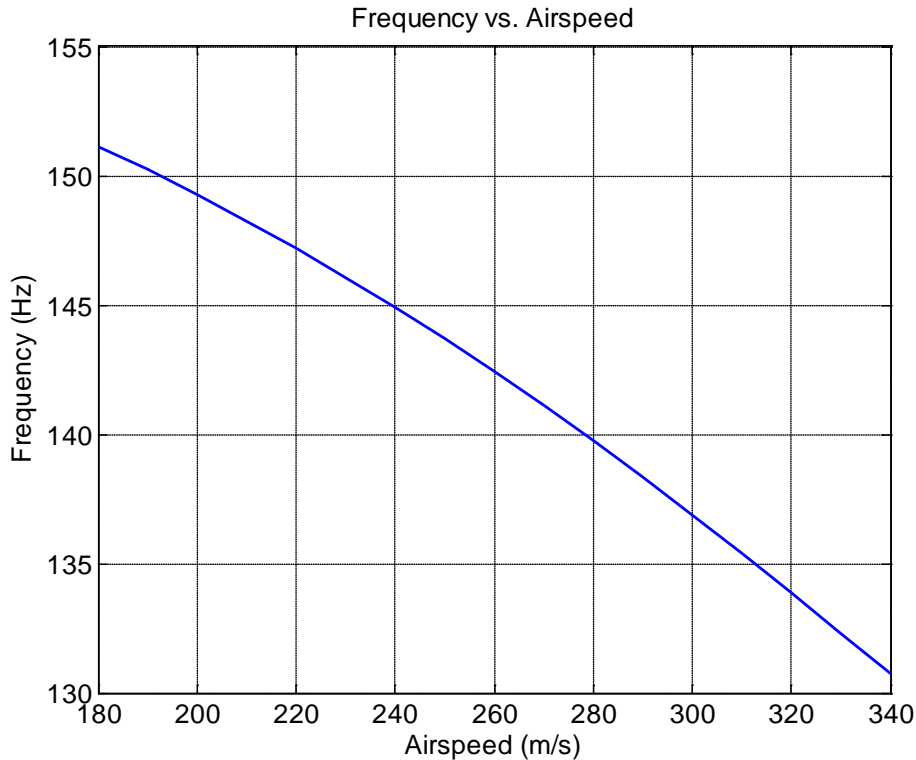
Figure 31 Frequency of Aeroelastic Mode 2 Calculated with the p-k Method

### 3.3.2    Root Locus Solution

In Section 2.4, the aeroelastic system matrix $A_{sys}$ is given. One way of searching for aeroelastic instability is to analyze $A_{sys}$ for stability. The eigenvalues of $A_{sys}$ is equivalent to the poles of the aeroelastic transfer function, and these eigenvalues are tracked in the locus of roots diagram, by gradually increasing the free stream speed in $q$ .

$A_{sys}$ has many eigenvalues, involving information about the dynamics of both the generalized coordinates and the aerodynamic lag states. When searching for flutter, one is interested in the stability of the generalized coordinates. Note that the transfer function for the aerodynamic lag states is given in Eqn. (2.28), and the poles of that transfer function is selected to be on the left hand side of the s-plane, so that the resulting aerodynamic lags do not explicitly bring unstability to the system. Then only the eigenvalues corresponding to the generalized coordinates are plotted on the root locus.

Since $A_{sys}$ is valid for a Mach number, altitude and a range of reduced frequencies, the approach to flutter analysis is similar to the p-k method. If the flutter speed results are non-matched, iterations on $M_i^{analysis}$ are again needed. The root locus analysis for flutter in this thesis is carried out in MATLAB; so that the structural and the aerodynamic matrices obtained from MSC NASTRAN, and the implementation of RFA method could be verified. Therefore, the only aeroelastic system matrix that is subjected to the root locus analysis is constructed by utilizing the GAF Database at Mach 0.75, at which the final flutter analysis was carried out with the p-k method in Section 3.3.1.

The eigenvalues corresponding to the generalized coordinates are obtained by using the MATLAB command 'eig' for $A_{sys}$ at selected free stream speeds which range from 180 m/s 340 m/s, with 10 m/s intervals. Below formulation is used to extract the effective damping ratio and undamped natural

frequency of an aeroelastic mode corresponding to an eigenvalue obtained. System matrix of a damped system gives complex eigenvalues $\lambda$, such that:

$$\lambda_j = -\xi_j \omega_j + i\omega_j \sqrt{1 - \xi_j^2} \qquad (3.13)$$

After each $\lambda_j$ is obtained from eigenvalue analysis, $\xi_j$ and $\omega_j$ are obtained for each aeroelastic mode, where the subscript 'j' denotes an aeroelastic mode. Locus of roots are plotted as the airspeed changes for the second aeroelastic mode, at which the flutter was found to exist with the p-k method, in Figure 32.
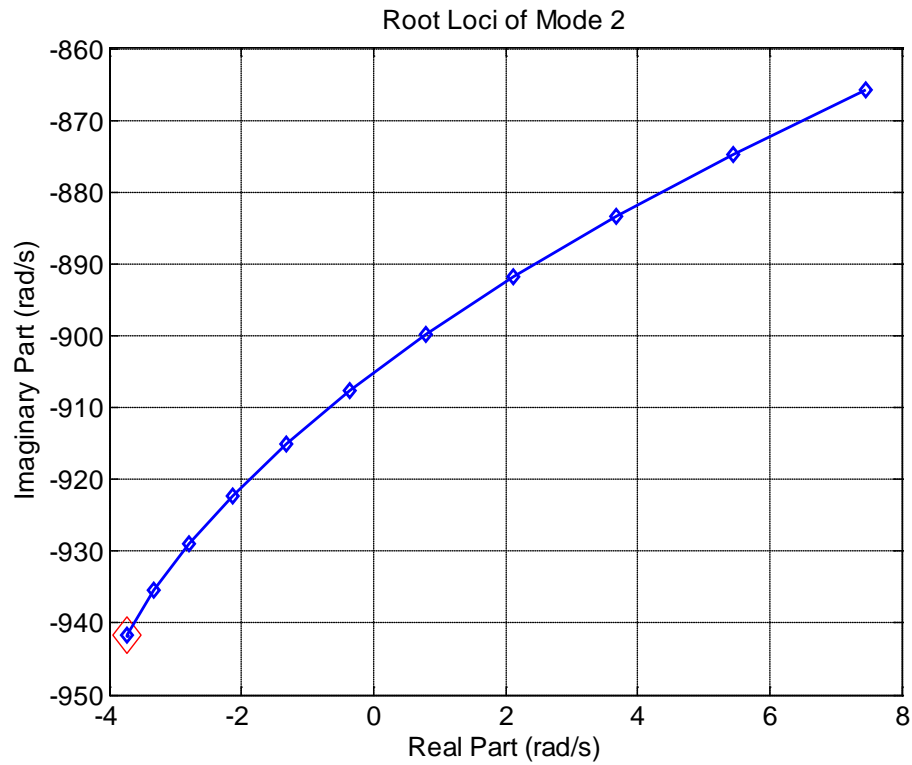


Figure 32 Locus of Aeroelastic Roots for Aeroelastic Mode 2

As the real part of the aeroelastic roots have positive values as the airspeed increases, instability is found in the second aeroelastic mode. The corresponding damping ratio and natural frequency of the second aeroelastic mode as airspeed changes are given in Figure 33 and Figure 34 respectively.
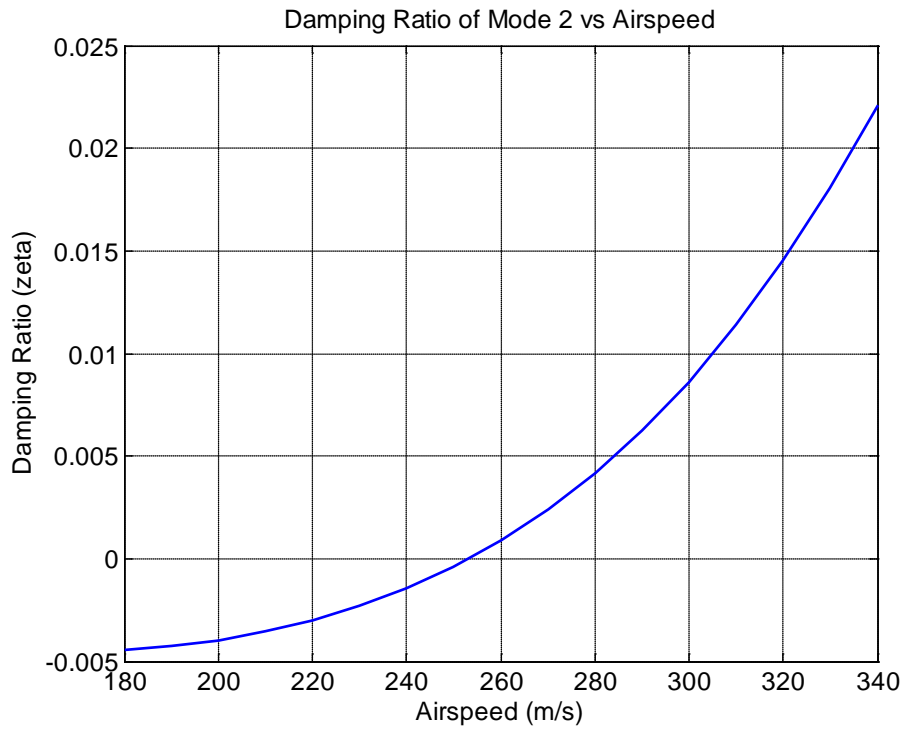
*Figure 33 Damping Ratio of Aeroelastic Mode 2 Calculated with the Root Locus Method*
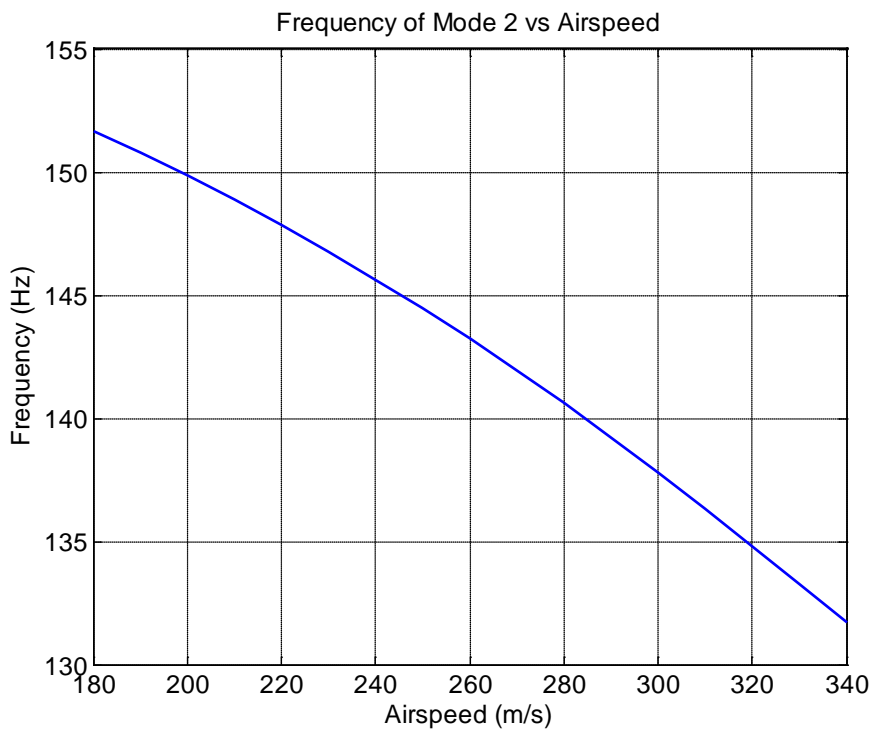


*Figure 34 Natural Frequency of Aeroelastic Mode 2 Calculated with the Root Locus Method*

The flutter speed is found to be at 253.11 m/s, at which the damping ratio of the second aeroelastic mode is zero. The flutter frequency is obtained at 253.11 m/s is 144.1 Hz.

The locus of roots for all aeroelastic modes together is given in Figure 35.
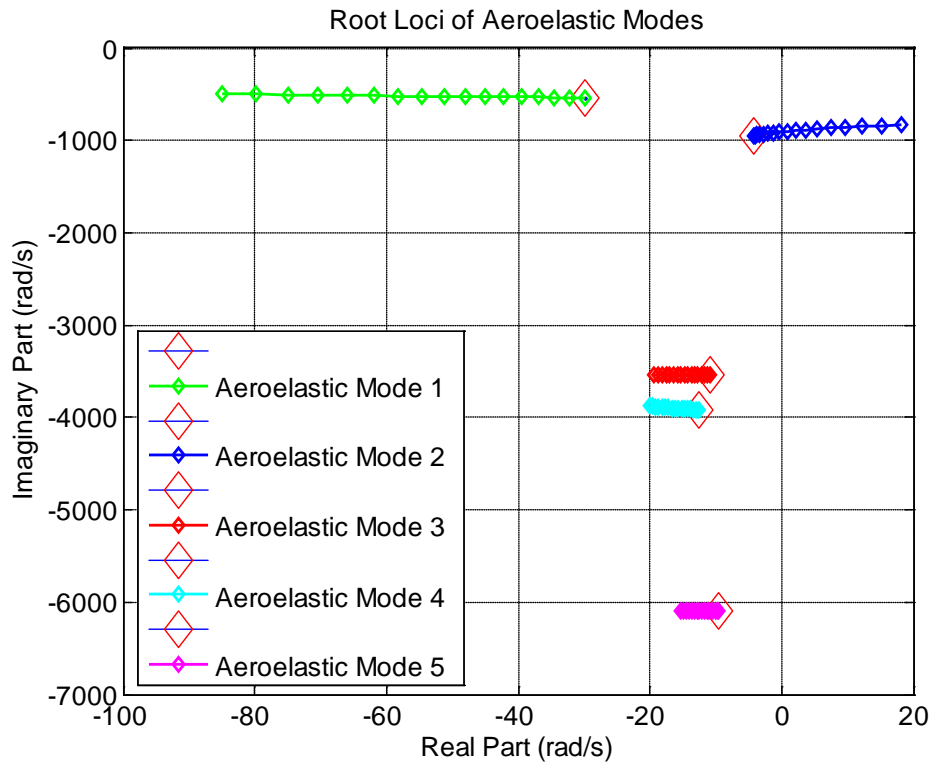
*Figure 35 Locus of Aeroleastic Roots*

As observed from Figure 35, the only aeroelastic mode that has a postive real part is the second mode. This result is equivalent to the one obtained in p-k method analysis. For the modes analyzed, no mechanism for unstability is observed in modes other than the second aeroelastic mode.

### 3.3.3 Time Domain Solution

Time domain solution of flutter is carried out, so that utilizing the aeroelastic system matrix for state space analysis is validated. Again, the aeroelastic system matrix constructed with the GAF Database at Mach 0.75 is used. By assigning a unit initial condition to the generalized coordinate of the second aeroelastic mode, time response of generalized coordinates of the open loop aeroelastic system is simulated with 1 m/s airspeed intervals. Eqn. (3.14) is integrated with a variable step solver (ode45) built in MATLAB, to obtain the time response of generalized coordinates for the quarter of a second.

$$\{\dot{z}(t)\} = \left[ A_{sys} \right] \{z(t)\} \tag{3.14}$$

where the state vector is defined as:

51

$$\{z(t)\} = \begin{Bmatrix} \zeta_s(t) \\ \dot{\zeta}_s(t) \\ \zeta_{s_{a1}}(t) \\ ... \\ \zeta_{s_{aN}}(t) \\ \zeta_{c_{a1}}(t) \\ ... \\ \zeta_{c_{aN}}(t) \end{Bmatrix} \qquad (3.15)$$

The initial condition for $\{z(t)\}$ is given such that all elements of $\{z(0)\}$ is zero except the second element of $\{\zeta_s(0)\}$, which is the initial value of the second aeroelastic generalized coordinate. That initial value is set to unity.

Time responses of the generalized coordinate corresponding to the second aeroelastic mode at selected free stream speeds are presented in Figure 36, Figure 37 and Figure 38.
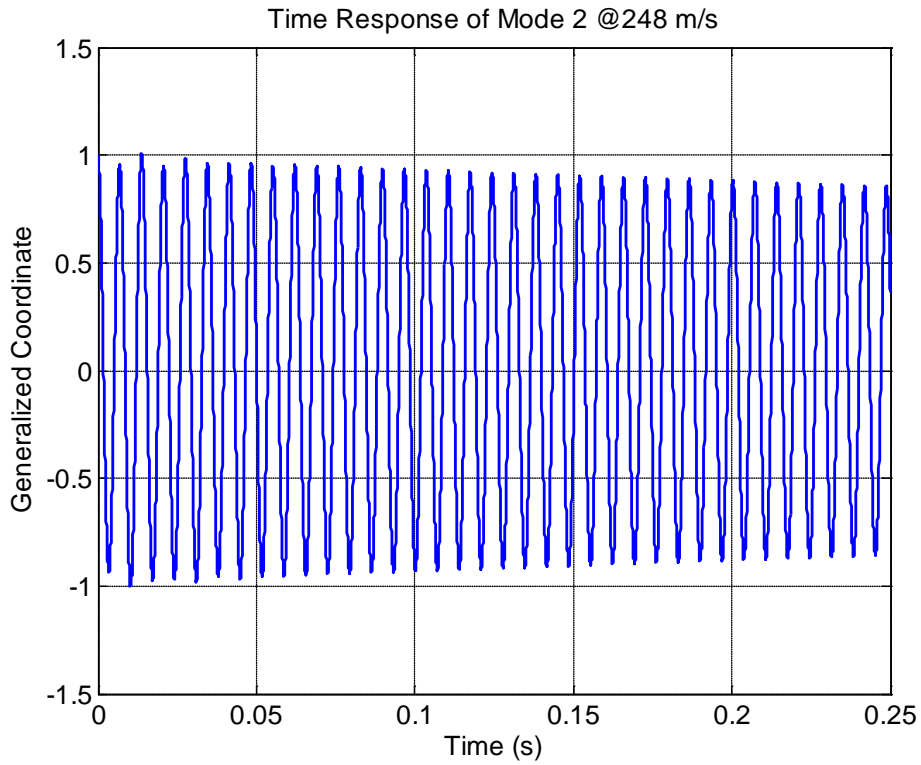


*Figure 36 Time Simulation of Second Aeroelastic Generalized Coordinate at 248 m/s*
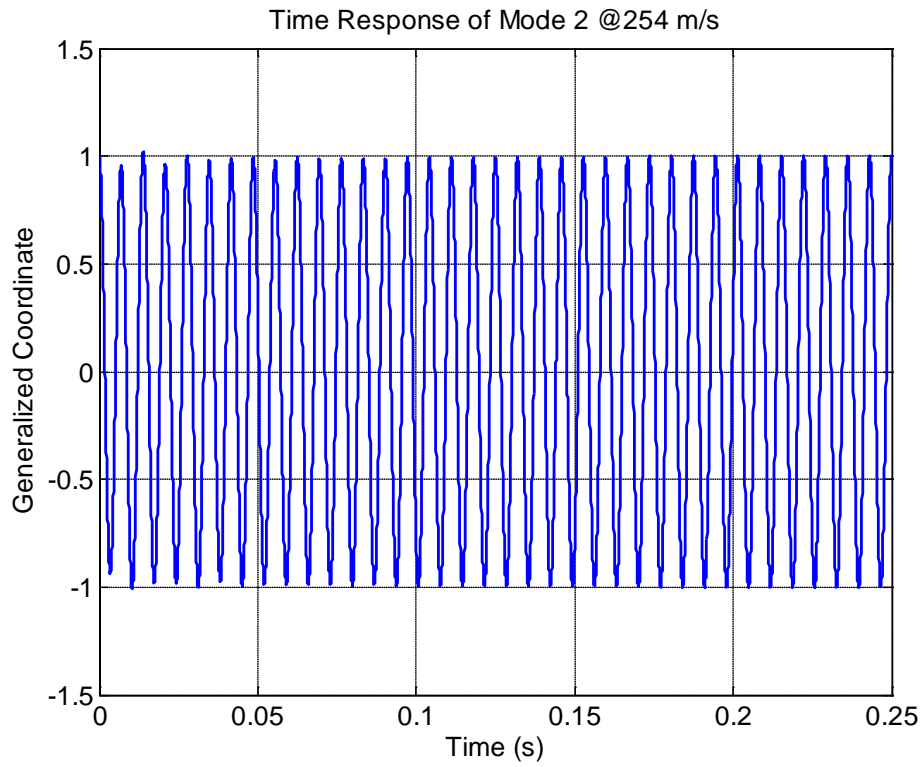
*Figure 37 Time Simulation of Second Aeroelastic Generalized Coordinate at 254 m/s*
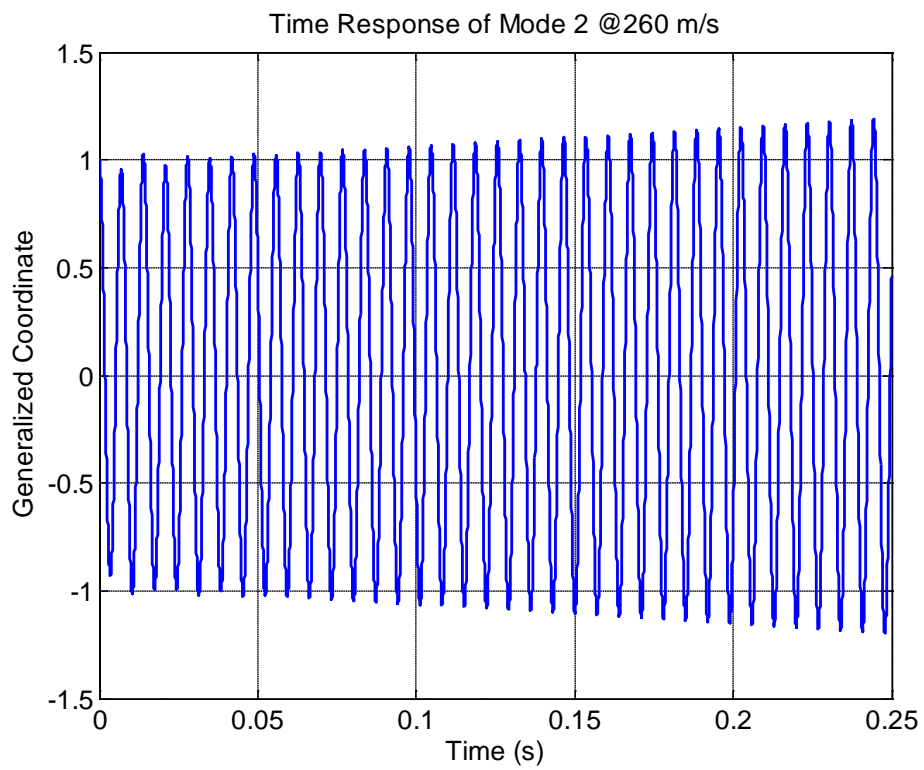


*Figure 38 Time Simulation of Second Aeroelastic Generalized Coordinate at 260 m/s*

According to Figure 36, Figure 37 and Figure 38; the onset of flutter is at 254 m/s.

The step sizes of the time simulation is crucial in reflecting the dynamics of the system. As observed from the root locus diagram in Figure 35, the aeroelastic roots are highly oscillatory and the dynamics is up to approximately 1200 Hz. Therefore the time step used in time simulation is set to be not smaller than 10000 Hz. This value is given as a constraint to the solver. Step sizes used in time simulation at 254 m/s is given in Figure 39.
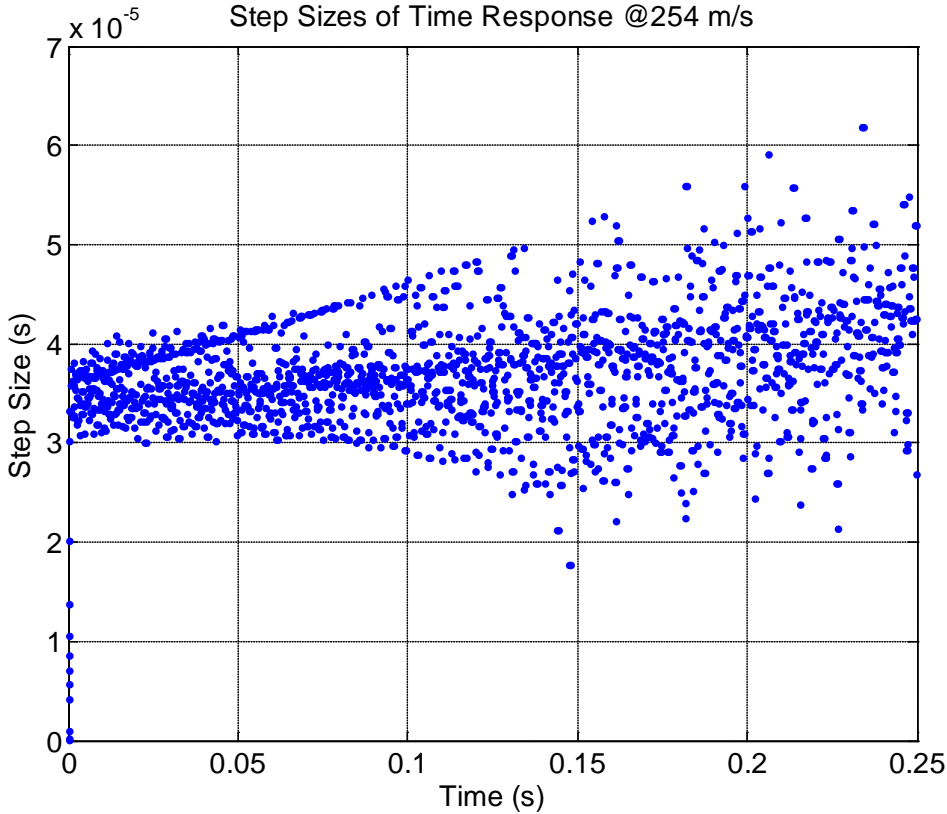


*Figure 39 Variable Step Sizes in Time Simulation*

The step sizes are selected by the 'ode45' solver itself and never got smaller than 10000 Hz.

### 3.3.4    Comparison of Flutter solutions

The flutter speeds obtained by three different methods in Section 3.3.1, Section 3.3.2, and Section 3.3.3 at the sea level are given in Table 11 for comparison.

54

*Table 11 Flutter Speed Comparison*

| | P-k Method (NASTRAN) | Root Locus Method (MATLAB) | Time Domain Solution (MATLAB) |
|---|---|---|---|
| $h_i^{analysis}$ (m) | 0 | 0 | 0 |
| $M^{analysis}$ | 0.75 | 0.75 | 0.75 |
| $\rho_i^{analysis}$ (kg/m$^3$) | 1.226 | 1.226 | 1.226 |
| Speed of Sound | 340.3 | 340.3 | 340.3 |
| Flutter Point | Aeroelastic Mode 3 | Aeroelastic Mode 3 | Aeroelastic Mode 3 |
| Flutter Speed (m/s) | <span style="color:red">251.12</span> | <span style="color:red">253.11</span> | <span style="color:red">254</span> |
| Flutter Frequency (Hz) | 143.55 | 144.1 | - |
| $U^{eq}$ (m/s) | 251.12 | 253.11 | 254 |
| $M^{eq}$ | 0.74 | 0.74 | 0.74 |

According to Table 11, there are differences in the flutter results obtained with different methods. These differences are the consequences of several phenomena:

- MSC NASTRAN uses linear interpolation methods while solving the flutter equation by the p-k method [34]. Therefore when solving for airspeeds other than the ones defined in the GAF Database, it uses interpolation for calculating aerodynamic forcing at discrete reduced frequencies. On the other hand, RFA methods are used in constructing the aeroelastic system matrix, whose stability is analyzed with root locus and time domain methods. Therefore when solving for intermediate airspeed values, a different methodology is being employed, because the analysis at discrete reduced frequencies are now a function of the RFA method used.

- The least square fits performed by Roger's method is always questionable when experimental information about the lag states is unavailable. The lag roots are chosen so that the overall least square error is minimized but the optimization process is unconstrained. No constraint is applied to exactly match the flutter speed or steady state aerodynamic forcing, therefore the resulting fits may deviate from the true aerodynamic forcing at discrete reduced frequencies of the GAF Database. There are various methods of constrained optimization in literature for RFA methods [24], which are not applied in this thesis.

The flutter results presented in Table 11, are considered to be almost identical. Therefore it is concluded that the RFA fitting process and the aeroelastic system matrix construction is valid.

# CHAPTER 4

## SERVO-ACTUATOR MODELING

In this chapter, a DC Motor and a transmission unit is selected for the smooth operation of the servo-actuation system, in compliance with the requirements of the control fin given in Section 1.2 in Table 2 and Table 3. The parameters of the selected DC motor and the transmission unit are inserted into the open loop actuator transfer function (2.41) for the PD controller synthesis. The PD controller synthesis is then carried out using the Root Locus Method. The PD controller design is carried out by neglecting the elastic structural and unsteady aerodynamic effects on the fin, as if the fin is rigid and the aerodynamics is steady. This is the traditional approach to controller design for missile fin actuation systems. The drawbacks of this approach are discussed in Section 5.2. Dynamics of the open loop and closed loop system are presented in both frequency and time domains.

## 4.1 Selection of DC Motor and Transmission Unit

The DC motor and the Transmission Unit together are called as the actuator. The selection of the actuator depends on the requirements of the servo-actuation system. In this section, the parameters driving the selection of the actuator are explained. The two main performance requirements that lead to a selection are the required torque and the required angular velocity at the fin. The required torque estimate for no stall is 6 N.m and the required velocity at that load torque is specified as 300 deg/s.

### 4.1.1 Specification of Maximum Required Torque

The maximum torque that an actuator can provide to the fin depends on both the DC motor and the transmission unit. The total maximum load torque on the actuator comes from the aerodynamic moment and the acceleration torque due to the inertia of the fin. The stall torque of the actuator should be higher than the resultant of the two.

$$T_{stall\,@\,fin} \geq T_{aero\,@\,fin}^{\max} + T_{inertial\,@\,fin}^{\max} \tag{4.1}$$

$T_{inertial\,@\,fin}$ is the total inertial moment at the fin due to the inertia of the fin. Eqn. (4.1) can also be expressed at the motor output shaft as:

$$T_{stall\,@\,motor} \geq T_{aero\,@\,motor}^{\max} + T_{inertial\,@\,motor}^{\max} \tag{4.2}$$

where,

$$T_{inertial\,@\,motor}^{\max} = \left( J_{motor} + J_{tr\,@\,motor} + J_{fin\,@\,motor} \right)\alpha_{motor}^{\max} \tag{4.3}$$

Recall from Section 2.4 that;

$$T_{hinge\,@\,fin}(t) = -\mathbf{M}_{cs}\ddot{\zeta}_s(t) + q\mathbf{Q}_{cs}(M,k)\zeta_s(t) - \mathbf{M}_{cc}\ddot{\zeta}_c(t) + q\mathbf{Q}_{cc}(M,k)\zeta_c(t) \tag{4.4}$$

Note that the above equation is expressed for a Mach number and a reduced frequency. Parts of Eqn. (4.4) can be eliminated so that the total load torque is expressed by only the rigid inertial moment and

steady aerodynamic moment. $\zeta_s(t)$ and $\ddot{\zeta}_s(t)$ is set to zero, so that only the rigid inertial moment and the aerodynamics of the rigid fin remains:

$$T_{hinge\,@\,fin}^{rigid}(t) = -\mathbf{M}_{cc}\ddot{\zeta}_c(t) + q\mathbf{Q}_{cc}(M,k)\zeta_c(t) \tag{4.5}$$

The aerodynamics becomes steady when the reduced frequency is zero. The GAF Matrix element $\mathbf{Q}_{cc}(M,k)$ becomes non-oscillatory at zero reduced frequency; therefore it should assume a real value. The smallest reduced frequency in the GAF Database generated is 0.001, which resembles to the steady aerodynamics [11]. $\mathbf{Q}_{cc}(M,k)$ at $k = 0.001$ has a negligible unsteady effect and a negligible imaginary component. Therefore the real part of $\mathbf{Q}_{cc}(M,0.001)$ is taken as the steady aerodynamic coefficient [23]. At Mach 0.6,

$$T_{hinge\,@\,fin}^{rigid,steady}(t) = -\mathbf{M}_{cc}\ddot{\zeta}_c(t) + q\mathbf{Q}_{cc}^{real}(0.6,0.001)\zeta_c(t) \tag{4.6}$$

Note that $\zeta_c(t)$ is the commanded fin position in radians. The maximum angular position that the fin will have is 15°. Therefore Eqn. (4.1) is expressed as:

$$T_{stall\,@\,fin} \geq \left| -\mathbf{M}_{cc}\ddot{\zeta}_c^{max} \right| + \left| q\mathbf{Q}_{cc}^{real}(0.6,0.001)\zeta_c^{max} \right| \tag{4.7}$$

Note that when the fin angular position is at $\zeta_c^{max} = 15$, if it tries to move to $\zeta_c = 0$ with full throttle giving a negative $\ddot{\zeta}_c^{max}$, it would face the maximum resistance torque, given that $\mathbf{Q}_{cc}^{real}(0.6,0.001)$ is positive. Therefore absolute values of the contributors are taken so that the worst case torque is overcome.

All parameters except $\ddot{\zeta}_c^{max}$ is already obtained up to this point. $\ddot{\zeta}_c^{max}$ is derived from the settling time requirement given in Table 2. The fin is expected to settle to $\zeta_c = 15°$ from rest in 50 ms without overshoot. At the moment before the DC Motor and the transmission unit is selected, it is not possible to have an exact value for $\ddot{\zeta}_c^{max}$. It is a common practice to assume a profile that would give the maximal acceleration expected for the application being modeled [46]. Although usually hand drawn profiles are assumed for standard industrial applications, a different methodology is followed here. In order to obtain $\ddot{\zeta}_c^{max}$ estimate for this application, the servo-actuator closed loop transfer function is assumed to respond to the angular position commands similar to a second order system which has the desired response time characteristics, and realistic dynamic limits [47]. The dynamic limits are introduced so as to account for the effect of power source limits. The resulting nonlinear second order dynamic system is tuned so that it meets the 50 ms settling time requirement with a reasonable maximum acceleration. The transfer function of a linear second order system is defined as:

$$\frac{Y(s)}{R(s)} = \frac{\omega_n^2}{s^2 + 2\xi\omega_n + \omega_n^2} \tag{4.8}$$

where,

$Y(s)$: Input

$R(s)$: Output

$\omega_n$ : Undamped Natural Frequency

$\xi$ : Damping Ratio

In order to obtain an estimate for $\ddot{\zeta}_c^{max}$, a nonlinear second order system model is assumed, involving a dynamic acceleration limit which also limits the angular velocity of the system to a

maximum of 500 °/s. The angular velocity limit assumed for the system is higher than the specification 300 °/s, so that the resulting 'estimate' transfer function behaves linear in a wider range of angular position commands and gives a more conservative maximum acceleration value. The MATLAB Simulink implementation of the nonlinear second order system is given in Figure 40[43].



*Figure 40 Second Order System with Position and Acceleration Limit Nonlinearities*

The dynamic behavior of a second order system is defined by its damping ratio and undamped natural frequency. If the system had no dynamic limits, these parameters could be defined for a specific settling time requirement as[48]:

$$\omega_n \Box \frac{4}{\xi t_s} \tag{4.9}$$

where the settling time is defined for the response to be within 2% of the reference, and the damping ratio is lower than 0.9. As the specified transfer function is critically damped and also the original system has power source limits, one should select a larger undamped natural frequency to meet the time response requirement. The undamped natural frequency is increased up to 157 rad/s to obtain a satisfactory time response. Angular position responses of the linear and the nonlinear system with $\omega_n = 157$ rad/s are compared in Figure 41.



*Figure 41 Angular Position Responses of Linear and Nonlinear 2$^{nd}$ order Systems*

59

The angular velocity and angular acceleration responses of the nonlinear second order system with 157 rad/s natural frequency are shown in Figure 42 and Figure 43 respectively.
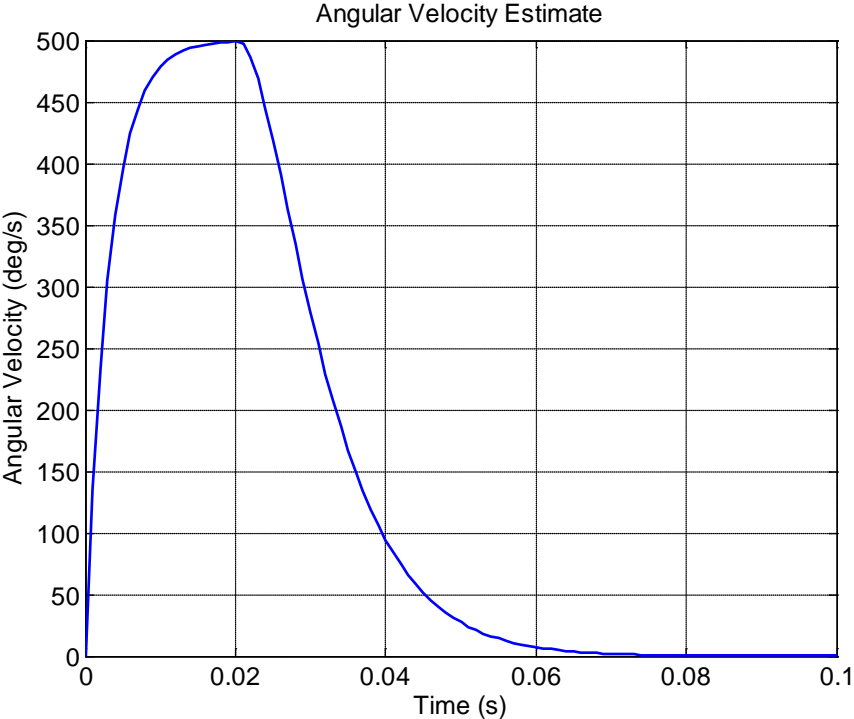


*Figure 42 Angular Velocity of the System with Position and Acceleration Limit Nonlinearities*
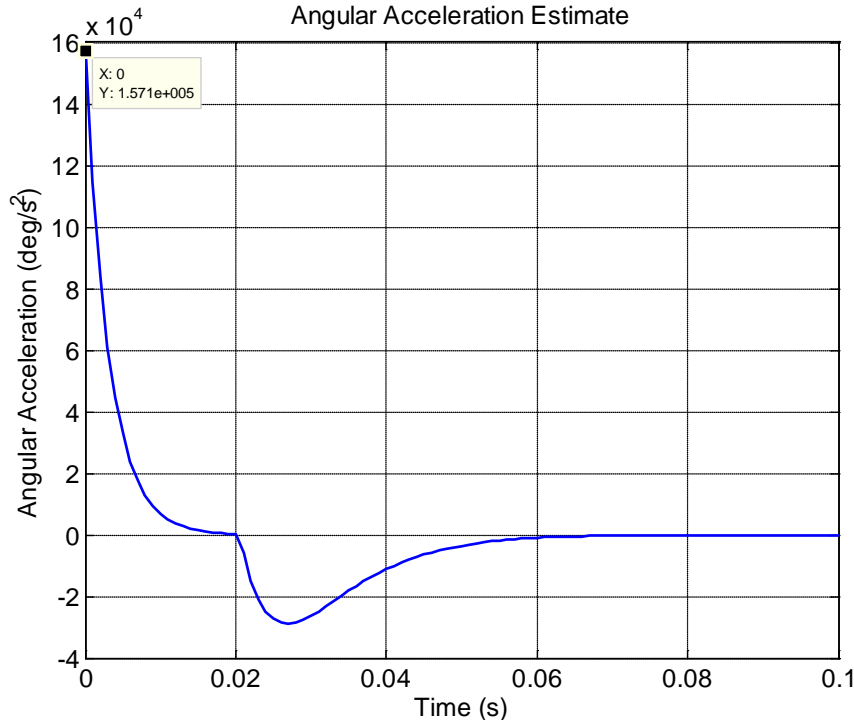


*Figure 43 Angular Acceleration of the System with Position and Acceleration Limit Nonlinearities*

From Figure 43, it is seen that the maximum acceleration attained is 157100 °/s². This acceleration is multiplied with the total inertia at the fin shaft, where the acceleration is actually observed. Then the required maximum torque estimate is obtained as

$$T_{stall \, @ \, fin} \geq \frac{157100 \times \pi}{180} J_{fin} + \left| q Q_{cc}^{real}(0.6, 0.001) \zeta_c^{max} \right| \qquad (4.10)$$

where the values are obtained as:

$$T_{stall \, @ \, fin} \geq \frac{157100 \times \pi}{180} 2.958 \times 10^{-4} + \frac{1}{2} \rho_{max} U_{max}^2 \left( 5.825 \times 10^{-4} \right) \frac{15 \times \pi}{180} \qquad (4.11)$$

$$T_{stall \, @ \, fin} \geq 4.74 \text{ N.m} \qquad (4.12)$$

where $\rho_{max}$ is the sea level air density and $U_{max}$ is the sea level airspeed at Mach 0.6. A factor of safety is generally taken for uncertainties and model fidelity to calculate $T_{stall \, @ \, fin}$. Therefore $T_{stall \, @ \, fin}$ is multiplied with 1.25 for conservatism and taken as 6 N.m.

After the required torque is obtained, the DC motor and the transmission unit are to be selected. In standard industrial applications, the common practice is to select a transmission unit that is capable of producing the necessary amount of torque and angular velocity first. This is because the maximum input angular velocities of transmission units are limited due to lifecycle concerns. The input angular velocities are commonly much lower than a DC motor can produce; therefore the transmission unit becomes the bottleneck. Therefore the DC motor which produces the necessary input torque can be selected after the transmission unit is specified. However, in missile applications, as the missile is a disposable item, lifecycle is not a concern. Therefore the transmission unit can be used at much higher angular velocities than the recommended values specified in catalogs. On the other hand, the size constraints on the actuator unit are demanding in missile applications. A missile is required to be light and compact as possible for any given mission concept, to reduce the costs and improve the dynamic performance. Therefore, strict size constraints are set up on all missile subsystems, including the control actuation system. The DC motor and transmission unit as a whole is required to be smaller than 28 mm in diameter, as given in Table 2 Requirements and Constraints of the Missile Control Fin. In this case, the DC motor is selected according to the diameter constraint. DC Motor Specifications are given in Table 12.

*Table 12 DC Motor Specifications*

| Faulhaber 2642 024CR | | |
|---|---|---|
| Diameter | 26 | mm |
| Length | 42 | mm |
| Voltage | 24 | Volts |
| Terminal Resistance | 5,78 | Ohms |
| Rotor Inductance | 550 | µH |
| Torque Constant | 34,6 | mNm/A |
| Rotor Inertia | 11 | g.cm² |

Since the DC motor is specified, a transmission unit that gives the required maximum torque of 6 N.m is to be selected. No reference to any specific brand or type of transmission is given here. A

transmission unit just capable of producing the necessary amount of torque is assumed with following characteristics:

$$N_{tr} = 66$$

$$\eta_{tr} = 70\% \qquad (4.13)$$

$$J_{tr} = 0.5 \times 10^{-7} \text{ kg.m}^2$$

The selection of the transmission unit involves a detailed specification of motion transmission characteristics such as changing the motion axis properly, and calculating the strength of mechanical linkages under the given load conditions. Since these topics are out of the scope of this thesis, a realistic transmission unit performance is assumed as given in Eqn. (4.13).

## 4.2    Servo-Actuator Model Implementation

The electromechanical servo-actuation system modeling is performed in MATLAB and Matlab$^®$ Simulink using the equations derived in Section 2.3. The open loop actuator transfer function defined in Eqn. (2.41) is implemented in MATLAB and used as the plant for the PD controller design. The PD controller is cascaded to the open loop transfer function and the resulting closed loop system in Eqn. (2.43) is modeled in both MATLAB and MATLAB Simulink. In the MATLAB Simulink model, the power constraint on the operation of the servo-actuation system is also modeled.

### 4.2.1    DC Motor and Transmission Unit Modeling in MATLAB Simulink

The DC motor model implemented in MATLAB Simulink is given in Figure 44. Note that a current limit is implemented through limiting the applied voltage as:

$$V_{\min} = -I_{\lim}R \qquad (4.14)$$
$$V_{\max} = I_{\lim}R \qquad (4.15)$$

The MATLAB Simulink implementation of the transmission unit is given in Figure 45, and the servo-actuation system model is given in Figure 46. Note that the 24 V voltage limit is also implemented in the servo-actuation system model. The steady state aerodynamic hinge moment as a function of fin angle is input to the transmission unit as an external disturbance.
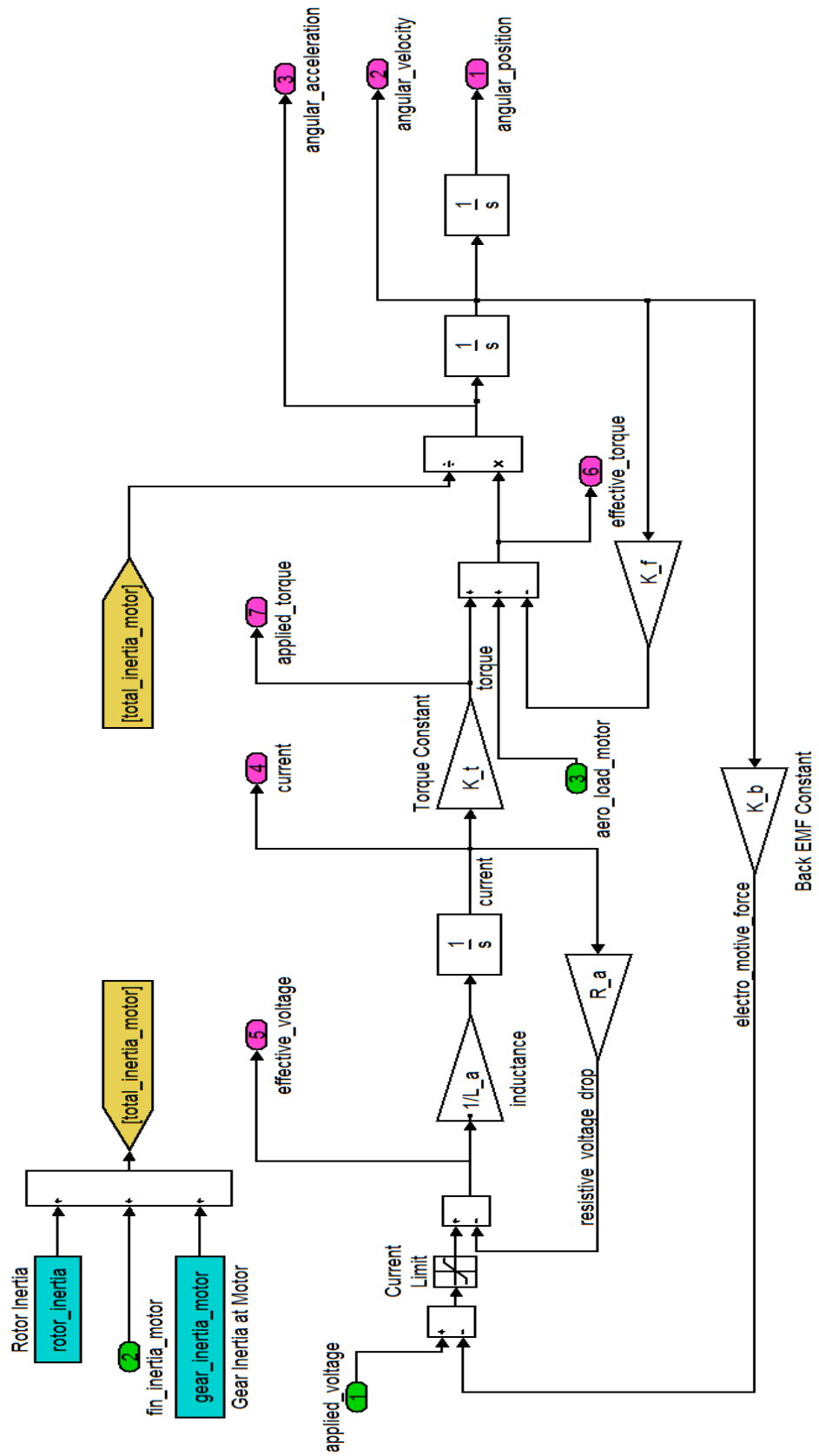
*Figure 44 DC Motor Model*
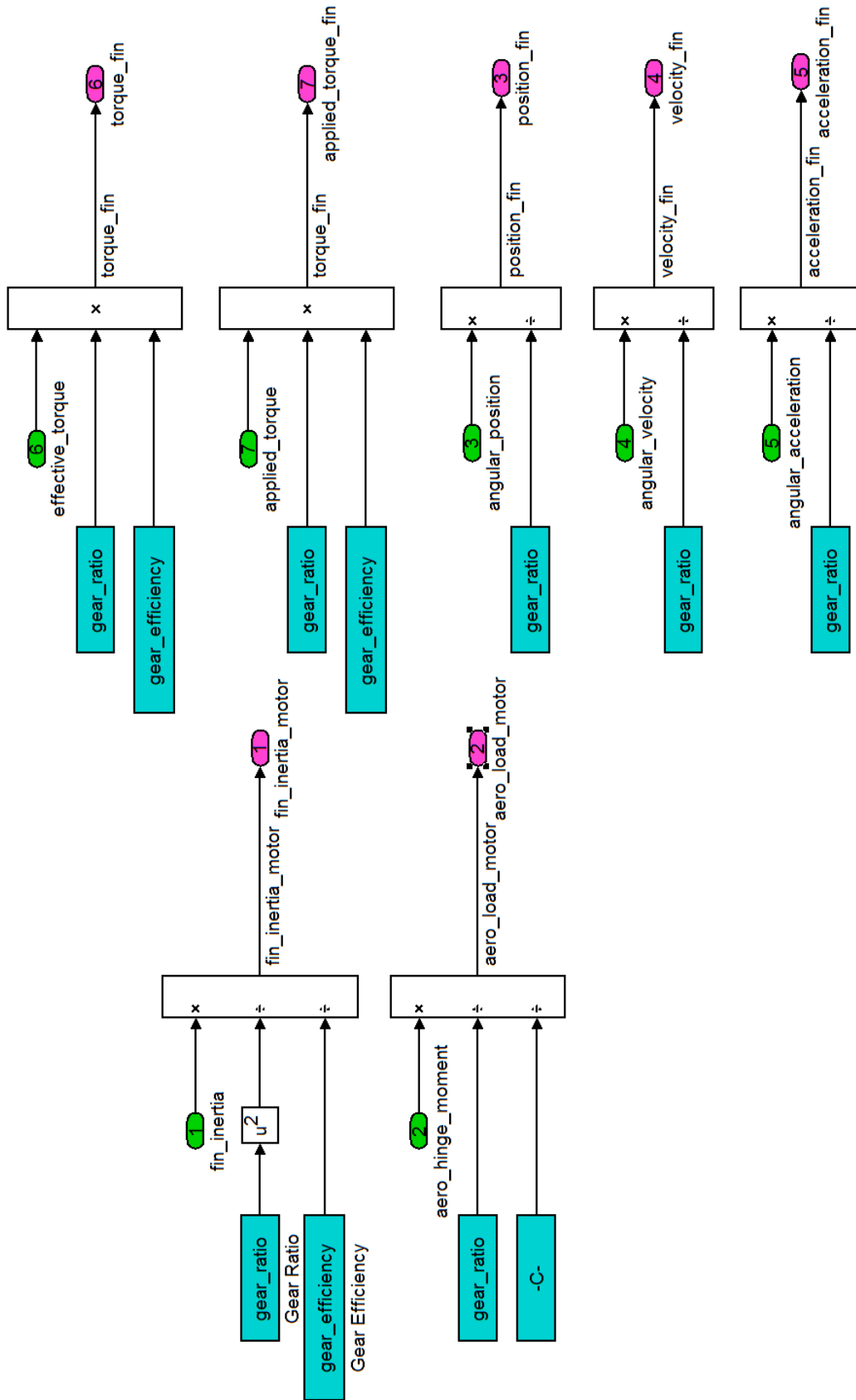
*Figure 45 Transmission Unit Model*
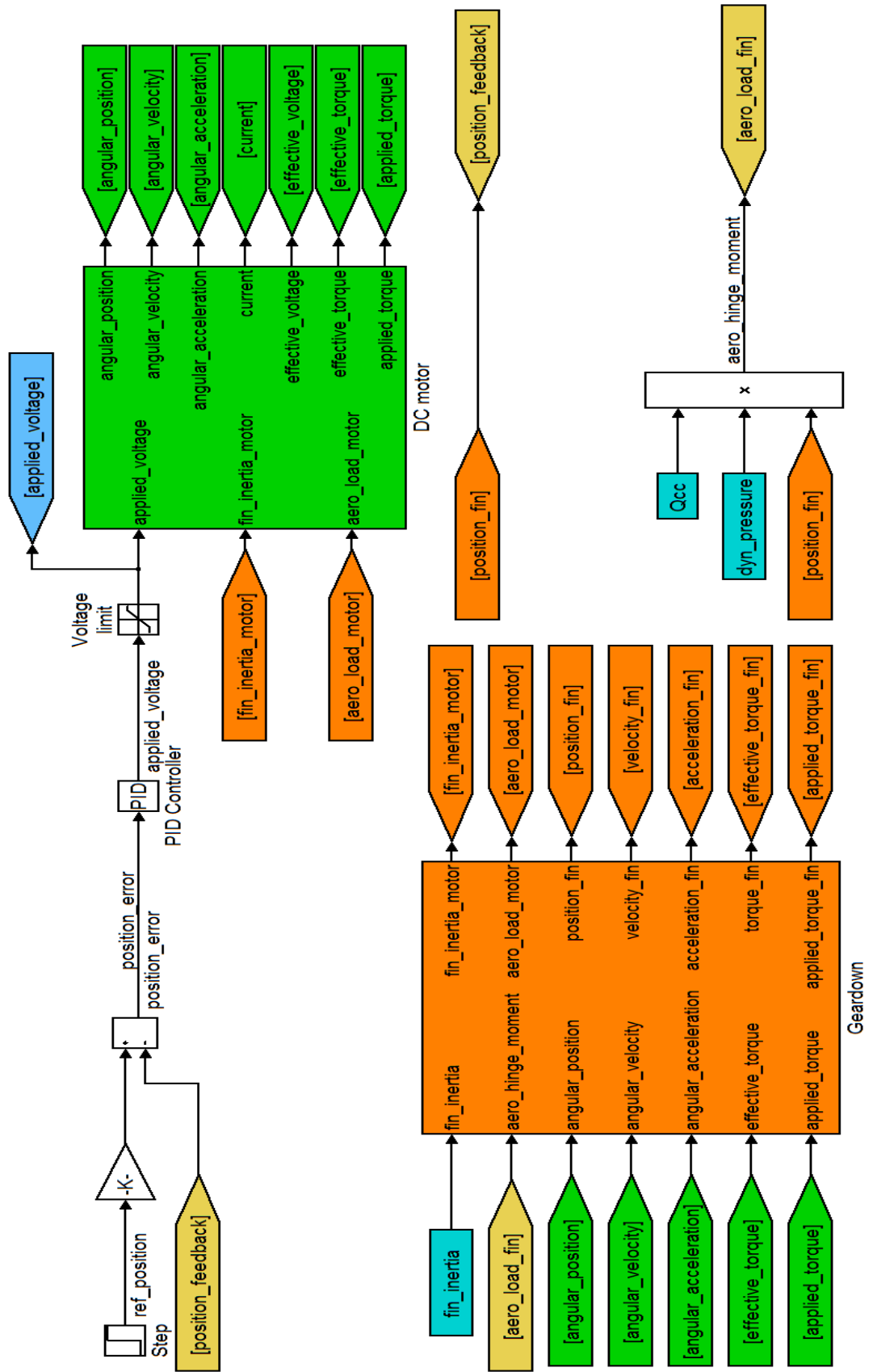
*Figure 46 Servo-Actuation System Model*

## 4.3    PD Controller Design

The controller design is carried out in the s-plane with the root locus method. The poles of the open loop actuator transfer function are given in Table 13.

*Table 13 Poles of the Actuator Transfer Function*

| Pole # | Value |
|--------|-------|
| 1 | 0,00 |
| 2 | -168,80 |
| 3 | -10340,28 |

The root locus method is a good candidate for systems having a dominant pair of poles such as given in Table 13.

The PD controller is designed to achieve the time response requirements. The aerodynamic hinge moment was assumed to be an external disturbance, while deriving the open loop actuator transfer function. Therefore the robustness of the closed loop servo-actuation system to the aerodynamic hinge moment is also assessed in PD controller design. No integral control action is preferred, because the open loop actuator transfer function (2.41) is inherently a Type I system [48], which has zero steady state error.

The root locus of the open loop actuator transfer function is shown in Figure 47. As observed from Figure 47, position response of the actuator to a voltage input is dominated by a pair of poles which reflect the mechanical characteristics of the actuator. The pole that is far away at the negative real axis is the result of the electric loop given in Figure 44.
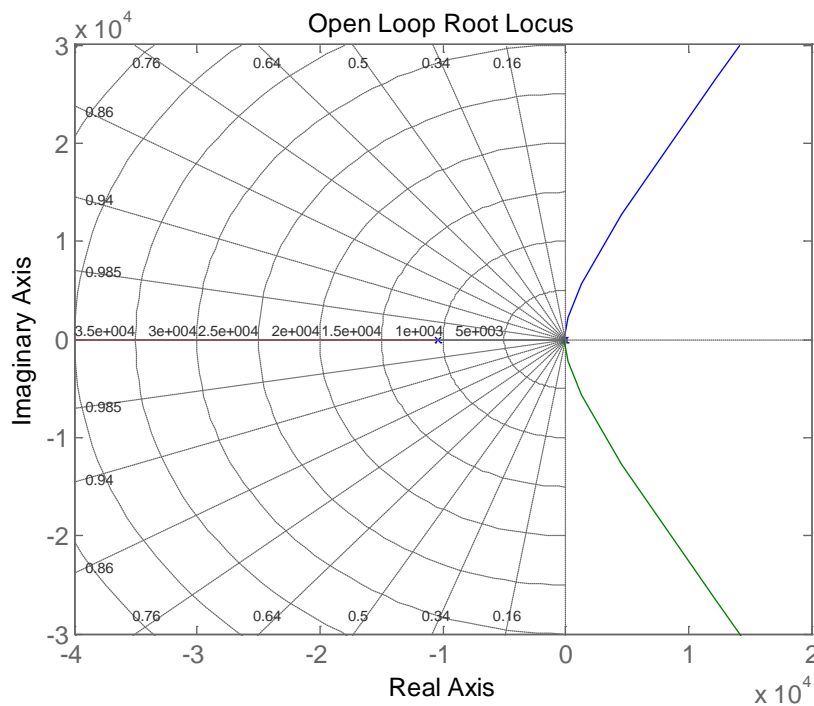


*Figure 47 The Open Loop Actuator Root Locus*

A closer look to the root locus near the origin reveals:
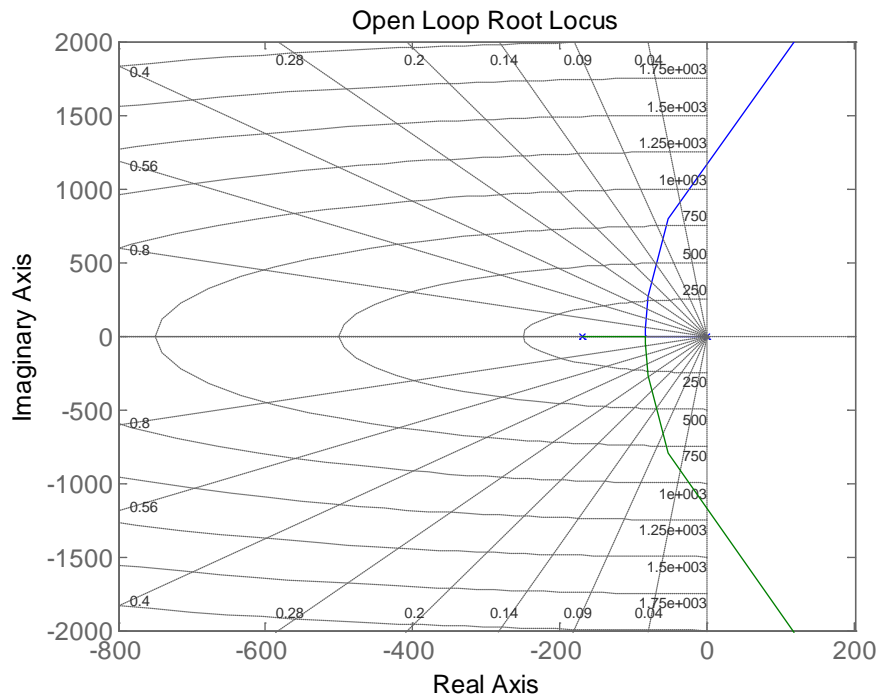
*Figure 48 The Open Loop Actuator Root Locus for Dominant Poles*

When a unity feedback system *without a controller* is formed with the actuator transfer function, assuming $K_p = 1$ and $K_d = 0$ in (2.43), the following closed loop transfer function is obtained :

$$\frac{\theta_{fin}}{\theta_{com}} = \frac{K_t}{NJLs^3 + N\left(J_{total\,@\,motor}R + cL\right)s^2 + \left(N\left(K_bK_t + cR\right)\right)s + K_t} \tag{4.16}$$

Unit step response of Eqn. (4.16) is observed in Figure 49.
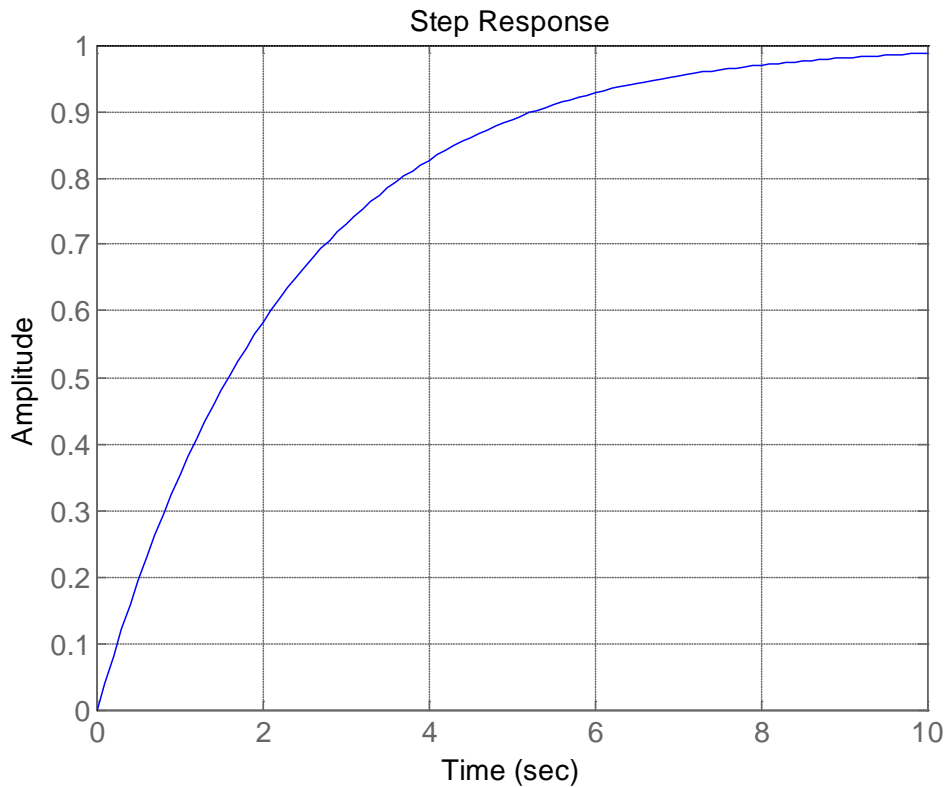
*Figure 49 Unit Step Response of Closed Loop System – No  Controller*

As observed from Figure 49, the response clearly needs to be improved. The reason the response is very slow is that, a pole very close to the origin still dominates the response, as shown in Table 14. The aim is to compensate for this effect.

*Table 14 Poles of Closed Loop System – No Controller*

| Pole # | Open Loop Actuator Poles | Closed Loop Poles without Controller |
|--------|--------------------------|--------------------------------------|
| 1 | 0,000 | -0,43 |
| 2 | -168,806 | -168,35 |
| 3 | -10340,285 | -10340,29 |

The PD controller adds a zero to the root locus in Figure 47. This improves the damping and speed of the response given in Figure 49, so as to match the time response requirements. The PD controller is cascaded to the actuator transfer function to form the forward path transfer function as:

$$G_{forward}(s) = \frac{K_c K_t (K_P + K_D s)}{Ns\left(\left(J_{total\,@\,motor}s + c\right)\left(Ls + R\right) + K_b K_t\right)} \tag{4.17}$$

where $K_c$ is the controller gain that scales $K_P$ and $K_D$.

Then with a unity feedback, the closed loop transfer function of the controlled system is obtained as:

$$\frac{\theta_{fin}}{\theta_{com}} = \frac{K_c K_D K_t s + K_c K_P K_t}{NJLs^3 + N\left(J_{total\,@\,motor}R + cL\right)s^2 + \left(N\left(K_b K_t + cR\right) + K_c K_D K_t\right)s + K_P K_t} \quad (4.18)$$

As observed from Eqn. (4.18), the PD controller added a zero and changed the location of the poles of Eqn. (4.16). These two actions speed up the response and improve damping together. The contribution to damping depends on $K_c K_D$, whereas the time response improvement depends on both $K_c K_P$ and $K_c K_D$. The added zero at $s = -K_P / K_D$ speeds up the response. Because the aim is to speed up the response with no overshoot, the characteristics of the system is altered accordingly. The root locus of the forward path transfer function is shown in Figure 50, for two different zero locations, both on the left of the second dominant pole $s = -168.806$ of the open loop system, when $K_c = 1$. The zero locations are selected to the left of the second dominant pole so that the system response is adjusted to be faster.
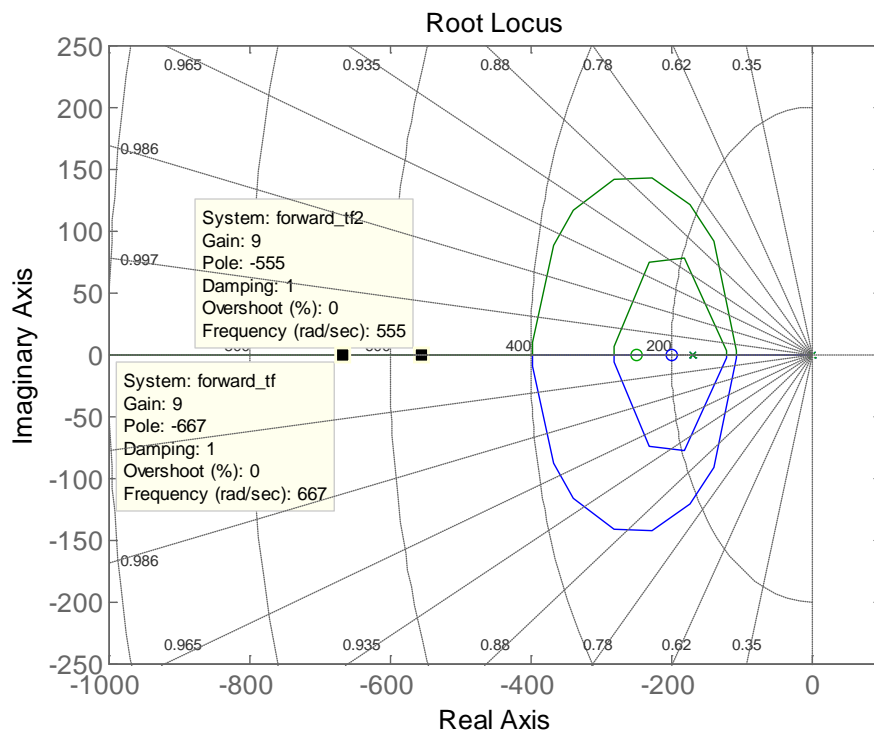


*Figure 50 Root Locus of Alternative Compensated Systems*

The zeros are placed at $s = -200$ and $s = -250$ respectively.

There is always a limit on how much the controller gain $K_c$ can be increased or how far away the zeros can be selected. This limit is due to the hardware implementation of the control system. The operating frequency of the digital control system implemented for the servo-actuation system is given as 1 kHz in Table 2. Therefore the fastest dynamic in the controller should be below 10% percent of this value for proper operation. Then the limit on the fastest pole is obtained as:

$$s_{\min} \geq -628.32 \text{ rad/s} \quad (4.19)$$

Figure 50 states that, as the controller gain $K_c$ is increased, the system gets faster without becoming unstable. According to Figure 50, the same $K_c$ gives different closed loop systems for different zero locations as given in Table 15.

*Table 15 Closed Loop Poles of Alternative Systems*

| | Controller Gain | Closed Loop Zero | Closed Loop Pole 1 | Closed Loop Pole 2 | Closed Loop Pole 3 |
|---|---|---|---|---|---|
| System 1 | 9,0 | -200 | -214,381917 | -666,563583 | -9628,15 |
| System 2 | 9,0 | -250 | -321,484467 | -555,387425 | -9632,22 |

These two systems with different zero locations differ in response characteristics. The one with the more negative zero responds faster to disturbances and is therefore more robust. Note that the second pole of the first system is above the specified $s_{\min}$, thus will be considered unacceptable. It is not possible to have $K_c$ higher than 9, when the zero is at $s = -200$. Therefore if higher $K_c$ is needed, the zero should be placed to the left of $s = -200$. Unit step responses of these systems are given in Figure 51.
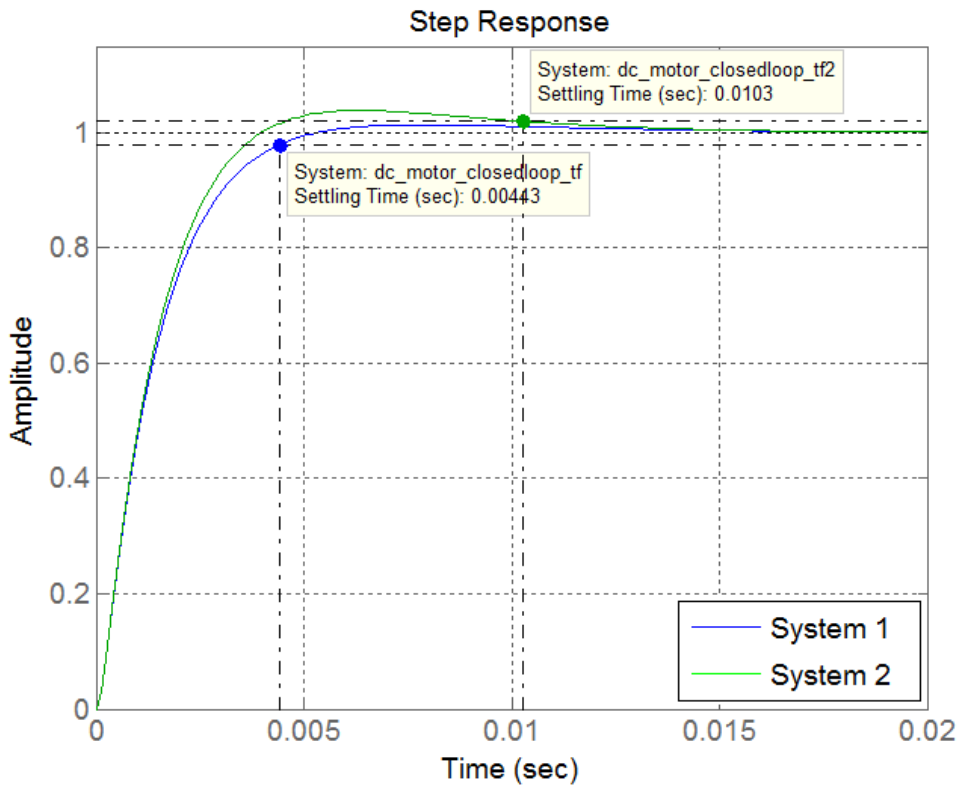


*Figure 51 Step Response of Alternative Linear Closed Loop Systems*

According to Figure 51, both systems are quite fast, the second one being faster, because the location of the zero is further away on the negative real axis. In the nonlinear system with power source limits, the system that performs faster in linear analysis may be advantageous. Also, it is possible to increase the controller gain $K_c$ further for the second system before reaching the limit $s_{\min}$. When the second system is simulated with power source limits by the model presented in Section 4.2.1, the step response to 14° angular position command is as follows:

70
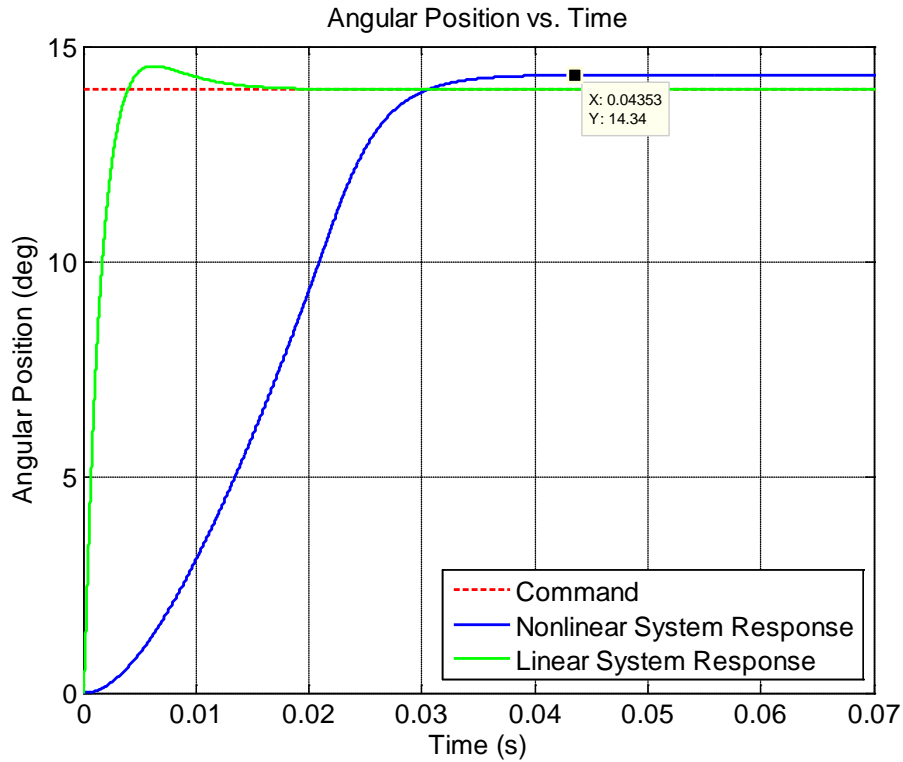
*Figure 52 Step Response of System 2 to 14° Command (Linear vs. Power Limited Nonlinear)*

The difference between linear and power limited nonlinear systems are summarized in Table 16.

*Table 16 Linear vs. Power Limited Nonlinear System Properties*

|  | Nonlinear System | Linear System |
|---|---|---|
| Voltage limit | 24 V | None |
| Current limit | 10 A | None |
| Aerodynamic hinge moment | Steady Aerodynamic Moment | None |

The steady aerodynamic hinge moment varying with angular position is applied to the nonlinear system, to check the closed loop system response under anticipated loading conditions. Although the system has no overshoot, the steady state error is not acceptable according to the specification which is given as 2%. To meet the 2% requirement the PD controller is tuned such that $K_c = 10$, $K_P = 275$ and $K_D = 1$, and a third system is formed. The step response of System 3 to 14° angular position command is given in Figure 53.
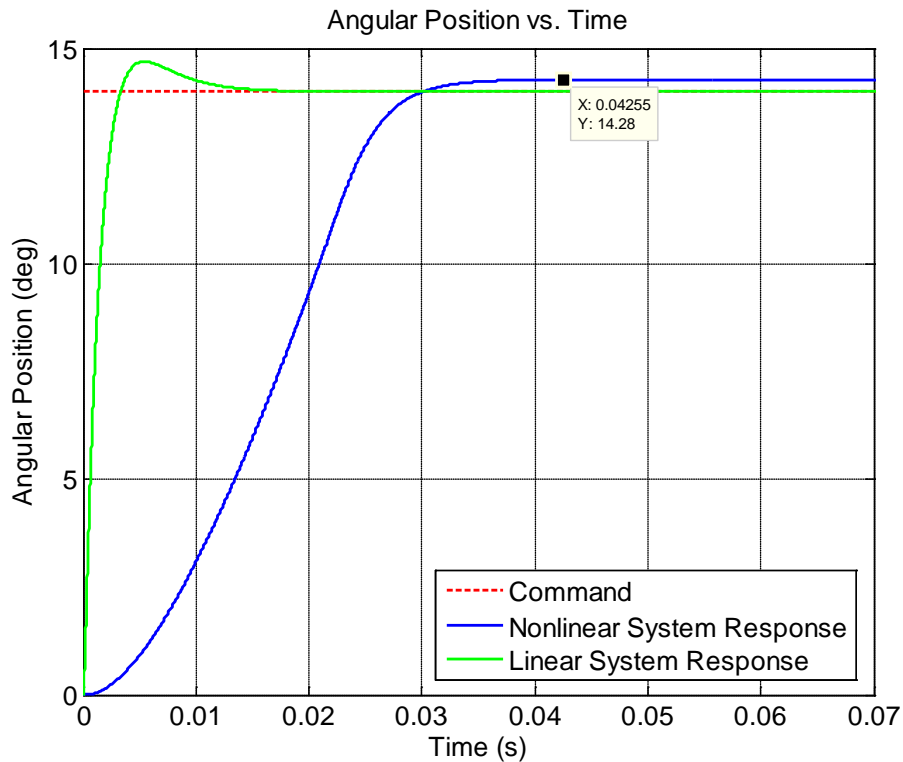
*Figure 53 Step Response of System 3 to 14° Command (Linear vs. Power Limited Nonlinear)*

According to Figure 53, the settling time is well below 50 ms for the final system. The poles of System 3 are given in Table 17.

*Table 17 Closed Loop Poles for Controller Gain – Zero Pairs of Alternative Systems*

|  | Controller Gain | Closed Loop Zero | Closed Loop Pole 1 | Closed Loop Pole 2 | Closed loop Pole 3 |
|---|---|---|---|---|---|
| System 1 | 9,0 | -200 | -214,38 | -666,56 | -9628,15 |
| System 2 | 9,0 | -250 | -321,48 | -555,38 | -9632,22 |
| System 3 | 10 | -275 | -378,25 | -581,96 | -9548,87 |

Note that, the final system meets the steady state error requirement, settling time requirement and overshoot requirement all together. The steady state error requirement is more demanding than the others, therefore the system turned out to be faster than required. The fastest dynamic of the dominant system poles is -581,96 rad/s, and is in compliance with $s_{min}$ requirement. The third pole is far away from the imaginary axis in all of the closed loop system tuning process, therefore the 'dominant poles' assumption is not violated.

The gain margin and the phase margin for the forward path transfer function are infinity and 78.4 degrees respectively. The gain margin being infinity is in compliance with the root locus diagram given in Figure 50, implying that the controller gain can be increased without making the system unstable. The Bode plot of the actuator is given in Figure 54.
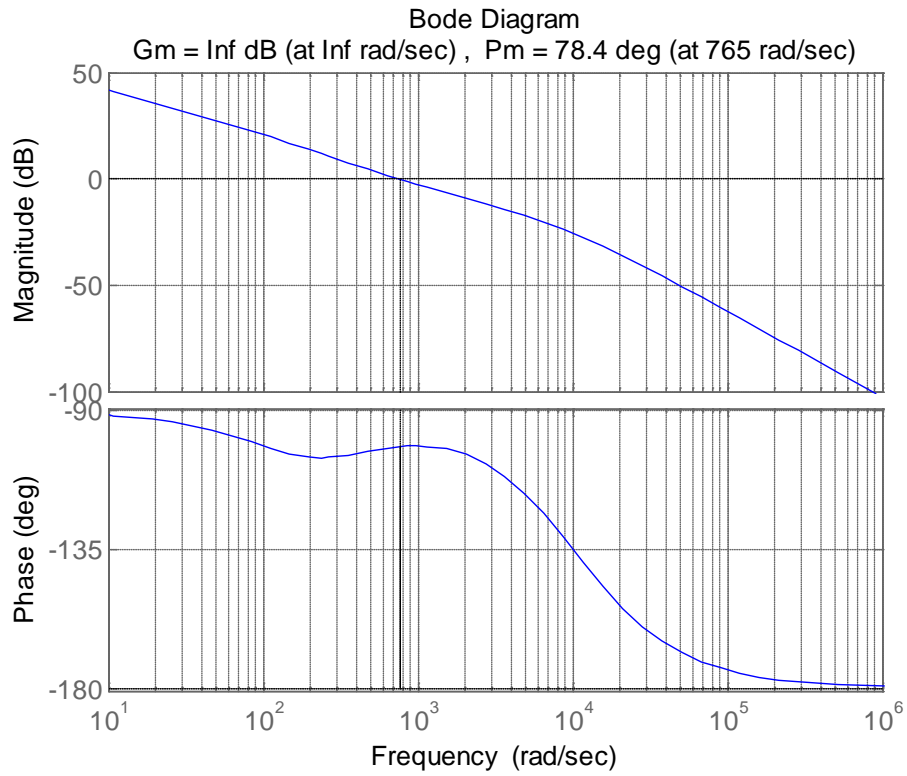
*Figure 54 Bode Plot of the Closed Loop Servo-Actuation System*

The position, velocity and torque profiles are presented for a -15° command when the initial condition is 15°. This is the condition that would slow down the servo most, because $Q_{cc}^{real}(0.6, 0.001)$, which is the steady state aerodynamic moment, is positive, thus creates a de-centering effect.
.
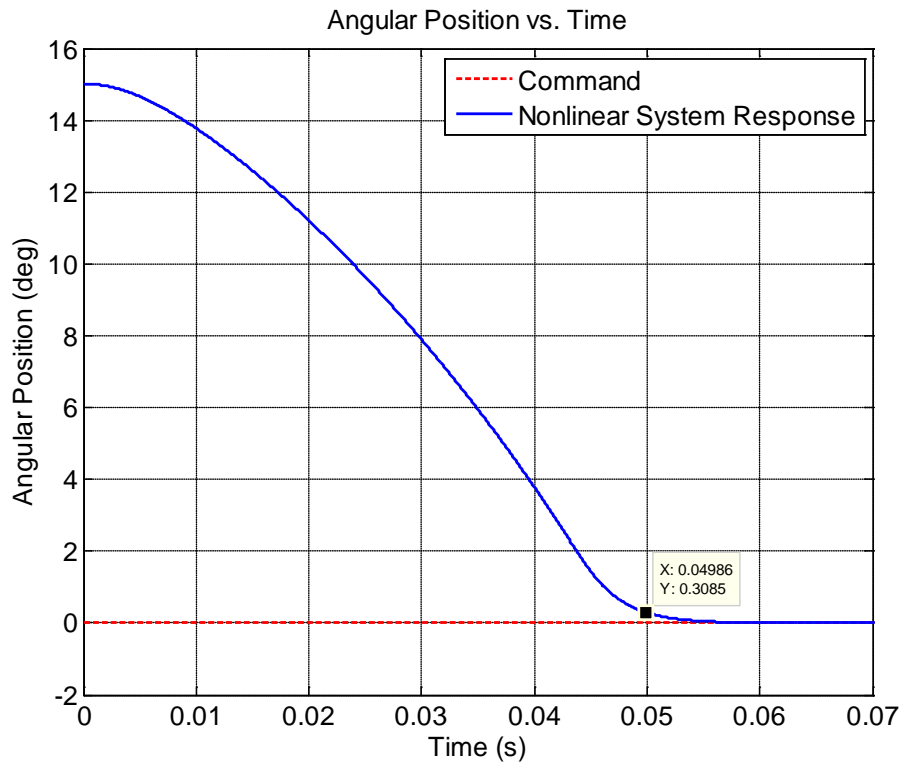
*Figure 55 Angular Position Response of the Power Limited Nonlinear System*
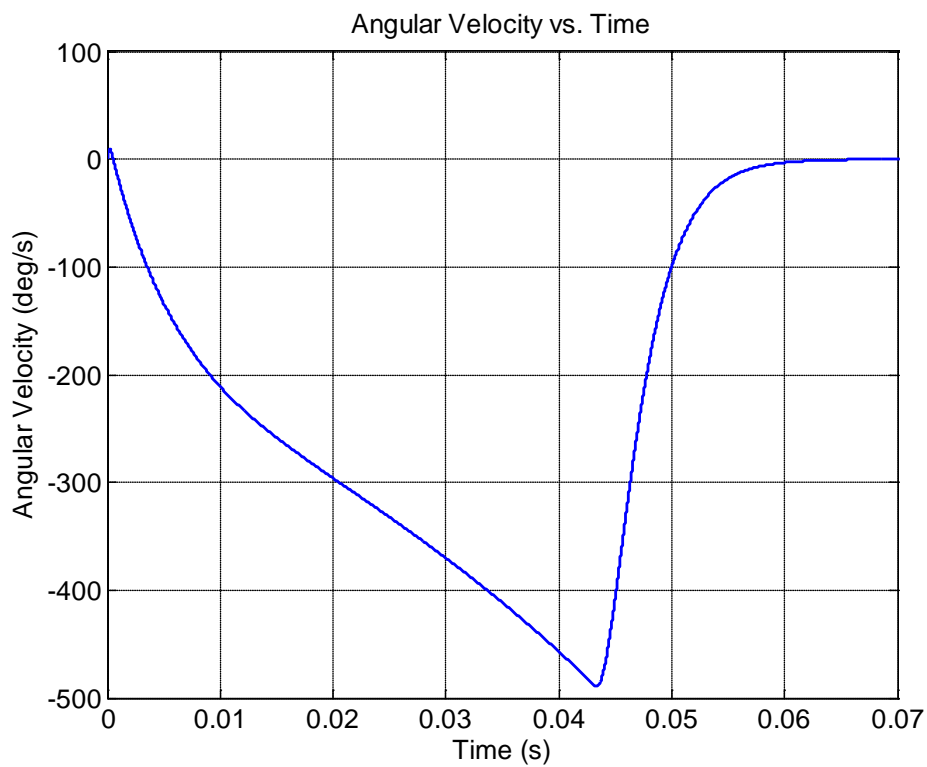


*Figure 56 Angular Velocity of the Power Limited Nonlinear System*
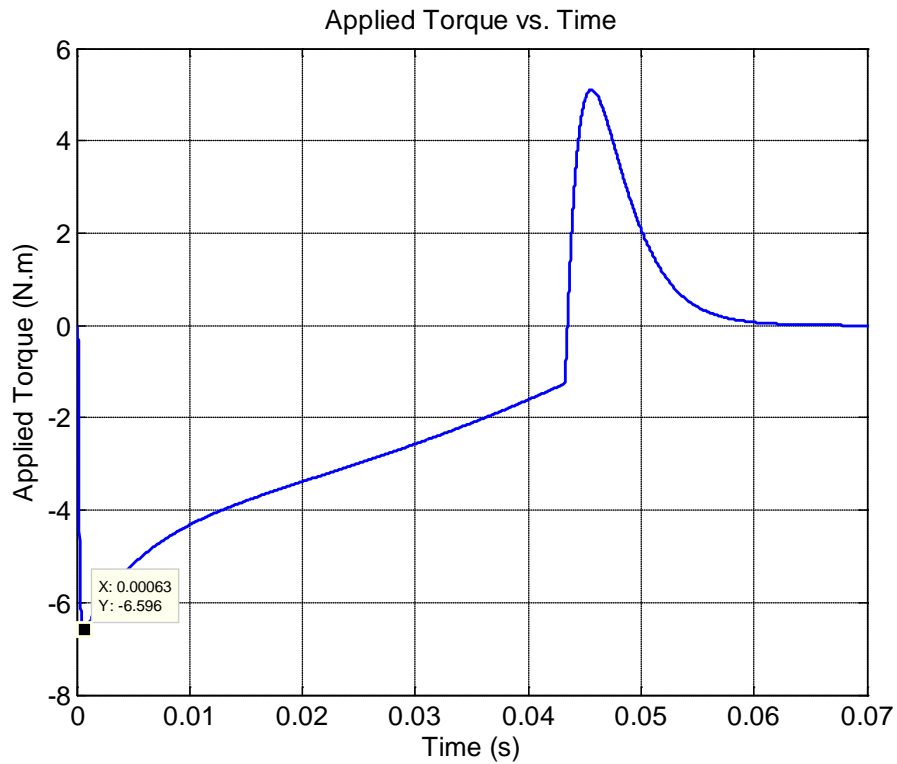
*Figure 57 Applied Torque for the Power Limited Nonlinear System*

According to Figure 55, Figure 56 and Figure 57, the system was able to create approximately 6.6 N.m torque and rise to approximately 500 °/s angular velocity, while settling at the commanded position in less than 50 ms. Although the required angular velocity was only 300 °/s, a faster system was necessary to obtain the required steady state error under anticipated steady aerodynamic loading.

**CHAPTER 5**

**AEROSERVOELASTIC MODELING**

In this chapter, in order to exploit the overall frequency and time response behavior of the missile control fin under given operating conditions, the aeroelastic model and the servo-actuation system model developed in Chapter 3 and Chapter 4 are integrated. The resulting model is shown to inherit the major behavior that should be addressed for control design purposes. The 'rigid fin' – 'steady aerodynamic loading' assumption that lead to the PD controller synthesis is discussed. The steps taken to interconnect the aeroleastic model and the servo-actuation system model are explained together with the feedback path generated through the aerodynamic hinge moment. Linear and power limited nonlinear versions of the aeroservoelastic system are generated and resulting differences are discussed. The effects of digital implementation of the controllers and sensors are neglected.

**5.1    Integration of Aeroelastic System and Servo-Actuation System Models**

State space model representations of the actuator and the aeroelastic fin were derived in Chapter 2. In this section, these models are integrated such that the hinge moment output given in Section 2.4 is fed back to the actuator as a disturbance. This feedback mechanism is modeled in MATLAB Simulink, for power limited nonlinear and linear analysis purposes. By utilizing the MATLAB command 'lft'[43] for generalized feedback interconnection of the actuator and the aeroelastic fin, the linear transfer function of the final aeroelastic open loop system is obtained. Figure 58 describes the feedback path for the hinge moment.
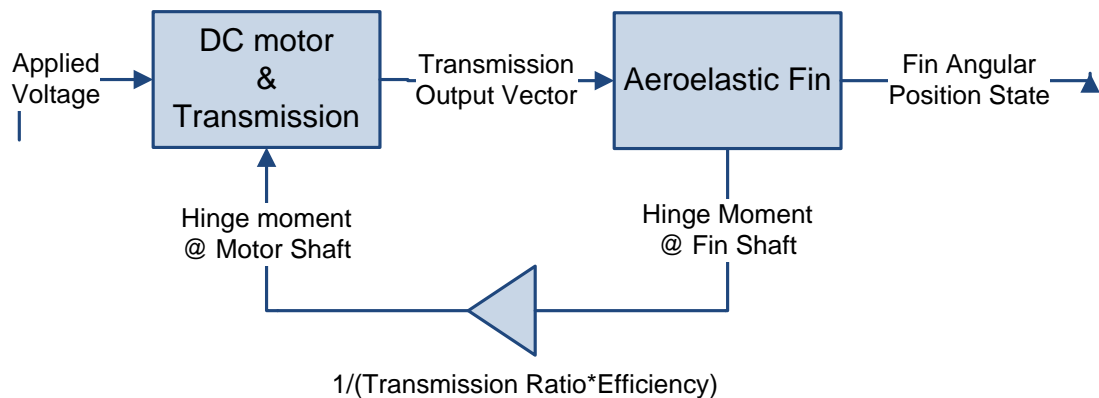


*Figure 58 Open Loop Actuator & Aeroelastic Fin System*

The system presented in Figure 58 is the actual open loop system to be controlled. Note that the control design was carried out neglecting the elasticity effects and the unsteady aerodynamic effects on the fin. In that case the open loop transfer function is depicted as below:

*Figure 59 Open Loop System Subjected to Control Design in Chapter 4*

Note that the aerodynamic hinge moment was taken as an unknown disturbance.

Two types of aeroservoelastic model topology are used for frequency and time domain analysis. The topologies differ in terms of the feedback signal of the controller.

Aeroservoelastic Model 1 is assumed to have an absolute encoder that perfectly measures the motor shaft position. The topology of Aeroservoelastic Model 1 is described in Figure 61.
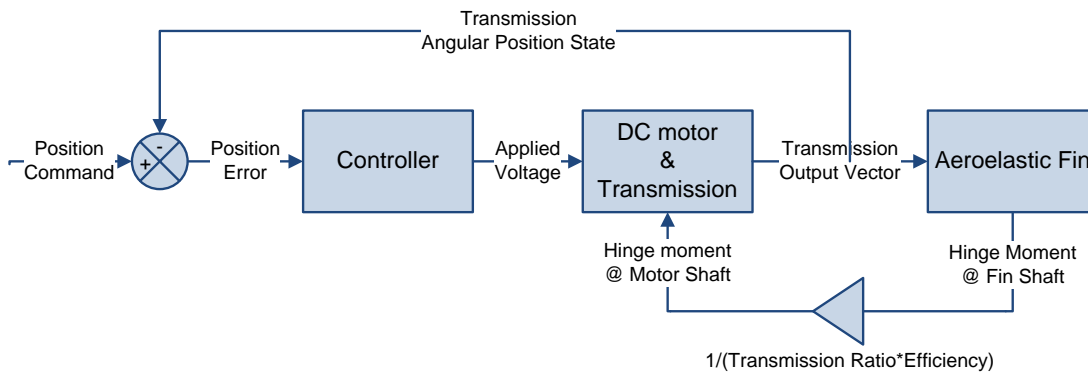


*Figure 60 Aeroservoelastic Model 1 Topology*

Aeroservoelastic Model 2 is assumed to have a potentiometer at the fin shaft that directly measures the angular deflection at the fin root. The dynamics and measurement errors related to the potentiometer are neglected.
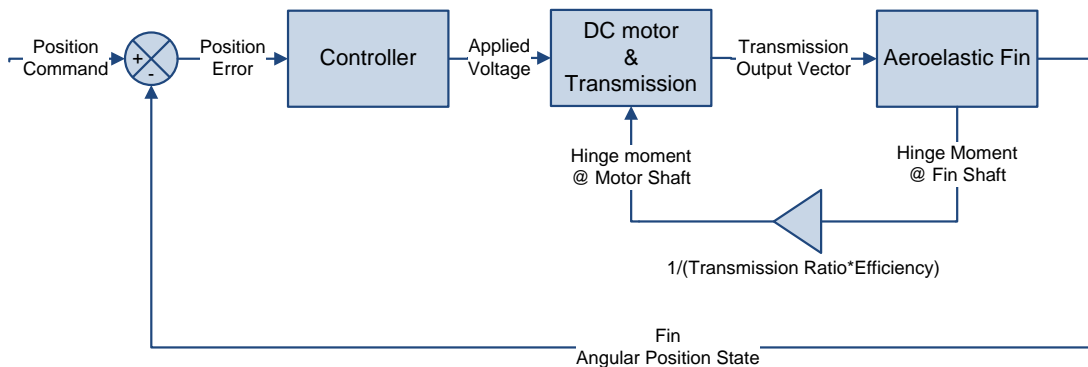


*Figure 61 Aeroservoelastic Model 2 Topology*

### 5.1.1   Preface to the Aeroservoelastic Model Analysis

In this chapter, time domain simulations of Aeroservoelastic Model 1 (AEM1) and Aeroservoelastic Model 2 (AEM2) are performed. The time response requirements of the servo-actuation system were 50 ms for the settling time and 2% for the steady state error.

There are a number of motives for satisfying the desired angular positioning accuracy, speed of response and static or dynamic stability of an all-movable control surface. These motives can be classified into two main categories:

- Irreversible phenomena which lead to the loss of the flight vehicle due to an instability at the control surface.
- Side effects, which reduce the efficiency of control on the flight vehicle or shorten the lifetime of the control surface and its interfacing components.

An irreversible phenomenon which leads to the loss of the flight vehicle may be due to the loss of structural stability or control stability of the control surface. The structural stability of the control surface can be lost due to an aeroservoelastic instability such as flutter. If the lift or moment values on the control surface are more than the values that it is design to withstand, the control surface may break.

Another irreversible outcome may be the loss of functioning due to unbearable steady aerodynamic loads than that of expected. This result may be due to an unexpected increase in steady lift, steady moment or an unwanted change of the center of pressure on the control surface. The loss of the control surface, especially for a missile, most probably would lead to the loss of the flight vehicle.

The control stability may be lost, due to the interaction of oscillatory aeroelastic dynamics and the servo-actuation system dynamics. If the frequency separation between the aeroelastic instability frequencies and the servo-actuation system bandwidth is not large enough, the two dynamics may interact in an unwanted manner that would lead to the loss of control stability and structural stability of the control surface at the same time. The loss of control stability may lead to the loss of control stability of the vehicle.

Although the control surface structural and control stability is not lost, the side effects due to aeroservoelastic interaction may impose problems on both flight vehicle's and control surface's design objectives. The nature of the response becoming oscillatory due to the aeroservoelastic interaction, for instance, would have an undesired effect on the power consumption of the servo-actuation system. For missiles, the amount of power onboard is limited due to tight packaging options. Therefore the increase in the power consumption may cause a missile to fail its mission, or at least reduce its effective range when the aeroservoelastic interaction is known and accepted. For flight vehicles that are used in long term, such as airplanes, oscillatory positioning response may cause the structures to wear. Although this is not a sudden failure situation, it may affect flight comfort and maintenance costs.

The oscillatory behavior or unwanted static deflection of the control surface may also cause the overall control system of the flight vehicle to intervene with the situation and try to compensate for the unwanted effect. This intervention in turn, may cause the flight vehicle to make unwanted motions that would reduce the flight performance or even affect overall flight stability.

In Figure 62, a generic block diagram of a missile control system whose guidance produces acceleration commands is shown.
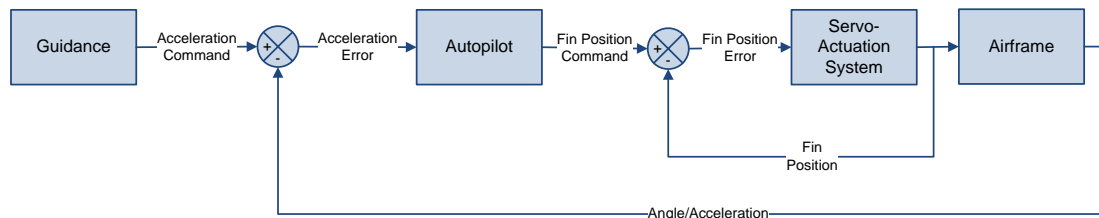


*Figure 62 Generic Missile Control System Block Diagram*

In order to understand the effects of an undesired response at a missile control fin on the overall control system, the basics of dynamics of the missile control system should be understood. The functions of the blocks represented in Figure 62 are summarized below.

*Guidance:* Generates the steering commands, such as the amount of lateral acceleration that the missile should have, the Euler Angles that the missile should orient itself to achieve its current goal.

*Autopilot:* Generates the control fin angular position commands, such that the missile fulfills the command given by the guidance.

*Servo-Actuation System:* Realizes the angular position commands.

*Airframe:* Responds to control fin position by changing incidence, Euler Angle, acceleration etc.

Since the servo-actuation system is a control system that is involved in another control system, the response that it generates interacts with the overall control system. For instance, if the frequency separation between the fin motion frequency content and the airframe bandwidth is not large enough, the airframe would be affected. Then the autopilot would try to compensate in turn. For example, the rolling dynamics is the fastest dynamics for a skid-to-turn missile that involves short spanned lifting surfaces, due to low roll damping and low roll inertia of the airframe. For an agile missile, instability or an oscillatory response at the control fin may easily interact with the roll dynamics and cause the missile to oscillate. Then, when the autopilot tries to compensate; the oscillation may grow, may be sustained, or may be attenuated depending on the autopilot bandwidth.

For the conservative structural designer, to be on the safe side, in the absence of aeroelastic and aeroservoelastic modeling, the decision would be to design stiffer and heavier structures that would reduce flight performance. For the conservative control system designer, accounting for the uncertainty of the models that do not include these phenomena may require larger stability margins, higher robustness, and in turn lower performance in the frequency range of operation. Therefore, on the conservative side, there is still the trade-off.


## 5.2 Open Loop Aeroservoelastic System Behavior

Since the transfer functions and state space representations of the actuator, and the aeroelastic fin are obtained, linear frequency domain analysis for the open loop system can be performed. In Figure 63, the Bode plot of several combinations of transfer functions are given. Three types of open loop transfer functions are analyzed. Note that the aeroelastic transfer functions depend on the Mach number and altitude, which are selected as Mach 0.5 and sea-level respectively. The open loop transfer functions inspected are summarized below:

- OPLOOP 1: The open loop transfer function that relates the transmission output to the applied voltage. This transfer function is the actuator transfer function that was subjected to PD controller design in Section 4.3.
- OPLOOP 2: The open loop transfer function that relates the transmission output to the applied voltage by adding the dynamics of the aeroelastic hinge moment as given in Figure 58. Note that the hinge moment is composed of elastic, aerodynamic and inertial effects. The output of this transfer function is the feedback signal of Aeroservoelastic Model 1 presented in Figure 60.
- OPLOOP 3: The open loop transfer function that relates the angular position at the fin root to the applied voltage by adding the dynamics of the aeroelastic hinge moment and aeroelastic motion of the fin as given in Figure 58. The output of this transfer function is the feedback signal of Aeroservoelastic Model 2 presented in Figure 61.
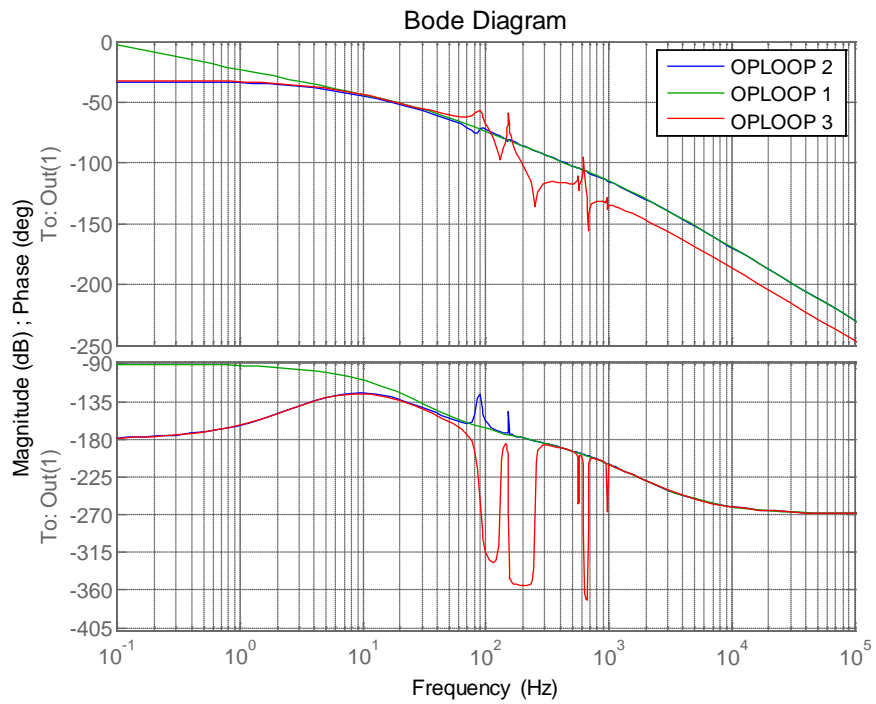
*Figure 63 Comparison of Frequency Response of Open Loop Systems*

By inspecting Figure 63, it is observed that if the feedback signal is selected as the output of OPLOOP 3, at least an oscillatory response with certain frequencies is expected without a proper controller. These frequencies are actually the natural frequencies of the system obtained by combining the servo-actuation system & aeroelastic fin at Mach 0.5 and sea level. Their values are a bit different from the structural natural frequencies. The first two resonant frequencies are shown in Figure 64, as 89.1 Hz and 152 Hz respectively. OPLOOP 3 is shown to have a problematic phase behavior.
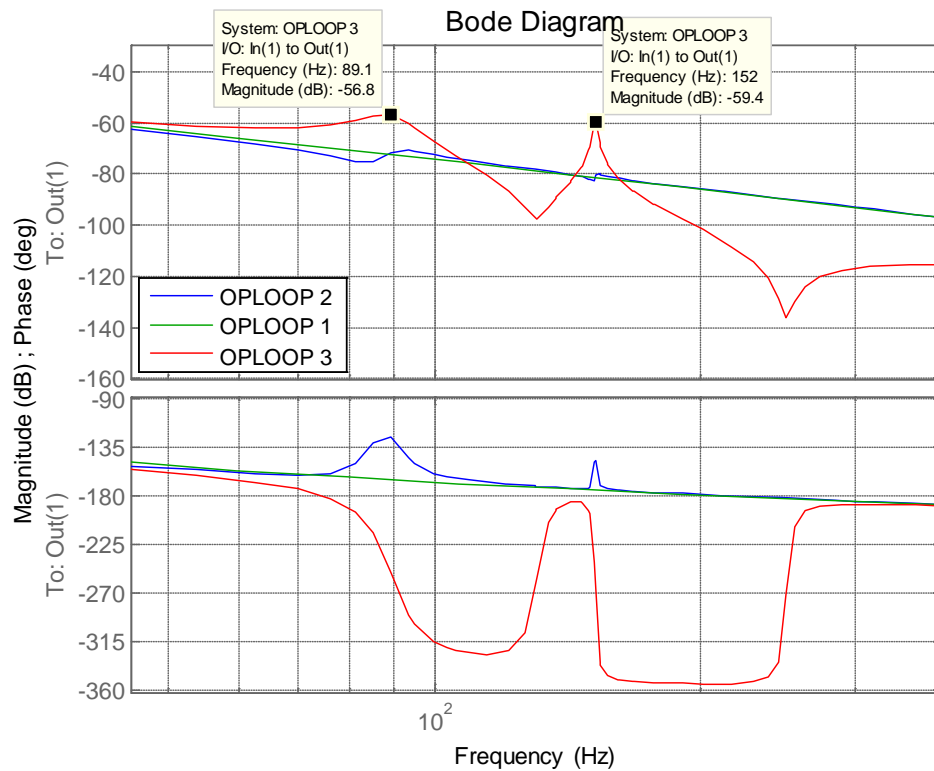
*Figure 64 Natural Frequencies of OPLOOP 3*

The state-space model built is considered to accurately represent the expected oscillatory behavior, although it is still statically stable without a controller. Note that the open loop systems inspected are all linear and possess no limit on voltage and current gains. The actual system will differ in response due to this nonlinearity.

When the PD Controller designed is cascaded to OPLOOP 1, OPLOOP 2 and OPLOOP 3, three types of forward path transfer functions are obtained:

- FWTF 1: The forward path transfer function designed in Chapter 4.
- FWTF 2: The forward path transfer function as given in Aeroservoelastic Model 1.
- FWTF 3: The forward path transfer function as given in Aeroservoelastic Model 2.

Bode plots of open loop transfer functions and forward path transfer functions are compared in Figure 65 , Figure 66, Figure 67 and Figure 68. Figure 65 shows the frequency response of the forward path transfer function obtained in Chapter 4. FWTF 1 has no high frequency resonances as observed. The gain margin is infinity and the phase margin is 79.5° with a gain crossover frequency of 131 Hz. The controller has clearly improved both the magnitude and phase response of OPLOOP 1.
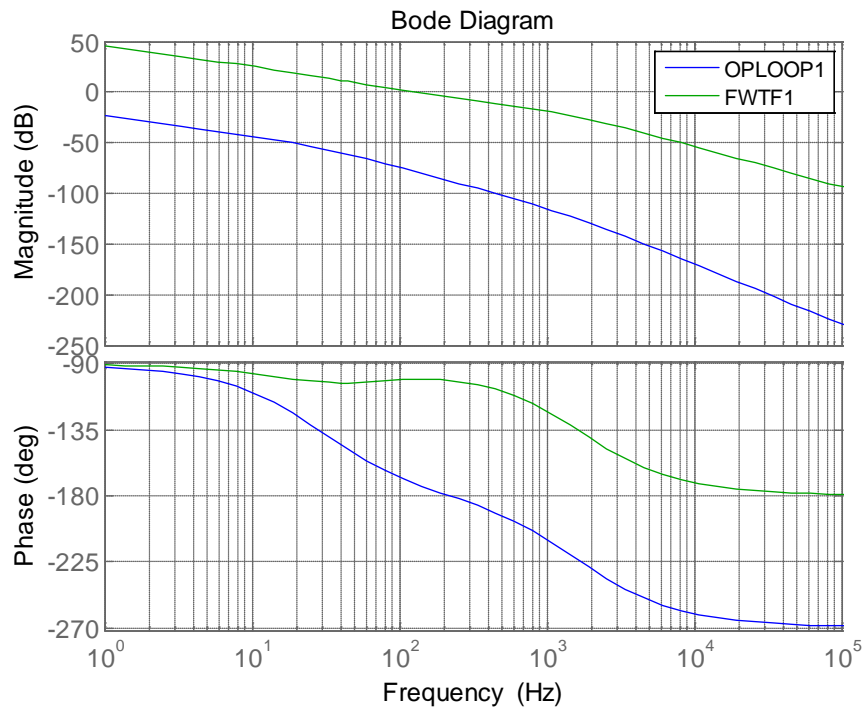
*Figure 65 Frequency Response of FWTF 1*

Figure 66 shows the frequency response of the forward path transfer function FWTF 2 obtained for Aeroservoelastic Model 1. This transfer function relates the transmission output including the aeroelastic hinge moment dynamics. It is observed that a closed loop system formed by FWTF 2 will not be far away from desired, since the feedback signal is chosen to be the transmission output. The magnitude responses of the three outputs have weak high frequency resonances by means of magnitude.
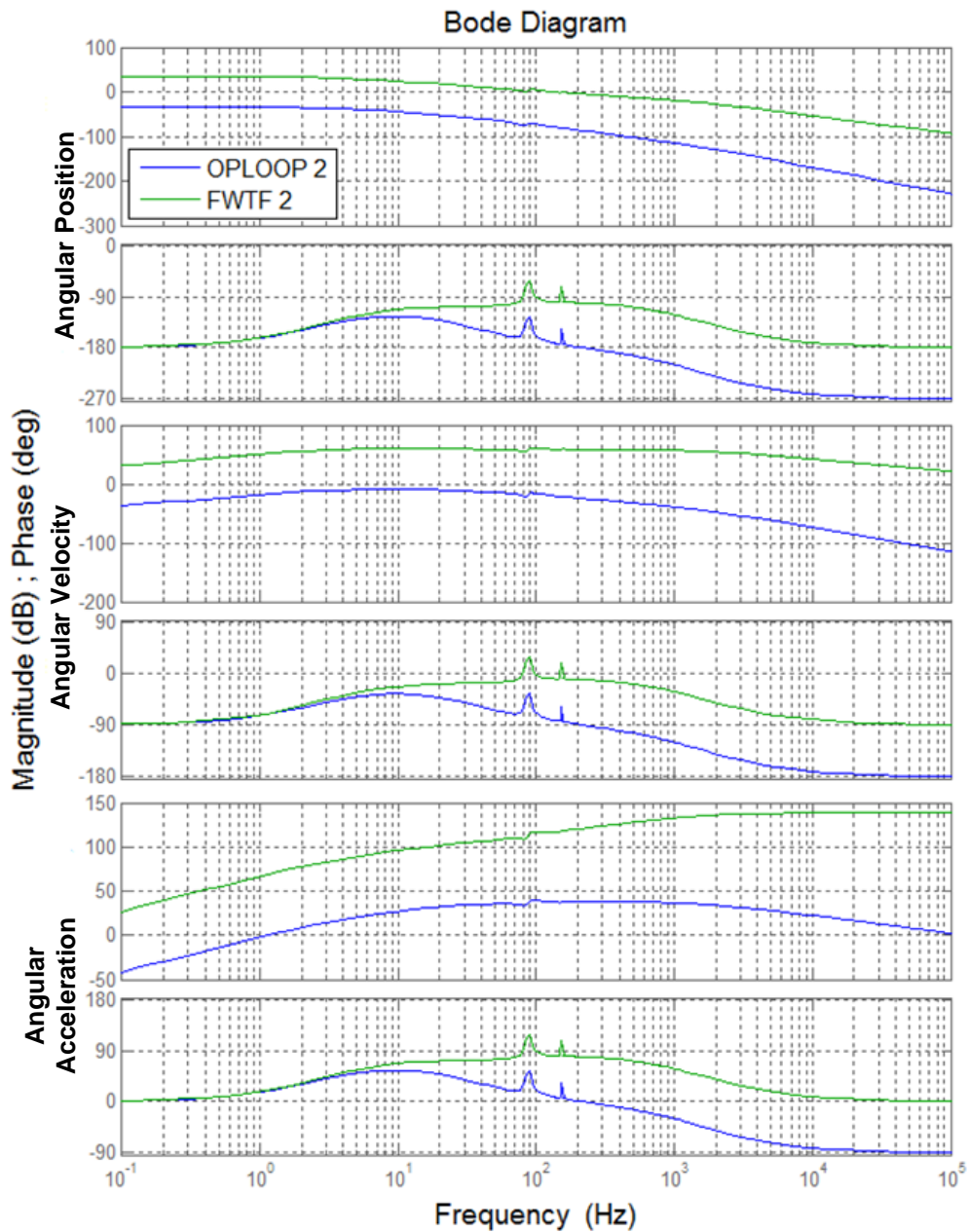
*Figure 66 Frequency Response of FWTF 2*

The three outputs of the state space model of FWTF 2 are stored in the transmission output state vector. These are the angular position, angular velocity and angular acceleration at the transmission output, which are in turn fed to the aeroelastic fin model. Note that FWTF 2 inherits the aeroelastic hinge moment dynamics via the feedback path given in Figure 60. The position output is given in Figure 67.
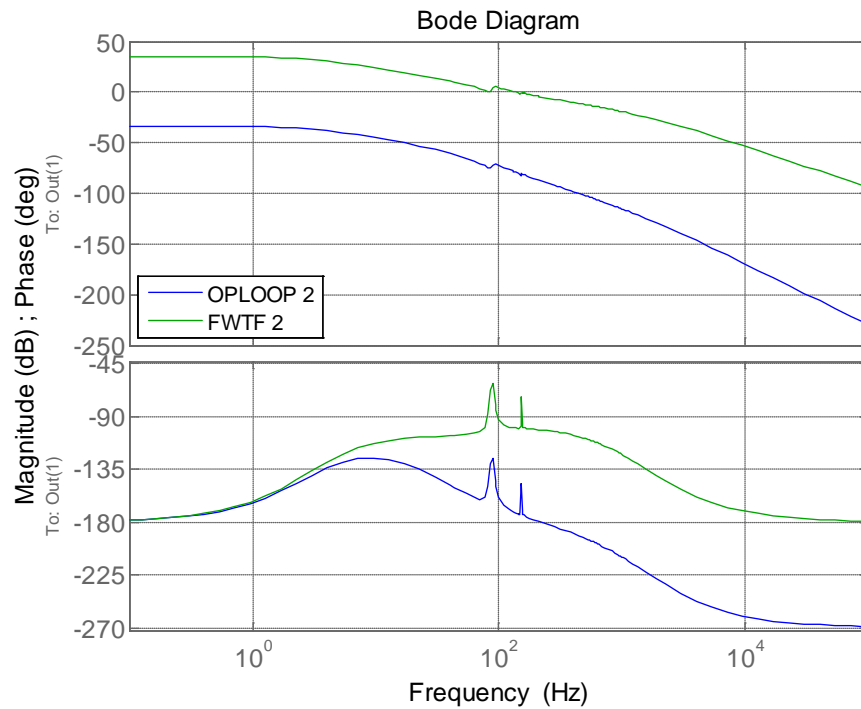
*Figure 67 Frequency Response of FWTF 2 for Position*

It is observed that the position response has not changed much when compared to FWTF 1. Thus, the servo-actuation system is considered to be robust to the aeroelastic hinge moment dynamics, when the feedback signal is selected to be the transmission output angular position. The gain crossover frequency is at 135 Hz with a phase margin of 80.2°. The gain margin is again infinity.

Figure 68 shows the frequency response of the forward path transfer function FWTF 3 obtained for Aeroservoelastic Model 2. This transfer function relates the fin angular position output including the aeroelastic hinge moment dynamics and the elastic motion of the fin shaft. The resulting system has multiple gain and phase cross over frequencies, all of which are closed loop unstable. Note the first gain margin at the first phase crossover frequency, which is about -19 dB, where as the FWTF 2 had infinite gain margin. It is shown that having the fin root angular position as in FWTF 3 as the feedback signal will render the system unstable. On the other hand, this result is questionable when the power source limit is employed in a nonlinear model, since the nonlinear system bandwidth would be smaller.
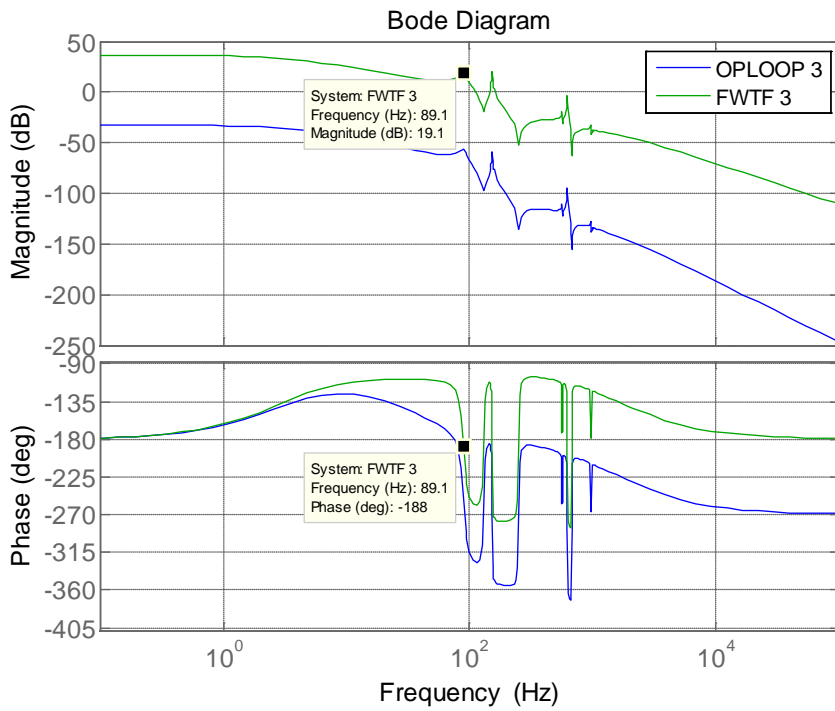
*Figure 68 Frequency Response of FWTF 3*

Finally Bode plots of FWTF 1, FWTF 2 and FWTF 3 are given for comparison, in Figure 69.
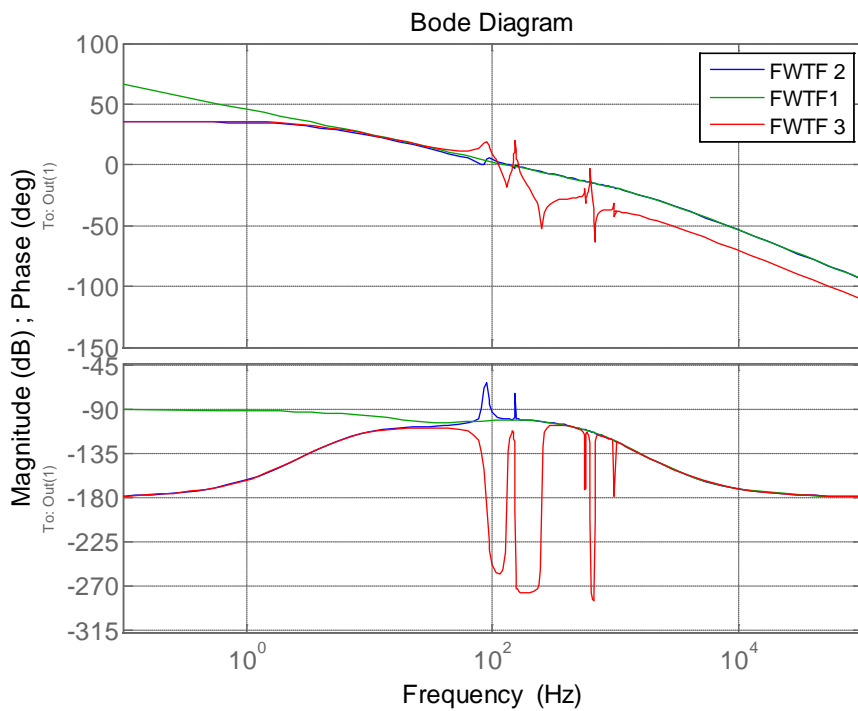


*Figure 69 Comparison of Magnitude and Phase Responses of Forward Path Transfer Functions*

## 5.3    Closed Loop Aeroservoelastic System Time Domain Simulations

Figure 70 shows the unit step response of AEM1, with and without the effect of power limit. According to Figure 70, the nonlinear, power limited response still satisfies the settling time and steady state error requirements. Little oscillation is observed on the transmission output angular position response, when power limited AEM1 is simulated for a unit step input. Since the linear system behaves faster, there is inevitably an overshoot and more oscillation in the linear response. The transmission output angular position turned out to be satisfactory in terms of the time domain requirements. This is actually not the case for other locations on the control fin.
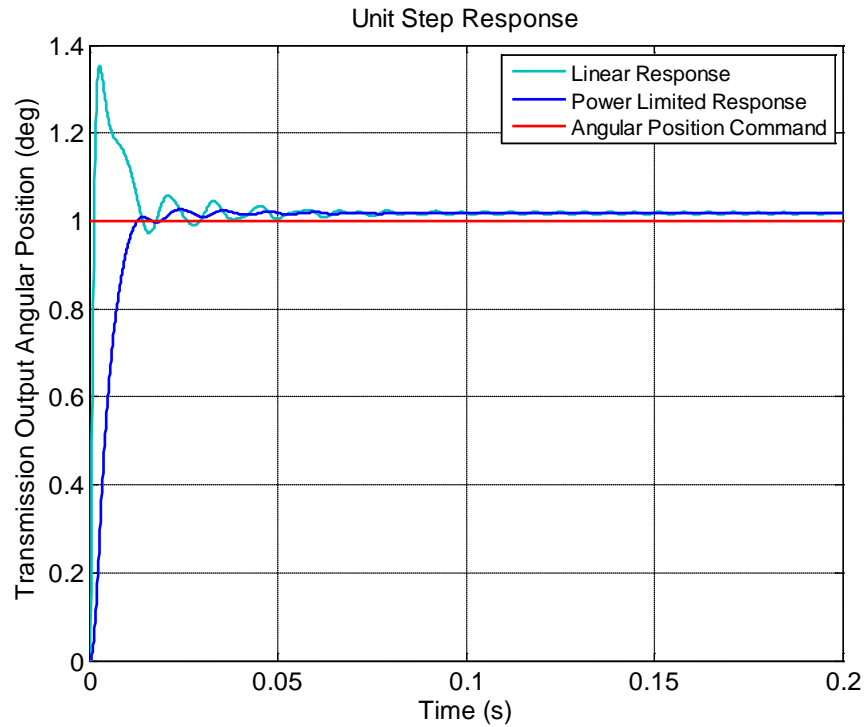


*Figure 70 Time History of Transmission Output of AEM1 for Unit Step Input (Linear and Power Limited Nonlinear Models)*
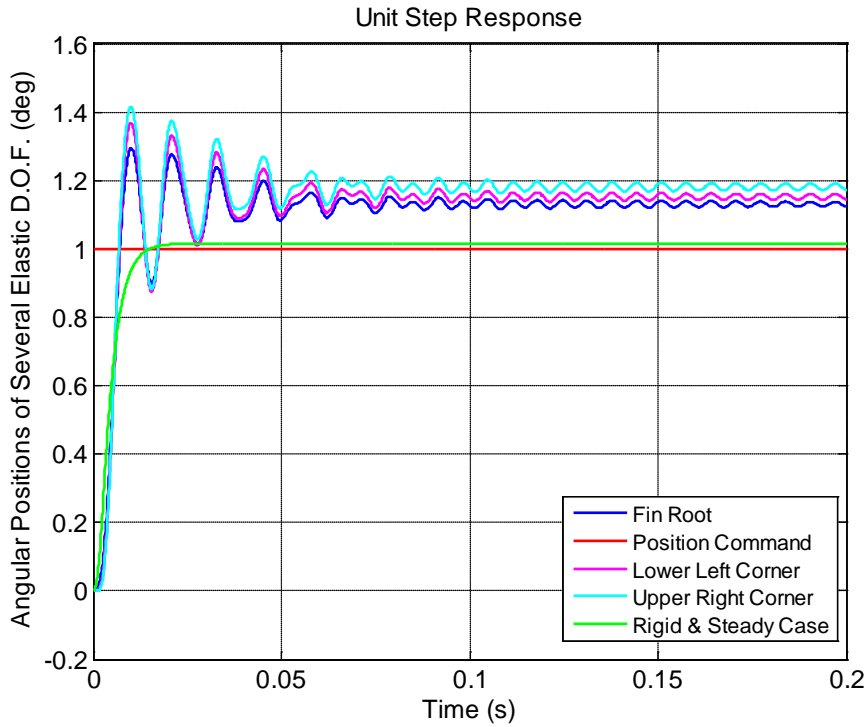
*Figure 71 Time History of Various Elastic D.O.F of AEM1 and Rigid Fin for Unit Step Input (Power Limited Nonlinear Model)*

In Figure 71, the angular positions at various elastic degrees of freedom are given. The lower left corner and the upper right corner are outer corners of the 1st and the 42nd QUAD4 elements given in Figure 12. The positions of the corners of the fin are shown in Figure 72.
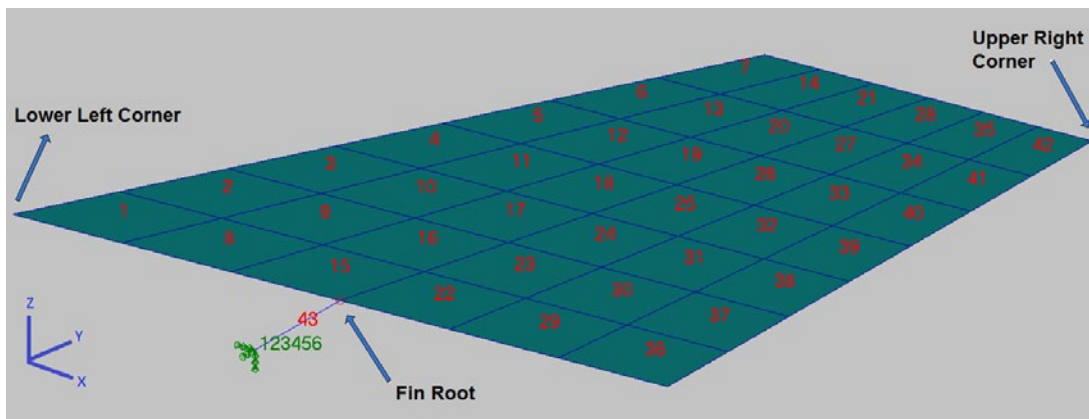


*Figure 72 Fin Positions Demonstrates in Figure 71*

There is an overshoot of 20% to 40% for different locations on the fin. The response converges to steady oscillation with certain static elastic deflection amplitude of about 15% of the input. Therefore, it is actually not possible to say that the steady state error requirement is fulfilled when the static elastic deflection is taken into account. The green line is the time history of the servo-actuation system model built in Chapter 4, involving a rigid fin and only steady aerodynamic moment. The deviation of the elastic response from the rigid fin assumption for the fin under study is significant, therefore the steady state error performance and the damped behavior of the rigid fin could not be preserved.

The position of the missile control fin with respect to the free stream, i.e. the incidence of the missile control fin, is actually not at the desired position. Therefore in both static and dynamic manners this is an unexpected and unwanted situation for the missile overall control system. The autopilot of the missile would try to compensate for the static effect, if it created a measurable response in desired missile orientation or acceleration. In addition, the autopilot of the missile would try to compensate for the oscillation, for instance, if the oscillation interacted with the roll dynamics of the airframe. Whether the interference of the autopilot would make the situation better or worse, would depend on the bandwidth of the autopilot, control effectiveness of the missile.

Figure 73 shows the Fourier transform of the angular position time history of the fin root, after it reaches 95% percent of the input. The mean value of the time history is also discarded. It is observed that the oscillations take place at frequencies very close to natural frequencies of the aeroelastic modes, which are 85.4 Hz and 151.6 Hz for Mach 0.5 and sea level. The difference is considered to be due to the finite sampling rate of the time simulation and the interference with servo-actuator dynamics. The effect of the first aeroelastic mode on the oscillatory response is larger than the second one, because it interferes with the servo-actuation system dynamics.
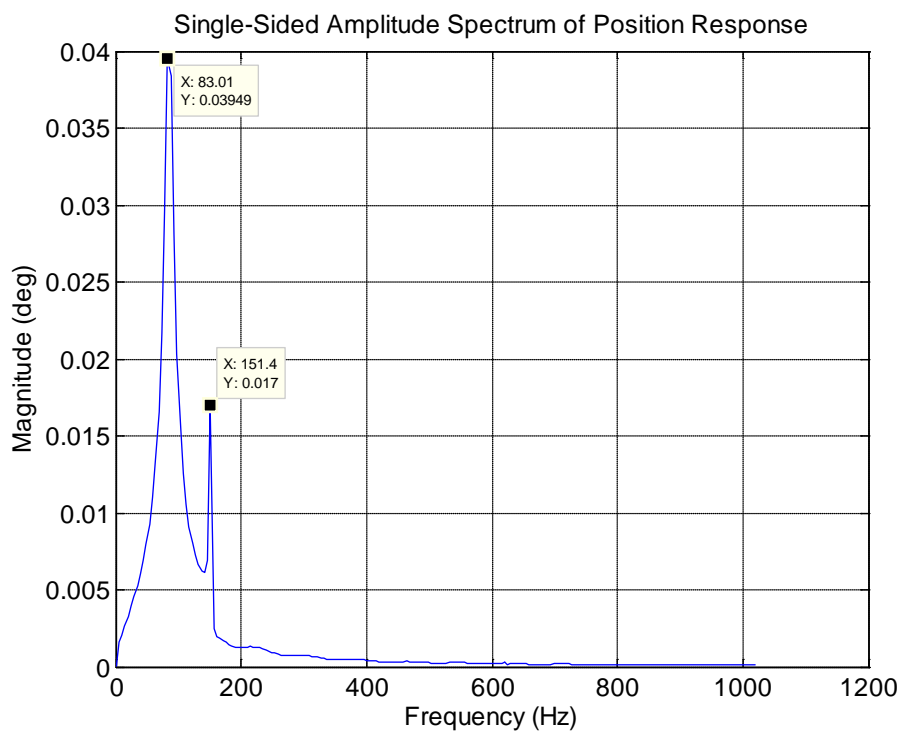


*Figure 73 Frequency Spectrum of the Fin Root Time History of AEM1 for Unit Step Input (Power Limited Nonlinear Model)*

The contribution of all five aeroelastic modes can be observed by inspecting the aeroelastic generalized coordinates' time history in Figure 74. The interference of servo-actuator dynamics and the first aeroelastic mode is clearer in Figure 74. Since the first 50 ms of motion is dominated by the transient behavior of the servo-actuation system, the first mode at 85.4 Hz is excited. Therefore its contribution to the oscillatory response is more dominant in the transient region. After reaching a steady state value, the oscillatory contribution of the first aeroelastic mode dies out, and the oscillatory response becomes dominated by the second aeroelastic mode. The oscillations of the second mode dies out rather slower, since this mode is the one at which the flutter is obtained at Mach 0.74. The steady state values of aeroelastic generalized coordinates converging to nonzero values imply the existence of the static elastic deflection.
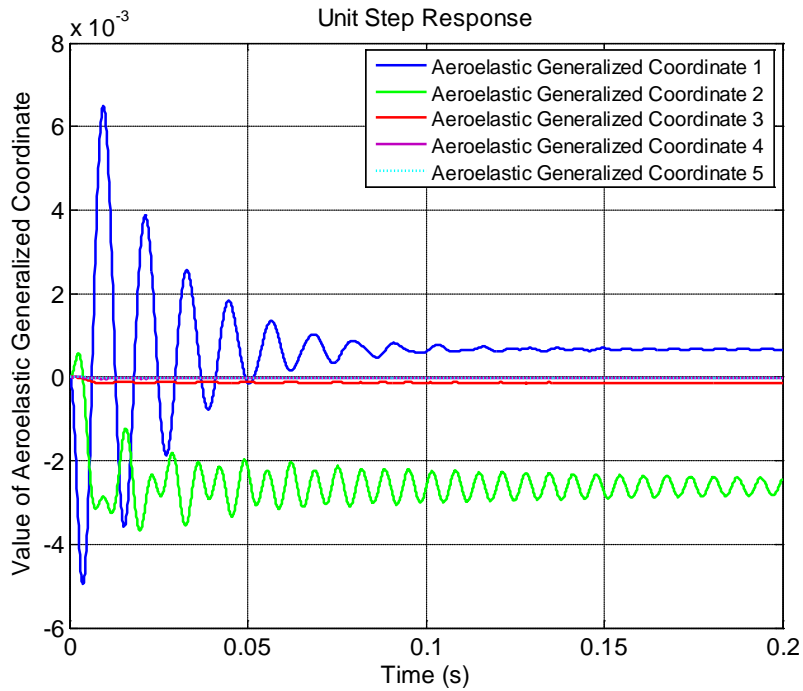
*Figure 74 Time History of Aeroelastic Generalized Coordinates of AEM1 for Unit Step Input (Power Limited Nonlinear Model)*

The aeroelastic hinge moment history is given in Figure 75, together with the steady aerodynamic moment estimate for the same angular position response. Note that the steady state value of the two hinge moments is different due to elastic static deflection of the fin. The oscillatory nature of the load implies more wear, and more power consumption to compensate for the fluctuations.
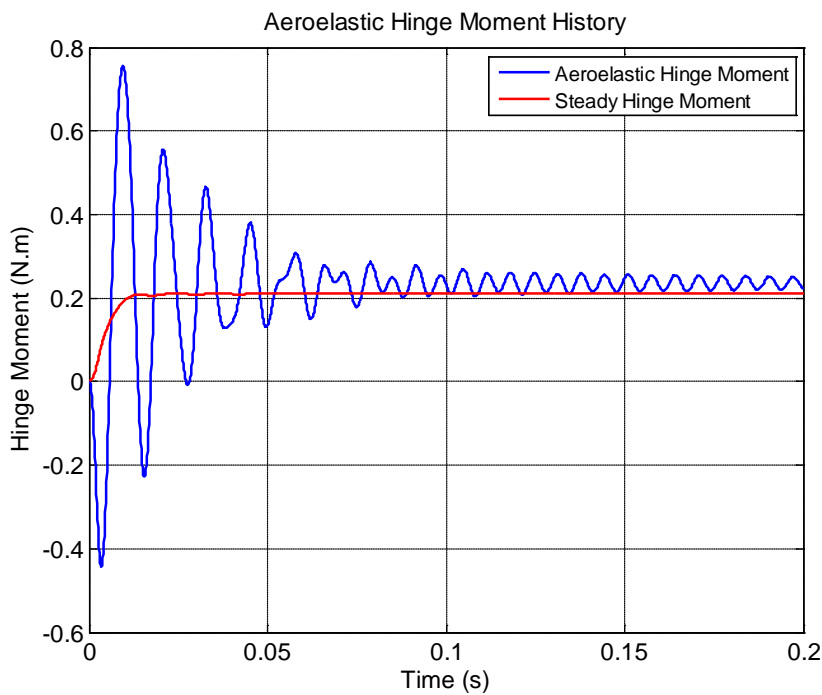


*Figure 75 Time History of Hinge Moment of AEM1 for Unit Step Input (Power Limited Nonlinear Model)*

The response to a +15° step input is simulated and shown in Figure 76, so that the effect of the power limit is fully observed. The nonlinear position response with power limit has very little oscillation because the system slowed down at higher values of the input due to increased effect of power saturation. The nonlinearity imposed a desirable effect, reducing overshoot and oscillation, by limiting the bandwidth of the control system.
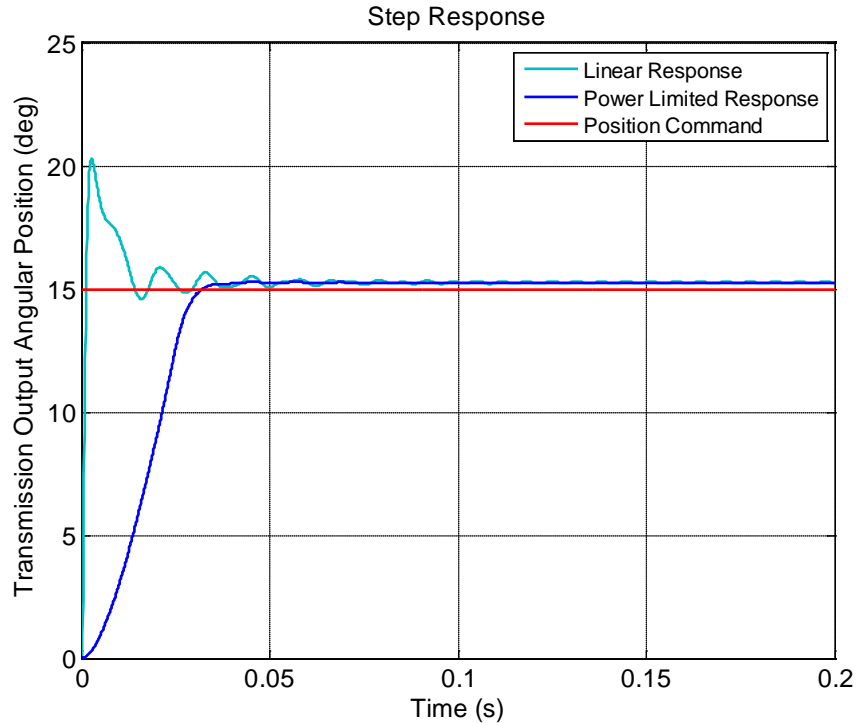


*Figure 76 Time History of Transmission Output of AEM1 for +15° Step Input*

The voltage and current time histories are given in Figure 77 and Figure 78 respectively for the unit step input and the +15° step input. It is observed that the voltage input of the actuator of AEM1 is saturated for a longer time, when the input is +15°. This input dependency and the limiting nature of the system is inherently nonlinear, but seems to be desirable. This is due to the fact that a very fast control system is designed in Section 4.3, counting on the fact that the power limit would reduce overshoots and oscillations at high input values.
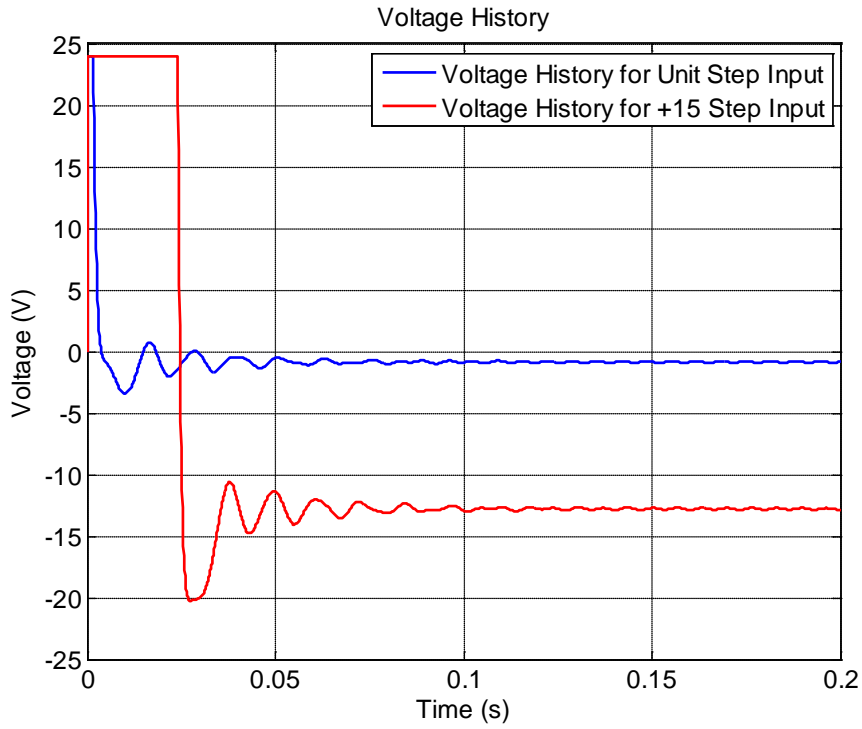
*Figure 77 Time History of Voltage Input of AEM1(Power Limited Nonlinear Model)*
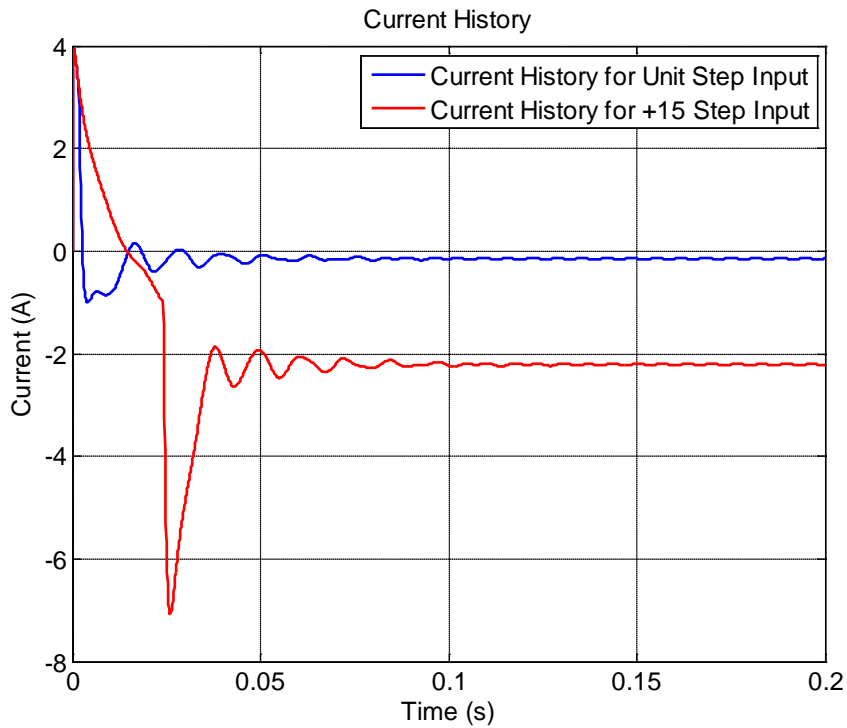


*Figure 78 Time History of Voltage Input of AEM1(Power Limited Nonlinear Model)*

Figure 79 shows the unit step response of AEM2, without the effect of power limit. According to Figure 79, the linear response is unstable, as shown in Figure 68. In this case, because the system is linear, the position response grows unboundedly and AEM2 linear model is dynamically unstable.
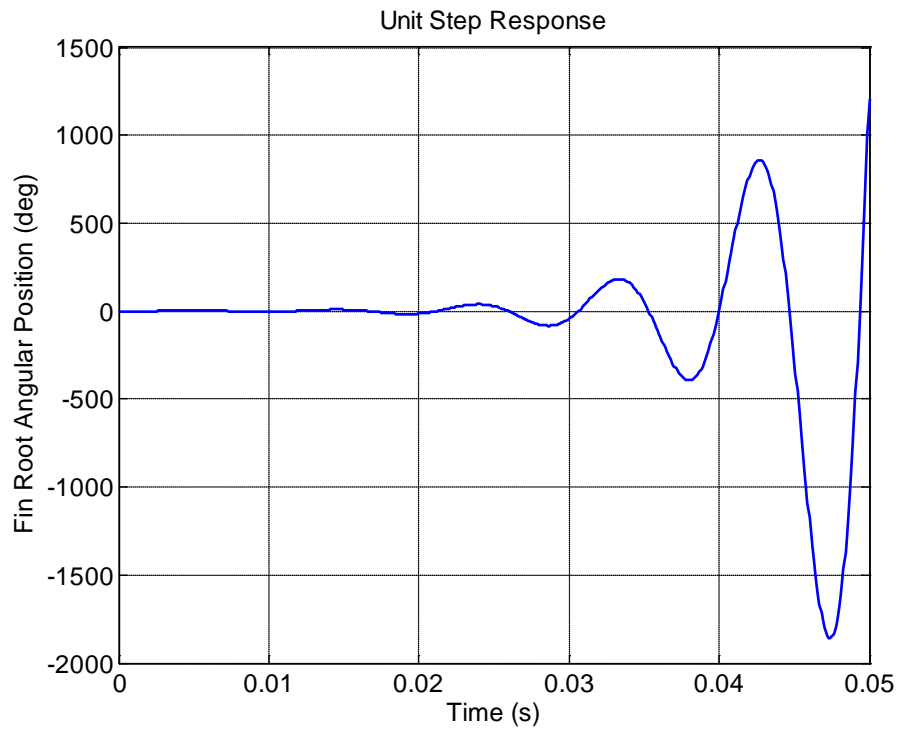
*Figure 79 Time History of Fin Root of AEM2 for Unit Step Input (Linear Model)*

The nonlinear response with power limit is shown in Figure 80. The response in the nonlinear case inherits the behavior of many nonlinear unstable systems, namely the limit cycle oscillation. This limit cycle oscillation actually seems to be of desirable type, since it prevents the system from going unstable, but the oscillation amplitude is clearly unacceptable.

A nonlinearity may also introduce instability to a system, whereas the linearized version of the system is originally stable. This type of instability may have been observed in AEM1, but the limit on voltage is so high that it did not introduce such effect.
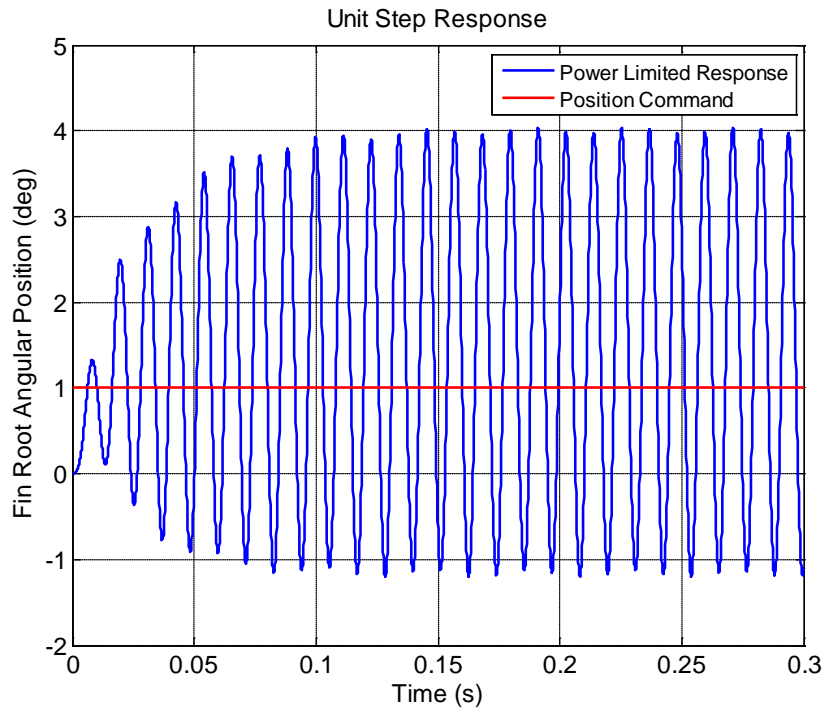
*Figure 80 Time History of Fin Root of AEM2 for Unit Step Input (Power Limited Nonlinear Model)*

Figure 81 shows the Fourier transform of the angular position time history of the fin root, after it reaches 95% percent of the input. The mean value of the time history is also discarded. It is observed that the limit cycle oscillation takes place at approximately a single frequency very close to the first aeroelastic mode's natural frequency.
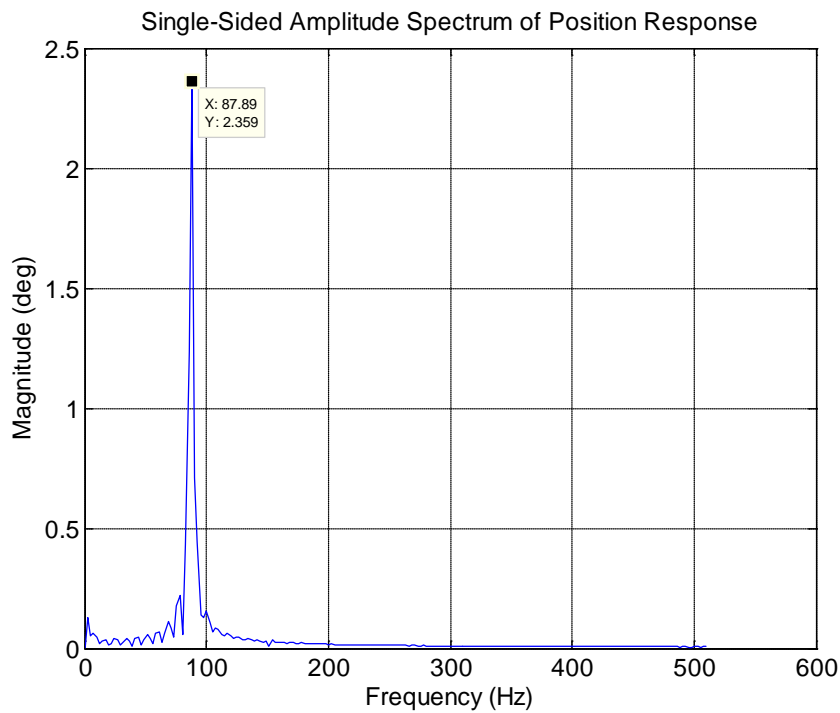


*Figure 81 Frequency Spectrum of the Fin Root Time History of AEM 2 for Unit Step Input (Power Limited Nonlinear Model)*

94

The contribution of all five aeroelastic modes can be observed by inspecting the aeroelastic generalized coordinates' history in Figure 82. The oscillations of the first two aeroelastic modes are sustained, do not grow or decay. The steady state values of aeroelastic generalized coordinates converging to nonzero values imply the existence of the static elastic deflection.

In AEM1, second aeroelastic mode was dominant for the steady state response. The first aeroelastic mode seems to be more pronounced than the second aeroelastic mode in AEM2. This is due to the stronger coupling of the servo-actuator dynamics and aeroelastic dynamics in AEM2. Since the first aeroelastic mode's frequency is closer to the servo-actuation system bandwidth than the second aeroelastic mode, it dominates the oscillatory response both for the transient and for the steady state response.
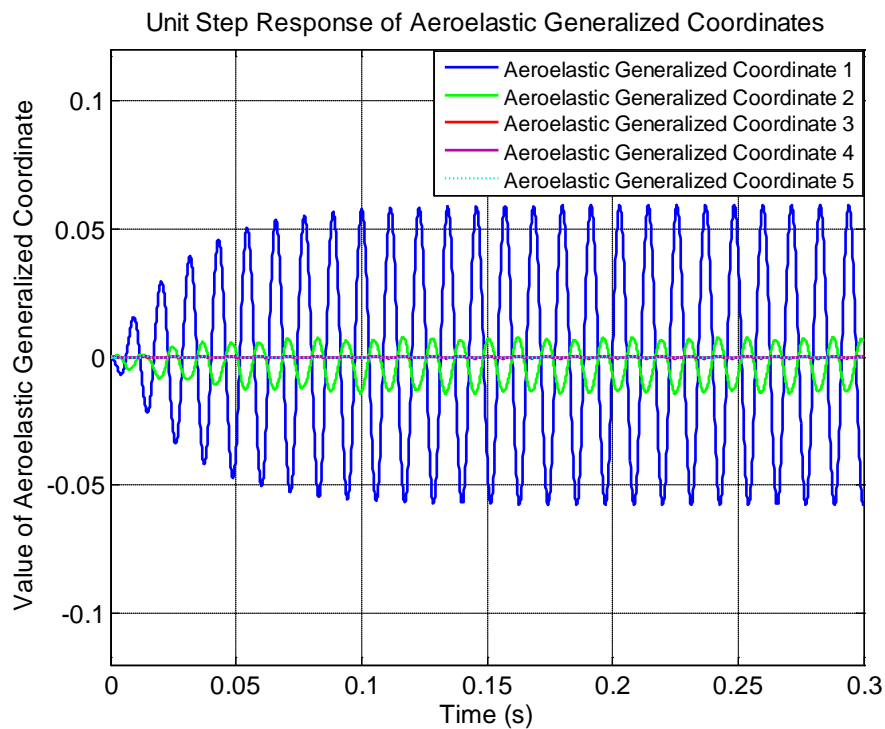


*Figure 82 Time History of Aeroelastic Generalized Coordinates of AEM2 for Unit Step Input (Power Limited Nonlinear Model)*

The voltage and time histories are given in Figure 77 and Figure 78 respectively for the unit step input. Note the repetitively limiting behavior of the voltage input, preventing the diverging nature of the linear model.
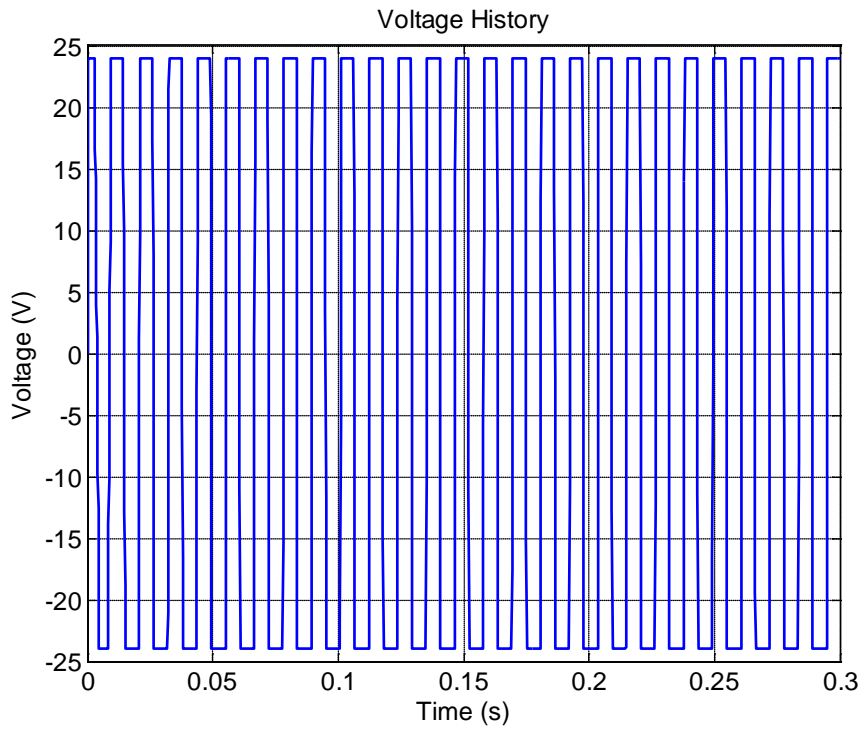
*Figure 83 Voltage History of AEM2 for Unit Step Input (Power Limited Nonlinear Model)*
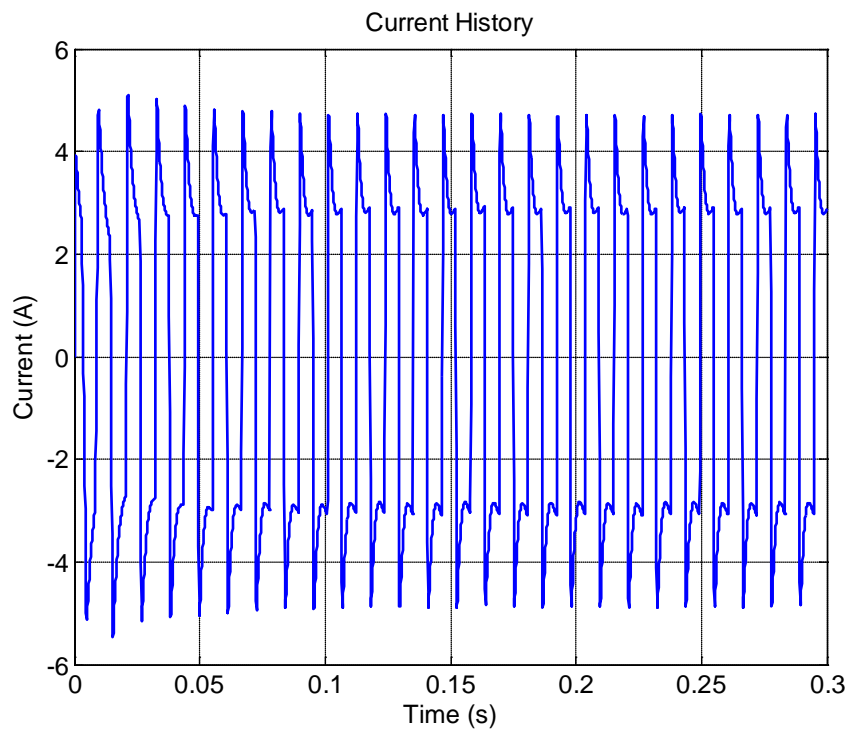


*Figure 84 Current History of AEM2 for Unit Step Input (Power Limited Nonlinear Model)*

# CHAPTER 6

# CONCLUSION

## 6.1    General Conclusions

The aim of this thesis is to build a generic aeroservoelastic model, that renders possible the important physical phenomena involved in the process to be exploited.

To provide genericity in structural modeling, the finite element formulation of structural dynamics is utilized. Through the use of the finite element formulation, implementation of various boundary conditions and various geometries are made possible. One way of using the practical fictitious mass concept[22] is also presented.

Aerodynamic modeling is handled with intermediate complexity, by utilizing panel discretization formulation of the Doublet Lattice Method. Panel formulations are still industry standard because of their ease of use, increased fidelity when compared to two dimensional methods and ability to generate fast estimates of linear aerodynamics when compared to CFD methods. Other than the linear unsteady aerodynamic modeling options in MSC Nastran, there are other panel discretization based aerodynamic solvers in software like ZAERO, which gives high fidelity representations of unsteady aerodynamic phenomena even when certain linearity assumptions of the flow is violated[33]. The aerodynamic forces are modeled with Generalized Aerodynamic Force matrices, to introduce additional modularity, since the extraction of these matrices is also possible with higher fidelity CFD solvers. The Generalized Aerodynamic Force matrices are fitted for a range of reduced frequencies with Roger's RFA method, so that the oscillatory aerodynamic forces can be represented in the time domain.

The aerodynamic and structural matrices are integrated, also accounting for rigid body motion, through a procedure which is well documented by Karpel[25]. The formulation allowed the state space representation of the dynamics of aeroservoselasticity.

To utilize vast opportunities of technical computing and control design, the MATLAB and MATLAB Simulink platforms are used to formulate the aeroservoelastic problem. Servo-actuation system modeling is carried out by implementing linear and nonlinear phenomena in these platforms. To obtain the aeroservoelastic model, the structural and the aerodynamic matrices generated by the 'SEFLUTTER' solver module[34] of MSC NASTRAN are input to the state space models built in MATLAB.

Flutter analysis and normal modes analysis of the resulting models in both platforms are carried out for verification. It is observed that the results of analysis carried out in MSC NASTRAN and MATLAB are very close, even if different methods such as the p-k method, root locus method and time domain simulation is utilized for flutter analysis. A controller design scenario with its constraints and requirements is followed, so that an aeroservoelastic model for frequency and time domain analysis could be built. The behavior of the resulting aeroservoelastic model is analyzed in frequency and time domains. It is observed that the model reflects the key physical phenomena that would render possible the study of different controllers on the missile control fin. The resulting aeroservoelatic model is considered to be a generic and fast tool for controller design purposes.

It is observed that designing the controller by assuming steady aerodynamic forces and a rigid fin turned out to be unsatisfactory for the fin under study, when the aeroservoelastic phenomena came into the picture. Two different aeroservoelastic model topologies are investigated for stability performance, both by linearity assumption and by implementing power source limits. The power

limited nonlinear models, were slower in response, but in a desirable manner to reduce overshoots and oscillations. The first model topology having the transmission output position as the feedback signal, named AEM1, turned out to be a stable aeroservoelastic system. The fin's static deflection and oscillatory behavior in AEM1 showed that the fin could not satisfy its 2% steady state error and damped response design requirements. The relation of this undesired response to the governing missile control system and dynamics is emphasized. The second model topology having the fin root position as the feedback signal, named AEM2, responded to input angular position commands with limit cycle oscillations due to the voltage input limit. The oscillation amplitude turned out to be unacceptable.

## 6.2    Recommendations for Future Work

Since aeroservoelasticity is a multidisciplinary subject, the range of future work that can be carried out is also divided into multiple disciplines. It possible to do future work for all three disciplines involved, and also for combinations of them. The studies that the author is aware of are listed below:

- Although the aeroservoelastic model is built by taking a missile control fin as the plant, the formulation can be easily applied for the wing-aileron combinations of aircraft structures [49].
- The model can be modified to include structural nonlinearities such as freeplay, so that limit cycle oscillations due to these concentrated nonlinearities are simulated[50][52].
- The bending stiffness of the actuator-fin connection is assumed to be infinite. That stiffness could have been modeled to inherit more fidelity.
- Multidisciplinary optimization studies can be carried out on the fin to improve its response characteristics by intentionally changing its stiffness and inertia properties through an iterative optimization method [17].
- The aerodynamic matrices can also be generated by other methods such as CFD, or higher fidelity panel methods such as in ZAERO [33].
- RFA methods other than Roger's Least Square fit can be employed to obtain better fits or smaller number of states.[16][23].
- Active vibration control studies can be carried out by utilizing robust controller design methods such as $H_\infty$ controller design [51].
- Active vibration control studies by utilizing piezoelectric patches can be studied [39].
- To increase the fidelity of the model further, the dynamics and digital nature of the sensors can be modeled. The effects due to digital nature of the controllers can also be modeled.
- The results of the aeroservoelastic model built in MATLAB can be compared with the results that can be obtained from transient response analysis solvers of MSC NASTRAN and other software.

# REFERENCES

[1]   Bisplinghoff, Raymond L., Ashley, H., Halfman, Robert L., Aeroelasticity. Addison-Wesley Publications, Massachusetts, 1957.

[2]   Theodorsen, T., General Theory of Aerodynamic Instability and the Mechanism of Flutter," NACA TR No. 496, May 1934.

[3]   Wagner, H., Uber die Entstehung des dynamischen Auftriebes von Tragugeln," February 1925, pp. 17-35.

[4]   Kussner, H. G., Zusammenfassender Berichtuber den instationaren Auftrieb vonFlugeln," December 1936, pp. 410-424

[5]   Garrick, I. E., On Some Reciprical Relations in the Theory of Nonstationary Flows," NACA TR No. 629, March 1938.

[6]   von Karman and Sears, Airfoil Theory for Non-Uniform Motion," Journal of the Aeronautical Sciences, Vol. 5, No. 10, 1938, pp. 379-390.

[7]   Collar, A. R., "The Expanding Domain of Aeroelasticity," Royal Aeronautical Society Journal, Vol. 50, Aug. 1946, pp. 613–636.

[8]   Bisplinghoff,R. L., and Ashley, H., Principles of Aeroelasticity, 1st ed., Wiley, New York, 1962, pp. 18–69, 450–486.

[9]   Garrick, I. E., "A Survey of Aerothermoelasticity,"AerospaceEngineering, Vol. 22, No. 1, 1963, pp. 140–147.

[10]  Garrick, I. E., "Aeroelasticity-Frontiers and Beyond," Journal of Aircraft, Vol. 13, No. 9, 1976, pp. 641–657.

[11]  Albano, E., and Rodden, W. P., "A Doublet Lattice Method for Calculating Lift Distributions on Oscillating Surfaces in Subsonic Flow," AIAA Journal, Vol. 7, No. 2, 1969, pp. 279–285.

[12]  Rodden, W.P., Taylor, P.F. and McIntosh, S.C., Further Refinement of the Subsonic Doublet-Lattice Method, AIAA J. Vol. 35, No. 5, 1998

[13]  Vepa, R., "Finite State Modeling of Aeroelastic Systems," NASA CR-2779, 1977; also, AIAA Paper 76-17, 1976.

[14]  Edwards, J. W., Ashley, H., and Breakwell, J. V., "Unsteady Aeroelastic Modeling for Arbitrary Motion," AIAA Journal, Vol. 17, No. 4, 1979, pp. 365–374.

[15]  Roger, K. L., "Airplane Math Modeling and Active Aeroelastic Control Design," CP-228,AGARD, Brussels, Aug. 1977, pp. 1–11.

[16]  Tiffany, S. H., and AdamsW.M., "Nonlinear Programming Extensions to Rational Function Approximation Methods for Unsteady Aerodynamic Forces," NASA TP 2776, July 1988.

[17]  Karpel, M., "Reduced-Order Models for Integrated Aeroservoelastic Optimization," Journal of Aircraft, Vol. 36, No. 1, 1999, pp. 146–155.

[18]  Nissim, E., and Abel, I., "Development and Application of an Optimization Procedure for Flutter Suppression Using the Aerodynamic Energy Concept," NASA TP 1173, Feb. 1978.

[19]  Newsom, J. R., Abel, I., and Dunn, H.J., "Application of Two Design Methods for Active Flutter Suppression and Wind-Tunnel Test Results," NASA TP 1653, May 1980.

[20]  Karpel, M., and Sheena, Z., "Structural Optimization for Aeroelastic Control Effectiveness," Journal of Aircraft, Vol. 26, No. 5, 1989, pp. 493-495.

[21]  Karpel, M., "Multidisciplinary Optimization of Aeroservoelastic Systems Using Reduced-Size Models," Journal of Aircraft, Vol. 29, No. 5, 1992, pp. 939-946.

[22]  Karpel, M., and Raveh, D., "Fictitious Mass Element in Structural Dynamics," AIAA Journal, Vol. 34, No. 3, 1996, pp. 607-613.

[23]  Karpel, M., and Hoadley, S. T., "Physically Weighted Approximations of Unsteady Aerodynamic Forces Using the Minimum-State Method," NASATP-3025, March 1991.

[24]  Karpel, M., "Design for Active Flutter Suppression and Gust Alleviation Using State-Space Aeroelastic Modeling," Journal of Aircraft, Vol. 19, No. 3, 1982, pp. 221-227.

[25]  Karpel, M., "Time-Domain Aeroservoelastic Modeling Using Weighted Unsteady Aerodynamic Forces," Journal of Guidance, Control, and Dynamics, Vol. 13, No. 1, 1990, pp. 30-37.

[26]  Karpel, M., and Presente, E., "Structural Dynamic Loads in Response to Impulsive Excitation," Journal of Aircraft, Vol. 32, No. 4,1995, pp. 853-861.

[27]  L. Meirovitch, Fundamentals of Vibrations, McGraw-Hill, New York, 2001.

[28] David N. Herting , MSC - Nastran Advanced Dynamic Analysis User's Guide, MacNeal-Schwendler Corporation, 1997.

[29] John D. Anderson, Fundamentals of Aerodynamics, McGraw-Hill, 3rd edition, January 2001.

[30] Gülçat, Ü., Fundamentals of Modern Unsteady Aerodynamics, Springer, 2010.

[31] Fung, Y.C., "An Introduction to the Theory of Aeroelasticity," Dover Publications, Inc., 1969.

[32] M. F. E. Dillenius and T. O. Lesieutre, Missile Fin Planform Optimization for Improved Performance, AGARD 82nd Fluid Dynamics Panel Symposium on Missile Aerodynamics, Sorrento, Italy, May 1998.

[33] Zona Technology, Inc. ZAERO 7.1 Theoretical Manual.

[34] Rodden, W.P., and Johnson, E. H., (1994). MSC/NASTRAN Aeroelastic Analysis User's Guide. The MacNeal-Schwendler Corporation.

[35] MSC.FlightLoads and Dynamics User's Guide Version 2006, MSC.Software Corporation.

[36] Luis R. Miranda, Robert D. Elliott, and William M. Baker, A generalized vortex lattice method for subsonic and supersonic flow applications, NASA CR-2865, December 1977.

[37] Dunn H. J., An Analytical Technique for Approximating UnsteadyAerodynamics in the Time Domain, NASA Technical Paper 1738, November 1980.

[38] Dowell E. H., A Modern Course in Aeroelasticity, Springer, 2005.

[39] F. M. Karadal. Active Flutter Suppression of a Smart Fin. Master's thesis, Middle East Technical University, 2008.

[40] Evans, W. R., "Graphical Analysis of Control Systems," Transactions of the AIEE, Vol. 67, 1948, pp. 547–551.

[41] MSC.Nastran Quick Reference Guide, MSC.Software Corparation, 2003.

[42] Reymond, Michael: MD NASTRAN 2006 DMAP Programmer's Guide, The MacNeal-Schwendler Corporation, 2006.

[43] MATLAB, "User's Manual", Version 6.5, The MathWorks Inc., 2003.MSC.

[44] Nastran Aeroelastic Analysis NAS111 Lecture Notes, MSC.Software Corparation, 1999.

[45] Hodges, D.H. and Pierce, G.A., "Introduction to Structural Dynamics and Aeroelasticity," Cambridge University Press, 2002.

[46] Vos, V., A Comprehensible Guide to Servo Motor Sizing, Copperhill Technologies Corporation, 2007.

[47] Siouris George. M., Missile Guidance And Control Systems, Springer, New York, 2004.

[48] K. Ogata, Modern Control Engineering, 4th edition, Pearson Education, New Delhi, 2003.

[49] Gold, P. and Karpel, M., "Reduced-Size Aeroservoelastic Modeling and Limit-Cycle-Oscillation Simulations with Structurally non-Linear Actuators," Journal of Aircraft, Vol.45, No. 2, 2008, pp. 471-477.

[50] Lee, I., and Kim, S. H., "Aeroelastic Analysis of a Flexible Control Surface with Structural Nonlinearity," Journal of Aircraft, Vol. 32, No. 4, 1995, pp. 868–874.

[51] Akmeşe A., Cömert M. D., Platin B.E., Aeroservoelastic Analysis of Missile Control Surfaces via Robust Control Methods. IFAC 2004.

[52] Yehelzkely, E., and Karpel, M., "Nonlinear Flutter Analysis of Missiles with Pneumatic Fin Actuators," Journal of Guidance, Control, and Dynamics, Vol. 19, No. 3, 1996, pp. 664–670.